Synthesis and Structural Characterization of Semiconductors based on Kesterites

vorgelegt von

Anna Ritscher, Bakk.rer.nat M.Sc.

aus Villach, Österreich

von der Fakultät II - Mathematik und Naturwissenschaften
der Technischen Universität Berlin
zur Erlangung des akademischen Grades

Doktorin der Naturwissenschaften

- Dr.rer.nat. -

genehmigte Dissertation

Promotionsausschuss:

Vorsitzende: Prof. Dr. Regine von Klitzing

Gutachter: Prof. Dr. Martin Lerch

Gutachter: Prof. Dr. Manfred Mühlberg

Tag der wissenschaftlichen Aussprache: 28.10.2016

Berlin, 2016

"There is a theory which states that if ever anyone discovers exactly what the Universe is for and why it is here, it will instantly disappear and be replaced by something even more bizarre and inexplicable. There is another theory mentioned, which states that this has already happened."

— Douglas Adams, The Hitchhiker's Guide to the Galaxy

Abstract

The here-presented thesis provides detailed investigations on the structural characteristics of the chalcogenide Cu_2ZnSnS_4 (CZTS). This semiconductor material is a promising candidate for absorber layers in solar cells due to its desirable properties for thin film photovoltaic applications. Yet, compared to current used chalcopyrite-based devices, efficiencies are significantly lower. This could be attributed to structural effects. Fundamental understanding of the structural characteristics of potential thin film absorber compounds is crucial for proper materials design in the field of solar technology. Therefore, intensive research is necessary to obtain knowledge on so far unexplored structural features or to certify and extend current literature data.

The main objective of the here-presented work was to deepen the understanding of the quaternary sulfide Cu_2ZnSnS_4. Primary, this implied the full characterization of structural properties of the compound using various diffraction techniques.

As the synthesis of phase-pure kesterite powder is a challenging problem, one of the central points of this work was the development of a novel rapid and facile synthesis process leading to single phase material. A mechanochemical approach was successfully introduced, including the reaction of the corresponding binary sulfides in a planetary ball mill followed by an annealing procedure in H_2S atmosphere, leading to highly crystalline powder samples. The crystallization of the as-milled powder during annealing was tracked by high temperature X-ray diffraction measurements. With this synthesis method it is nicely possible to control the composition of the synthesized powder. Therefore, it was feasible to prepare single phase stoichiometric as well as off-stoichiometric samples with desired compositions. Phase purity and composition were determined by means of electron microprobe analysis and X-ray absorption spectroscopy.

First, structural analysis of a stoichiometric sample was performed using X-ray powder diffraction methods including Rietveld refinement. As copper and zinc are not distinguishable using conventional X-ray diffraction methods, only the Sn/(Cu/Zn) distribution could be disclosed, whereas Cu/Zn order remained unknown. For full cation distribution analysis, neutron diffraction measurements were performed, as copper and zinc show a significant difference in the neutron scattering length. It could be shown that the powder sample adopts the kesterite-type structure with a partial disorder of copper and zinc on the two Wyckoff positions $2c$ and $2d$.

Another key issue of the present thesis was the investigation of the order-disorder transition in Cu_2ZnSnS_4. For this purpose, a series of stoichiometric CZTS samples were synthesized according to the mechanochemical synthesis process and afterwards annealed at different temperatures in a range of $473-623\,K$. Again, neutron diffraction techniques were used to investigate the samples. Detailed structural analysis revealed a Landau-type second order transition from an ordered to a disordered kesterite-type structure at a critical temperature of $552\pm2\,K$. Additionally, a fully ordered Cu_2ZnSnS_4 powder sample (within the standard deviation) was successfully synthesized at $473\,K$.

In a final step, special focus was put on the study of intrinsic point defects in off-stoichiometric kesterite. For this purpose, B- and C-type off-stoichiometric samples were prepared and analyzed by means of X-ray and neutron diffraction measurements. It could be shown that it is possible to synthesize phase-pure kesterite samples with a composition far off the stoichiometric point.

Kurzfassung

Die vorliegende Arbeit liefert eine detaillierte Untersuchung der strukturellen Eigenschaften des Chalkogenides Cu_2ZnSnS_4 (CZTS). Die Halbleiterverbindung gilt als ein vielversprechender Kandidat für Absorberschichten in Solarzellen aufgrund ihrer geeigneten Eigenschaften für Dünnschicht-Photovoltaik-Anwendungen. Im Vergleich zu aktuellen verwendeten Chalkopyrit-basierten Solarzellen sind die Effizienzen jedoch deutlich geringer. Dies könnte auf strukturelle Effekte zurückzuführen sein.

Ein fundamentales Verständnis der strukturellen Merkmale von potentiellen Dünnschicht-Absorber-Verbindungen ist für die Materialentwicklung auf dem Gebiet der Solartechnik von entscheidender Bedeutung. Die detaillierte Erforschung der Kristallstruktur ist notwendig um deren Beeinflussung der physikalischen und chemischen Eigenschaften des Materials festzustellen.

Das Hauptziel der hier präsentierten Arbeit war es, das Verständnis des quaternären Sulfids Cu_2ZnSnS_4 zu vertiefen. Primär impliziert dies die vollständige Charakterisierung der strukturellen Eigenschaften der Verbindung mit Hilfe verschiedener Beugungstechniken.

Da die Synthese von phasenreinem Kesteritpulver eine anspruchsvolle Aufgabe ist, war die Entwicklung eines neuartigen, schnellen und einfachen Syntheseverfahrens zu Herstellung einphasigen CZTS-Materials ein zentraler Punkt dieser Arbeit. Ein mechanochemischer Prozess wurde erfolgreich entwickelt. Dieser umfasst die Umsetzung der entsprechenden binären Sulfide in einer Planetenkugelmühle und ein anschließendes Temperverfahren in H_2S Atmosphäre, wodurch ein hochkristallines Pulver erhalten wird. Mittels Hochtemperatur-Röntgenbeugungsmessungen konnte die Kristallisation des gemahlenen Pulvers *in situ* verfolgt werden. Mit dem neu entwickelten Verfahren ist es möglich, die Zusammensetzung des synthetisierten Pulvers zu steuern. Daher war die Herstellung einphasiger stöchiometrischer sowie nicht-stöchiometrischer Proben mit gewünschten Zusammensetzungen realisierbar. Die Phasenreinheit und die exakte Zusammensetzung wurden mittels Elektronenstrahlmikroanalyse und Röntgenabsorptionsspektroskopie bestimmt.

Erste strukturelle Untersuchungen einer stöchiometrischen Probe wurden mittels Pulver-Röntgenbeugung und anschließender Rietveld-Verfeinerung durchgeführt. Kupfer und Zink sind mit herkömmlichen Röntgenbeugungsmethoden nicht unterscheidbar, dadurch ließ sich nur die Sn/(Cu/Zn) Verteilung bestimmen, während die Cu/Zn-Ordnung unklar blieb. Zur vollständigen Kationenverteilungsanalyse wurden Neutronenbeugungsmessungen durch-

geführt, da Kupfer und Zink einen signifikanten Unterschied in der Neutronenstreulänge aufweisen. Es konnte gezeigt werden, dass das Pulver im Kesterit Strukturtyp kristallisiert und eine partielle Unordnung von Kupfer und Zink auf den beiden Wyckoff-Positionen $2c$ und $2d$ aufweist.

Ein weiterer Schwerpunkt der vorliegenden Arbeit war die Untersuchung des Ordnungs-Unordnungs-Übergangs in Cu_2ZnSnS_4. Hierfür wurde eine Reihe stöchiometrischer CZTS Proben nach dem mechanochemischen Syntheseverfahren hergestellt und anschließend bei verschiedenen Temperaturen in einem Bereich von $473-623\,K$ getempert. Zur detaillierten Strukturanalyse wurden Neutronenbeugungsmessungen durchgeführt und die Kristallstrukturen wurden mit Hilfe der Rietveld-Methode verfeinert. Diese Untersuchungen ergaben einen Landau–Übergang zweiter Ordnung. Die kritische Temperatur des Übergangs von der geordneten zur ungeordneten Kesterit-Struktur konnte mit $552\pm2\,K$ bestimmt werden. Zusätzlich konnte bei $473\,K$ eine vollständig geordnete Cu_2ZnSnS_4 Probe (innerhalb der Standardabweichung) erfolgreich synthetisiert werden.

Abschließend wurden Untersuchungen zu intrinsischen Punktdefekten nicht-stöchiometrischer Kesterit-Proben durchgeführt. Zu diesem Zweck wurden Pulverproben des nicht-stöchiometrischen B- und C-Typs gemäß der mechanochemischen Route hergestellt und mittels Röntgen- und Neutronenbeugungsmessungen untersucht. Es konnte gezeigt werden, dass es möglich ist, phasenreine Kesterit-Proben mit einer Zusammensetzung weit vom stöchiometrischen Punkt zu synthetisieren.

Acknowledgement

of theoretical and practical questions. In particular I want to bring out the help of Dr. Suliman Nakhal for helping with every problem of the Rietveld refinements, and Dr. Sevilay Cosgun for our great talks about everything and anything during lunch time. And of course Steven Orthmann for our working group ICSD.

My thanks also go to my colleagues of the Helmholtz-Zentrum Berlin graduate school. Elisa and Kai who helped me a lot with any crystallographic issue concerning the kesterite material, Anastasia for our motivating talks and the enjoyable conference visits, and all other MatSEC students for the nice discussions at our research colloquia.

Moreover, thanks go to my lovely friends here in Berlin, in Austria, and in other parts of Europe and the world, who have always been there for me. Many thanks for the moral and emotional support during this work, for enriching my life and for all our exciting and unforgettable memories. A big thank goes to Silvia for the proofreading the thesis.

All of this could not happen without my family, I am very thankful to my parents for their continuous encouragement, love and full support in all matters. Last but not least, I want to express my gratitude and love to Ralf. All these years, he has been my best friend and great companion who encouraged me when I doubted myself and always stayed by my side, even when my mind was miles away. I truly thank him for his support, patience and unwavering love and of course for arousing and sharing my passion for photography, which became more than a hobby and made us exploring the world in our own way.

Danke!

Preface

The here-presented dissertation is written in a cumulative way. The overall research question of the doctoral project is presented by a comprehensive introductory chapter including theoretical background and methodology, describing the used scientific methods (Part I – Introduction). This introduction completes with a corresponding bibliography.

The results (Part II – Results and Discussion) of the work are based on following, already published journal articles.

1. Anna Ritscher, Justus Just, Oleksandr Dolotko, Susan Schorr, Martin Lerch; **A mechanochemical route to single phase Cu_2ZnSnS_4 powder**, *J. Alloys Compd.* 2016, *670*, 289 – 296.

2. Anna Ritscher, Markus Hoelzel, Martin Lerch; **The order-disorder transition in Cu_2ZnSnS_4 – a neutron scattering investigation**, *J. Solid State Chem.* 2016, *238*, 68 – 73.

3. Anna Ritscher, Marc Schlosser, Arno Pfitzner, Martin Lerch; **Study of the mechanochemical process to crystalline Cu_2ZnSnS_4 powder**, *Mater. Res. Bull.* 2016, *84*, 162 – 167.

4. Anna Ritscher, Alexandra Franz, Susan Schorr, Martin Lerch; **Off-stoichiometric CZTS - Neutron scattering investigations on mechanochemical synthesized powders**, *J. Alloys Compd.* 2016, *689*, 271 – 277.

In order to have a consistent layout and good readability the formatting is kept identical for the entire work. Thus, the display format of the papers incorporated in the thesis is not similar to the published versions. Each publication has an independent introductory section, consequently some information might be repeated within the work. Every publication concludes with its related list of references.

The subsequent section (Chapter 8 – Conclusion and Prospects) collects the major results and relevant information discussed in the individual publications and closes with a short outlook to possible prospective experiments in the research area.

Contents

Part I.

Introduction

1. Motivation

1.1. Energy issue

The global energy demand is constantly increasing due to rising living standards and the advancing technologization not only in highly developed countries but also in emerging nations. In recent years an annual growth of about 1.5 % of the global consumption is reported [1], leading to a world primary energy use of about 12.9 billions tons of oil equivalent ($= 12.5 \cdot 10^{14}$ kWh) in 2014 [2]. Providing energy access to the continuously growing earth's population, which already reached the 7.3 billions people mark [3], is one of the biggest challenges of our time. Today's energy supply is still primarily covered by fossil fuels like oil, natural gas, or coal [4]. Due to the sudden decline in oil prices at the end of 2014 the attractiveness of carbon based fuels is once more strengthened [5]. One of the biggest problems concerning these energy sources is the shortage of raw material. Fossil resources are finite, even though innovative extraction processes are prolonging the use of carbon based fuels for a certain timeframe [4]. Moreover, the burning of fossil fuels is irrevocably linked to global warming due to the emission of CO_2 and additional greenhouse-gases. Since the beginning of the 20th century carbon emissions increased dramatically resulting in a high atmospheric CO_2-concentration and concerns about the causes and effects of the related climate change are omnipresent [6].

Therefore, other energy sources, which help managing the increasing energy consumption and reducing CO_2-emission, are required. A low carbon power generating technology, which has long been regarded as a potential alternative to fossil fuels, is nuclear power. However, several factors, such as the limiting availability of uranium or the difficulty in the management and final storage of radioactive waste [7], make nuclear power plants not a long term alternative. Furthermore, the growing public rejection due to the risk of nuclear accidents or the possible abuse of nuclear research by the military industry cannot be disregarded.

Consequently, the use of renewable energy sources and new energy storage systems is getting increasingly important for the development of a worldwide sustainable energy policy. A lot of progress has been made in developing cleaner and more efficient energy in order to overcome the dependence on fossil fuels. In 2014, the amount of world's CO_2-emission remained stable in spite of the growing global economy and increasing energy consumption.
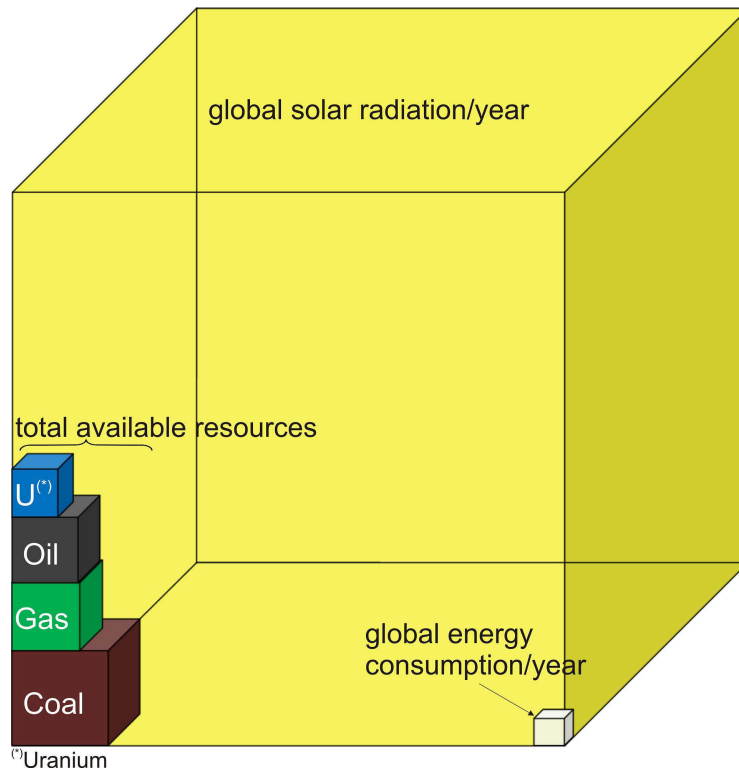
Figure 1.1.: Estimated annual potential of solar energy in comparison with the worldwide energy demand, as well as the total available resources of fossil and nuclear energy sources. Energy dice according to Ref. [8].

This was the first time in 40 years and it can be primarily attributed to the increasing use of renewable energy sources and the improved energy efficiency [1]. As long ago as 2013, 19.1 % of world's final energy consumption was provided by renewable energy sources [1]. Sustainable technologies are getting more and more competitive, but still a lot of research is needed to reduce costs and enhance efficiencies [5]. Apart from the use of hydropower, wind power, biomass energy, geothermal energy, and tidal power, the use of solar energy in form of solar thermal power or photovoltaics (PV) are in the focus of interest.

1.2. Solar power

The direct conversion of solar energy into electrical energy is perhaps the most promising sustainable energy. Each year, the sun provides us with $1.119 \cdot 10^{18}$ kWh of radiant energy [8]. This means that the annual solar radiation on earth exceeds the total global energy consumption by a factor of 7000. This relation is depicted in Figure 1.1. Thus, solar energy alone could cover the world's energy demand, even taking into account that the actual technologically usable potential for solar energy is lower than the theoretical
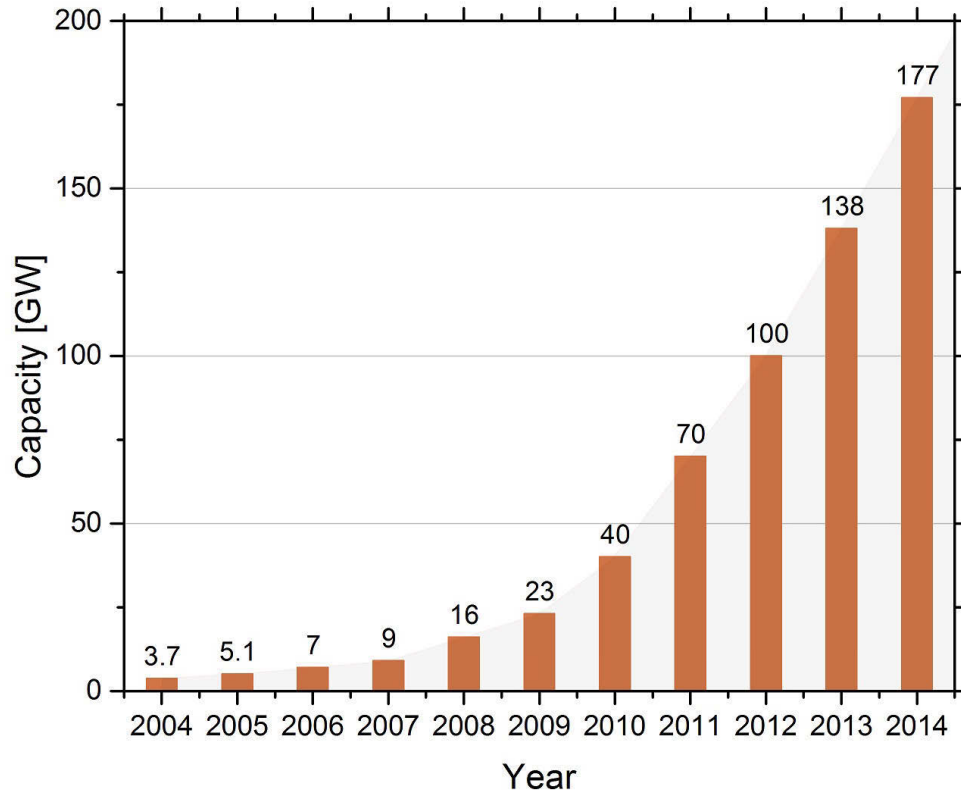
Figure 1.2.: Growth of the worldwide solar photovoltaic capacity (2004 – 2014) according to Ref. [1].

one, due to structural and ecological restrictions as well as limited efficiencies and plant sizes [9].

The solar technology is an important and rapidly growing industrial sector with a high rate of innovation. The worldwide capacity of solar photovoltaics increased from 3.4 GW in 2004 to a total of 17 GW in 2014. 60 % of the global capacity was added in the years 2012 – 2014 (see Figure 1.2). At present, crystalline silicon based devices are the predominant solar technology with an 80 – 90 % share of the world market in recent years. They belong to the so called "first generation solar cells" with record efficiencies up to 25 % for monocrystalline and 21 % for multicrystalline Si-solar cells [8, 10]. However, the high energy consumption and production costs, which are caused by the need of highly purified silicon material, as well as the excessive material necessity (layer thickness of around 180 μm), lead to considerable long energy payback times of these solar power systems [8]. As a result, despite the high efficiency rates of silicon based devices, the almost unlimited availability and the low price of silicon raw material, scientists are looking for suitable and affordable alternatives to the currently dominant solar technology.

One suitable approach is the usage of thin film solar cells, where the absorber material has only a thickness of a few micrometers. Due to the use of materials with high absorption coefficients the required quantity of material can be reduced, leading to considerable energy and production cost savings. For example, utilizing amorphous silicon for so called pin-cells would allow thinner layers to be used for devices. But until now these a-Si cells are no real alternative to crystalline Si-cells as they only reach low efficiencies that are even further degraded in direct sunlight after a longer period of time [8].

Other thin film technologies on the basis of compound semiconductors have proven to be a more promising alternative to silicon based devices. Among this second generation of light absorbers, two material systems, namely cadmium telluride (CdTe) and copper indium gallium selenide (CIGS –$Cu(In,Ga)Se_2$), have successfully entered the solar market so far. CdTe and CIGS solar cells have reached power conversion efficiency records of 22.1 and 22.3 %, respectively [10]. Despite the large improvement of devices using these absorber materials, the low abundance of In and Te, as well as the toxicity of Cd is the major obstacle to their widespread use. The development of new environmental friendly, low cost, and abundant materials as a persistent alternative to CdTe and CIGS alloys plays a decisive role for the advancement of thin film photovoltaic technologies.

1.3. $Cu_2ZnSn(S,Se)_4$ compounds

In the last decades, many efforts have been undertaken in the field of thin film technologies in order to develop a new class of materials as a possible replacement for CdTe and CIGS as absorber material. One auspicious approach is the quaternary chalcogenide $CZT(S,Se)$ (kesterite). $CZT(S,Se)$ is a compound semiconductor made of copper, zinc, tin, and sulfur (selenium). Extensive research in the field of kesterite is addressed to the pure sulfide Cu_2ZnSnS_4 (CZTS), the pure selenide $Cu_2ZnSnSe_4$ (CZTSe), as well as their solid solution $Cu_2ZnSn(S,Se)_4$ (CZTSSe). Kesterite compounds are very promising materials, as they are p-type semiconductors with a direct band gap between 1.0 eV (pure Se material) and 1.5 eV (pure S material) [11], both close to the optimal value for solar energy conversion [8]. In recent years, rapid improvements of the device performance have been obtained using kesterite materials. The current record efficiency of 12.6 % was reached for thin film solar cells based on the solid solution $Cu_2ZnSn(S,Se)_4$[12], whereas slightly lower efficiencies are reported for both endmembers Cu_2ZnSnS_4 (8.4 % [13]) and $Cu_2ZnSnSe_4$ (9.7 % [14]). From an environmental point of view the usage of selenium free material would be clearly preferable to solar cells based on a mix of sulfide-selenide $Cu_2ZnSn(S,Se)_4$. Pure sulfide kesterite would combine optimal properties for solar energy conversion with the benefits of using a compound composed of only environmental friendly, earth abundant, and cost efficient elements.

A more detailed review of the $Cu_2ZnSnSn_4$ compound, its already known properties and the chronological development as a material for solar cells, is given in section 2.1. In order to become a promising and viable photovoltaic material for production on an industrial scale, further extensive research in the field of kesterite is necessary. Still, several questions about the fundamental characteristics of the kesterite material, particularly with regard to structural aspects, remain to be answered.

1.4. Aims of the thesis

The investigations in the present work focus on the quaternary sulfide Cu_2ZnSnS_4 and the properties of the bulk material as a powder. The aim of the research is to gain a deeper insight into the structural characteristics of the absorber material and to get a profound understanding of the correlation between the crystal structure and the materials chemical and physical properties.

Record efficiencies of kesterite devices still not meet the requirements for commercialization. For the preparation of promising and competitive solar cells, it is essential to have a comprehensive knowledge of the fundamental characteristics of the thin film material. Due to cooperative phenomena there is a close structure-function relationship in crystalline solids. Chemical, physical, optical, or electronic properties of a solid material strongly depend on its crystal structure.

In the here-presented study an attempt is made to overcome major challenges concerning the properties of CZTS compound. Following goals were set in order to elucidate structural questions and to carry forward current research progress in the field of kesterite.

First of all, the aim was the development of a novel easy and fast synthesis process for the preparation of phase pure CZTS powder with good crystallinity and controlled composition. Second, CZTS material with different chemical composition or annealed at different temperatures should be prepared. This should enable the full disclosure of key structural features of the compound, especially concerning ordering of the cations, occurrence of intrinsic defects and their correlation with the composition.

These topics are of great scientific interest as they can be essential for the optimization of the kesterite material as an absorber layer for PV applications.

2. Theoretical Background

2.1. Kesterite Cu_2ZnSnS_4 – an overview

This chapter mainly focuses on the general properties of kesterite and will give a brief overview of the Cu-Zn-Sn-S material system. It will provide information about the quasi-ternary system, the crystal structure of Cu_2ZnSnS_4 as well as all possible secondary phases and the phase equilibria of the quasi-binary systems that limit the Cu_2S-SnS_2-ZnS system. Additionally, occurring intrinsic point defects, optical/electronic properties, and solar device characteristics will be discussed.

2.1.1. The Cu-Zn-Sn-S material system

A phase diagram illustrates the thermodynamic equilibrium state of a materials system as a function of different variables such as temperature, pressure, and composition. The construction of phase diagrams of material systems, involving four or more elements, is very complex and only possible in three dimensions. In order to ease the representation of a quaternary system one degree of freedom must be fixed, for example by setting the concentration of one element in the system. In this way, a 2-dimensional quasi-ternary section can be obtained. In the Cu-Zn-Sn-S material system a phase diagram with the end members Cu_2S, ZnS, and SnS_2 can be created by fixing the amount of sulfur.

Until now only a limited number of experimental data is given in literature on the quasi-ternary phase diagram Cu_2S-ZnS-SnS_2. In an early study of Moh [16] who examined the system at 600 °C, Cu_2ZnSnS_4 (CZTS) is the only quaternary phase. More recent experimental investigations of the quaternary material system have been performed by Olekseyuk et al. [15]. Their work is based on the investigation of samples prepared in evacuated silica ampoules at an annealing temperature of 670 K (397 °C). The analysis of the phase equilibria in the system was carried out using differential thermal (DTA), X-ray phase (XPA), and microstructure (MSA) analysis methods. Based on these experimental results it was possible to create a liquidus surface projection of the quasi-ternary phase diagram and to establish an isothermal section at 670 K, which is depicted in Figure 2.1. Besides the phase Cu_2ZnSnS_4, a second quaternary phase, $Cu_2ZnSn_3S_8$, was introduced in the Cu_2S-ZnS-SnS_2 system. This Sn-rich compound is reported to crystallize in a tetragonal structure with almost similar lattice parameters as for Cu_2ZnSnS_4, and is formed
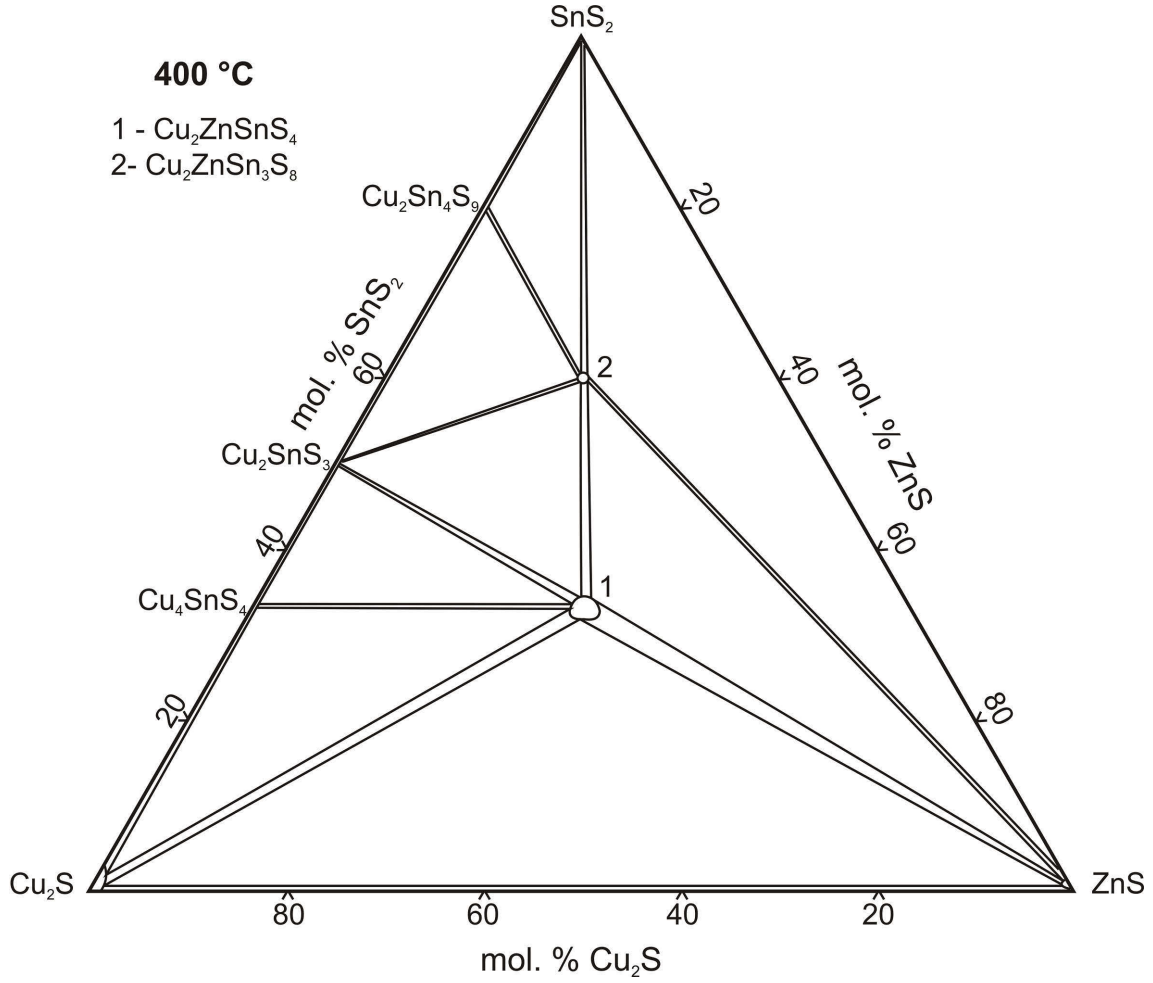
Figure 2.1.: Quasi-ternary phase diagram of the system Cu_2S-ZnS-SnS_2 at $670\,K$ according to Olekseyuk et al. [15]. Region 1 represents the homogeneity region of CZTS.

by the reaction of SnS_2 with CZTS below $700\,°C$. Although analogous compounds, so called quaternary thiospinels $Cu_2XSn_3S_8$ (X = Cd, Ni, Co), are known to occur in nature, the existence of $Cu_2ZnSn_3S_8$ could not been proven yet. No further literature data on this quaternary sulfide is available, except a recent study of a Sn-rich thin film sample with a composition close to $Cu_2ZnSn_3S_8$ [17]. No indication for the presence of the quaternary phase was found in this work. In summary, it can be said that, according to current literature, Cu_2ZnSnS_4 seems to be the only stable quaternary phase in the Cu-Zn-Sn-S material system.

In Figure 2.2 the phase diagram of the Cu_2SnS_3 (CTS)-ZnS quasi-binary system is depicted. It corresponds to a triangulating section of the ternary Cu_2S-ZnS-SnS_2 system and was established by Olekseyuk et al. [15]. According to their investigations, CZTS forms at $1253\,K$ ($980\,°C$) by the peritectic reaction Liquid (L) + α-ZnS ↔ Cu_2ZnSnS_4, where α-

ZnS is the sphalerite modification of ZnS. At the peritectic point the mixture contains 12.5 mol% α-ZnS. CZTS is represented as a line compound, so it is expected, that ZnS shows no significant solubility in it. A similar representation of the pseudo-binary phase diagram is given in the work of Moh [16], who created a Cu$_2$ZnSnS$_4$-ZnS cross section. In conclusion, as outlined in Figure 2.1 and 2.2 the homogeneity region of single phase CZTS is rather small and secondary phases are likely to form when deviating from the stoichiometric composition. All possible occurring phases and related phase diagrams will be discussed in subsection 2.1.4.
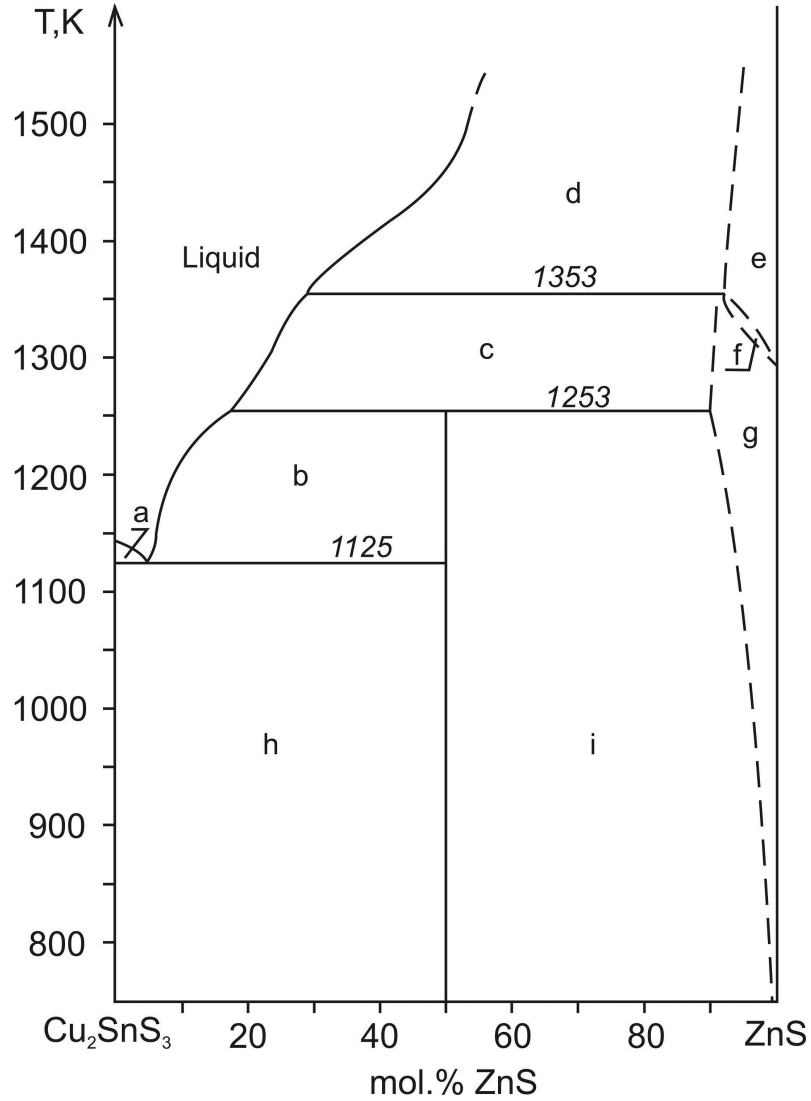
Figure 2.2.: Phase diagram of the Cu$_2$SnS$_3$-ZnS quasi binary system according to Olekseyuk et al. [15] .

2.1.2. Crystal structure

Cu_2ZnSnS_4 is a member of the adamantine compound family. The basis of this compound group is the cubic diamond structure, space group $Fd\bar{3}m$ [18] (see Figure 2.3). It is also possible to describe the adamantine compound family starting from the hexagonal diamond structure (lonsdaleite) going to monoclinic wurtz-kesterite, but as this hexagonal branch is not part of the study, it will not be discussed. The cubic diamond structure can be described by two overlapping face centered cubic (fcc) sublattices. Each atom is tetrahedrally coordinated having four covalent bonds to its nearest neighbors, which requires four valence electrons. Starting from this cubic diamond structure different multinary compounds can be derived under the provision that the average number of valence electrons per atom is four and consequently the tetrahedral bonding character is maintained. In these multinary compounds the anions and cations occupy one of the fcc substructures, respectively.

When substituting the group IV element with one element with two and one with six valence electrons the average number of valence electrons per atom remains four and a binary compound with the general formula $A^{II}B^{VI}$ can be derived. One common representative is the binary sulfide ZnS, which crystallizes in the cubic sphalerite-type structure, the symmetry is lowered to space group $F\bar{4}3m$ (See Figure 2.3).

Performing a second isoelectronic substitution the ternary chalcopyrite-type crystal structure can be obtained (See Figure 2.3). The group II element, in our case Zn, is replaced by one group I element (Cu) and by a second element that has three valence electrons (In/Ga), respectively, leading to the semiconductor materials $CuInS_2$ or $CuGaS_2$. In contrast to sphalerite, in chalcopyrite two cation species need to be distributed over the lattice in an ordered way. Therefore, the fcc unit cell has to be doubled along the c-axes (z-direction), resulting in a body-centered tetragonal unit cell. The symmetry is reduced and the space group changes from $F\bar{4}3m$ to $I\bar{4}2d$. With the doubling of the unit cell in z-direction in the substitution step sphalerite $\rightarrow$ chalcopyrite and the resulting change from a cubic to a tetragonal structure, two additional structural degrees of freedom are introduced [19]. As the sulfur atoms are no longer surrounded by only one cation species, irregular interactions between the anion and the neighboring cations occur. Hence, unequal bond lengths and angles arise ($r_{A-X} \neq r_{B-X} \neq r_{C-X}$), resulting in a lattice parameter ratio $c/2a \neq 1$, which is called tetragonal distortion η. Furthermore, an anion displacement u is observed. Due to the differing bond lengths the sulfur anion shifts from the ideal tetrahedral site. When lowering the symmetry, the anion displacement increases. In the sphalerite-type structure the anion occupies the ideal tetrahedral position $(1/4, 1/4, 1/4)$, whereas in the chalcopyrite-type structure already one atomic coordinate is free $(x, 1/4, 1/8)$.

Repeating the isoelectronic substitution leads to the formation of a compound with the general formula $A^I_2B^{II}C^{IV}X^{VI}_4$, e.g. Cu_2ZnSnS_4. For this compound two tetragonal

structures are proposed in literature: the stannite-type and the kesterite-type structure, named after the mineral where this structure was first observed, Cu$_2$FeSnS$_4$ for stannite and Cu$_2$(Zn,Fe)SnS$_4$ for kesterite, respectively [20]. Generally, both structures can be described as cubic closed packed (ccp) array of anions and half of the tetrahedral voids are filled with cations, but different distribution schemes of the three cation species Cu$^+$, Zn^{2+}, and Sn^{4+} are possible. In the stannite-type structure the cations are arranged in alternating zinc-tin and copper-copper layers at $z = 0$, $1/2$ and $z = 1/4$, $3/4$, respectively. Regarding the Wyckoff positions of stannite, zinc occupies the $2a$ $(0, 0, 0)$ position, copper the $4d$ $(0, 1/2, 1/4)$ position and tin lies on the $2b$ $(0, 0, 1/2)$ position. In the kesterite-type structure, on the other hand, a symmetry decrease is occurring by changing the metal ordering. In this structure type CuZn layers ($z = 1/4$, $3/4$) alternate with CuSn layers ($z = 0$, $1/2$). Except tin, which remains on position $2b$, differences are found concerning the Wyckoff positions. The $2a$ position is occupied by one copper, whereas zinc and the remaining copper are ordered at $2c$ and $2d$ position, respectively, resulting in the reduction of the symmetry to space group $I\overline{4}$. The anion displacement is further increased with symmetry degradation. In stannite-type structure the anion now occupies the position $8i$ (x, x, z) and in the kesterite-type structure three free atomic coordinates $8g$ (x, y, z) are reached.

First-principle calculations were performed to determine the stabilities of the different modifications of CZTS [11, 21, 22]. According to these works, the kesterite-type structure has the lowest total energy and is the most stable modification, even though the formation of the stannite-type structure seems to be facile due to the small energy difference. By using neutron diffraction and solid NMR measurements it could be confirmed that Cu$_2$ZnSnS$_4$ crystallizes in the kesterite-type structure [23–25].

Also, a so called disordered kesterite-type structure has to be considered. This structure type can be described by partial or complete disorder of Cu and Zn on positons $2c$ and $2d$ and was already detected in neutron diffraction studies of CZTS powder samples [25, 26]. The difference between the two cation positions $2c$ and $2d$ vanish, thus complete disordered kesterite can be again described by the higher symmetric space group $I\overline{4}2m$, with Zn and Cu occupying the $4d$ position. According to *ab initio* calculations Cu/Zn disorder is likely to occur as the exchange of Cu and Zn atoms in the CuZn layer ($z = 1/4$ and $3/4$) needs only little energy [27, 28].

Near-resonant Raman measurements on Zn-rich CZTS thin films were carried out to track the order-disorder transition from kesterite- to disordered kesterite-type structure determining a critical temperature of $260 \pm 10\,°C$ by Scragg et al. [29]. Furthermore, at $240\,°C$ a kink in the temperature dependent lattice parameter was observed in *in situ* high temperature X-ray diffraction measurements [30], which could be an indication for an order-disorder transformation.
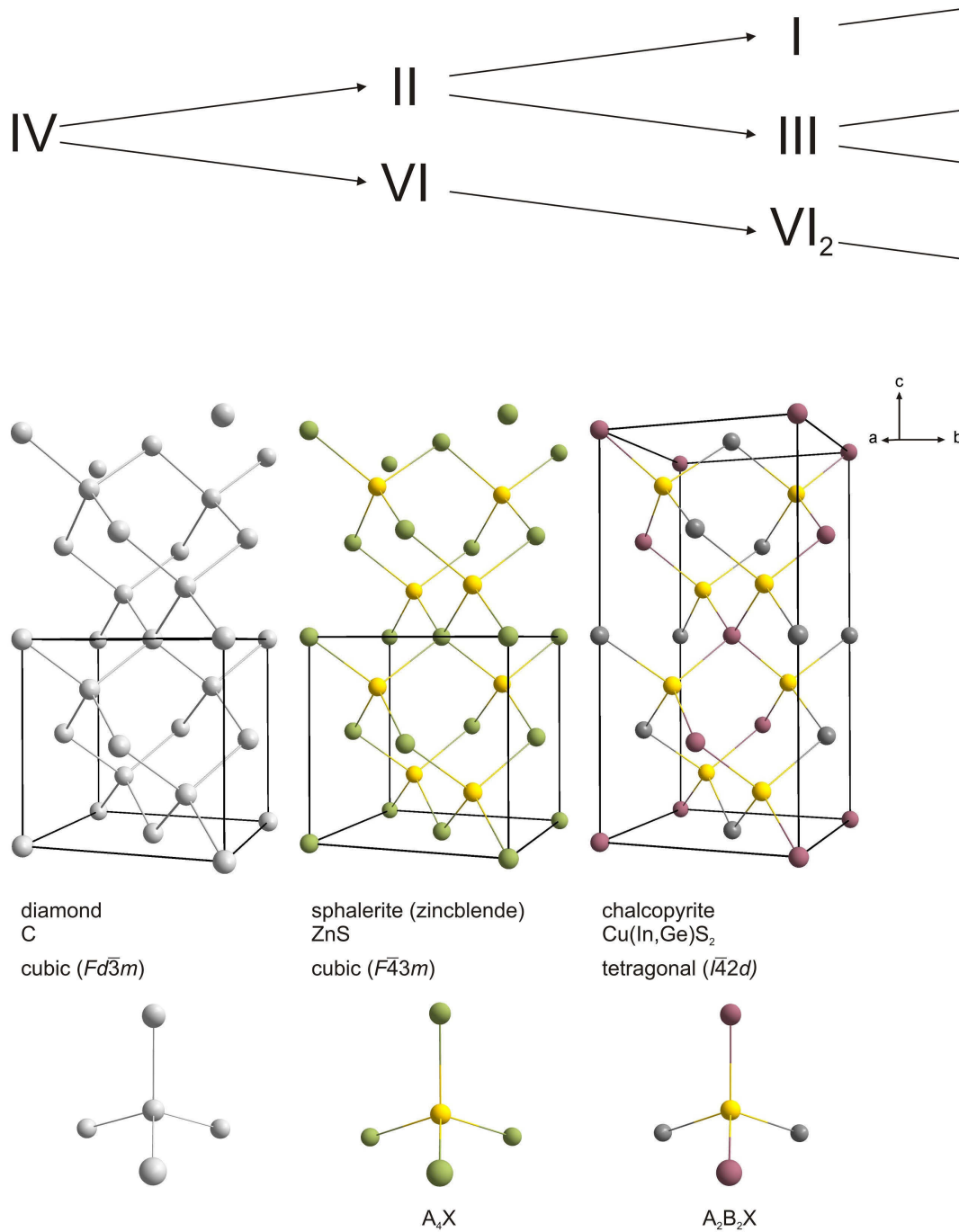
Figure 2.3.: The adamantine compound family. Top: Substitutions scheme, roman numbers give the valence state of the cations and anions, respectively. Middle: Crystal structure models, type structure denotation, compound formula, crystal system, and space group symbol. Bottom: Cation tetraedra for each crystal structure.

I_2

II

IV

VI_4

stannite
Cu_2ZnSnS_4
tetragonal ($I\bar{4}2m$)

kesterite
Cu_2ZnSnS_4
tetragonal ($I\bar{4}$)

disordered kesterite
Cu_2ZnSnS_4
tetragonal ($I\bar{4}2m$)

C
Cu
Cu/Zn
In/Ga
Sn
Zn
S

A_2BCX

A_2BCX

A_2BCX
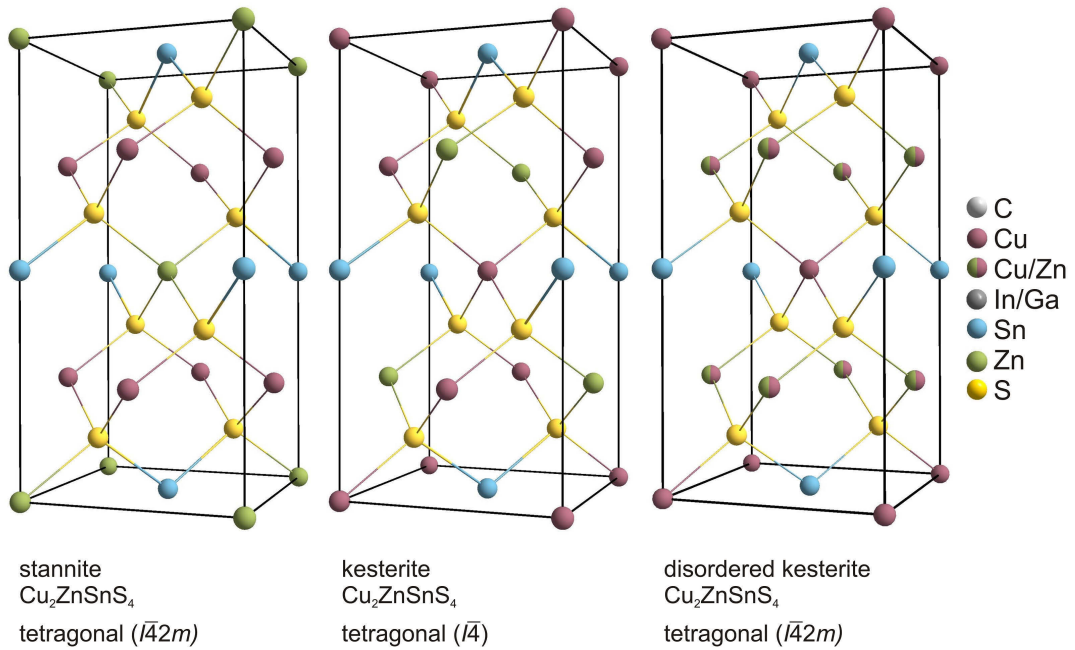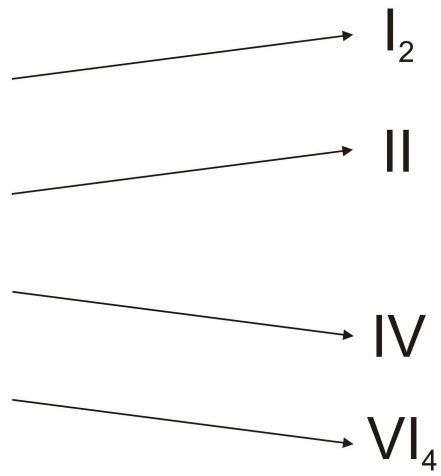
Table 2.1.: Overview of structural details of proposed structure-types of CZTS including Wyckoff positions and atomic coordinates.

Structure type	Space group	Cation sites				Anion site
		Cu1	Cu2	Zn	Sn	S
stannite	$I\bar{4}2m$	$4d\,(0,1/2,1/4)$		$2a\,(0,0,0)$	$2b\,(0,0,1/2)$	$8i\,(x,x,z)$
kesterite	$I\bar{4}$	$2a\,(0,0,0)$	$2c\,(0,1/2,1/4)$	$2d\,(0,1/2,3/4)$	$2b\,(0,0,1/2)$	$8g\,(x,y,z)$
disordered kesterite	$I\bar{4}2m$	$2a\,(0,0,0)$	$4d\,(0,1/2,1/4)$		$2b\,(0,0,1/2)$	$8i\,(x,x,z)$

All three Cu_2ZnSnS_4 structure types are depicted in Figure 2.3 and an overview of the Wyckoff positions is shown in Table 2.1.

In a theoretical work by Paier et al. [21] additional tetragonal modifications of the kesterite-type structure were introduced, exhibiting space groups $P\bar{4}2c$, $P\bar{4}2_1m$, and $P2$, respectively. All of them can be regarded as modifications of kesterite where two ions of the cation sublattice are exchanged. Either, Cu and Zn are exchanged in the layer $z=1/4$ (space group $P\bar{4}2c$), Cu and Zn are exchanged between the layers $z=1/4$ and $3/4$ leading to complete Cu- and Zn-layers (space group $P\bar{4}2_1m$), or one Cu atom ($z=1/2$) is exchanged with one Zn-atom at $z=3/4$ (space group $P2$). Space group $P2$ can be seen as a structural mixture between stannite (layers $z=1/2$ and $3/4$) and kesterite (layers $z=0$ and $1/4$). Phases crystallizing in space groups $P\bar{4}2_1m$ and $P2$ are not likely to occur because they are significantly higher in energy ($200-400\,$meV [21]) than the kesterite-type structure. CZTS crystallizing in space group $P\bar{4}2c$ is only slightly less stable than the kesterite-type structure [21], but until now it has never been reported in experimental studies.

A structural phase transition in CTZS was reported by Schorr and Gonzalez-Aviles [30]. They performed in situ high-temperature X-ray diffraction measurements of a CZTS powder sample using synchrotron radiation, and 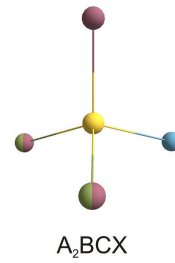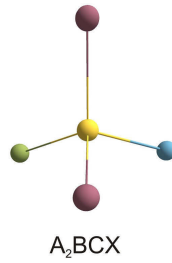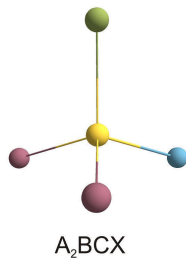revealed the existence of a structural phase transition from the tetragonal kesterite-type to the cubic sphalerite-type structure (space group $F\bar{4}3m$), which occurs between $866-883\,°C$, where the two phases coexist.

2.1.3. Defects

Although it is nicely possible to represent phase equilibria and compositions in the Cu-Zn-Sn-S material system with the above described ternary phase diagram, in CZTS literature the cation ratios Cu/(Zn+Sn) and Zn/Sn are mainly used to describe the composition of the CZTS-material [31–35]. A representation of these cation ratios is given in Figure 7.1. Both ratios are equal to one, when the CZTS-sample is stoichiometric. In literature, the cation ratios of the majority of synthesized CZTS samples deviate from these nominal values, thus

Table 2.2.: The electric character of CZTS related intrinsic defect

Electronic character	Point defect
Acceptor	Cu$_{Zn}$, Cu$_{Sn}$, Zn$_{Sn}$
	V$_{Cu}$, V$_{Zn}$, V$_{Sn}$
Donor	Zn$_{Cu}$, Sn$_{Cu}$, Sn$_{Zn}$
	Cu$_i$, Zn$_i$, Sn$_i$

the samples are off-stoichiometric. The significant off-stoichiometry in CZTS samples can be attributed to the existence of a considerable concentration of intrinsic defects or defect clusters. A number of theoretical works investigated the potential intrinsic defects, their formation energy and their effect on the bandgap of CZTS [11, 27, 28, 35–38]. Different defects types are possible in CZTS:

- Antisites defects A$_B$, indicating an atom A replacing an atom B on the lattice site (Cu$_{Zn}$, Cu$_{Sn}$, Zn$_{Cu}$, Zn$_{Sn}$, Sn$_{Cu}$, Sn$_{Zn}$).

- Vacancies V$_A$, characterized by an unoccupied lattice site of atom A (V$_{Cu}$, V$_{Zn}$, V$_{Sn}$, V$_S$).

- Interstitials A$_i$, corresponding to an atom A at an interstitial site (Cu$_i$, Zn$_i$, Sn$_i$).

The formation energy of these defects as a function of the chemical potentials has been calculated by Chen et al. [27, 35–37]. In Figure 2.4 (a) the formation energy of point defects of CZTS as a function of the chemical potential according to Ref. [27] are depicted. As shown in their calculations, Cu$_{Zn}$ is the defect with the lowest formation energy, pointing out that this antisite is the dominant point defect in CZTS. Among all other intrinsic defects, V$_{Cu}$, V$_{Zn}$, Cu$_{Sn}$, and Zn$_{Sn}$ have also relatively low formation energy.

Defects can be categorized in acceptor and donor defects (see Table 2.2). In Figure 2.4 (b,c) the formation energy of defects clusters in CZTS as a function of the chemical potential according to Ref. [27] is depicted. It can be seen that the $[Cu_{Zn}^- + Zn_{Cu}^+]$ defect complex has the lowest formation energy with $0.21\,$eV/pair. The facile formation of this defect cluster was already confirmed by experimental work [25, 26], where partial or complete Cu/Zn disorder in the CuZn layer ($z = 1/4$ and $3/4$) was reported. As already mentioned above, a statistically distribution of Cu and Zn is leading to the so called disordered kesterite-type structure (Figure 2.3). The formation energy of other antisite pairs ($[Zn_{Sn}^{2-} + Sn_{Zn}^{2+}]$ and $[Cu_{Sn}^{3-} + Sn_{Cu}^{3+}]$) is significantly higher, reaching an energy of $2\,$eV/pair for the latter one.

For defect clusters that involve atom exchange, $[2Cu_{Zn}^- + Sn_{Zn}^{2+}]$ has the lowest formation energy according to calculations of Chen et al. [35] (see Figure 2.4 (c)) with around $0.2 - 0.6\,$eV depending on the chemical potential. Other low energy complexes are $[V_{Cu}^- + Zn_{Cu}^+]$

or $[Zn_{Sn}^{2+} + 2Zn_{Cu}^{+}]$. In general it can be seen, that the overall formation energy of the defect complexes is notably lower than their corresponding isolated point defects.
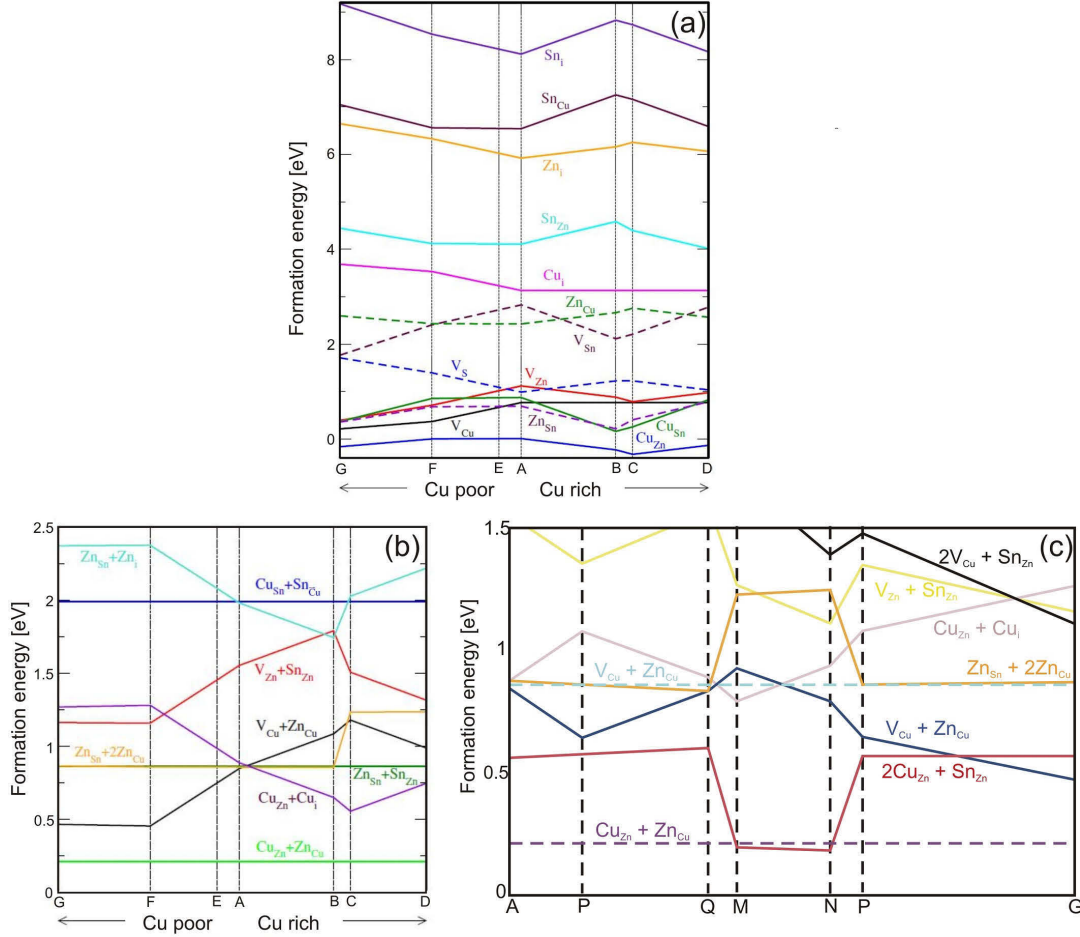
Figure 2.4.: Formation energy of isolated point defects (a) and charge compensating defect complexes (b) according to Chen et al. [27] and (c) according to Chen et al. [35] in CZTS at different chemical potentials

First systematic experimental work on the ability of the CZTS phase to deviate from the Cu_2ZnSnS_4 stoichiometric composition, while keeping the structure, was done by Lafond et al. [33, 34].They proposed four different off-stoichiometric types that can be described by certain cation substitution reactions and the formation of corresponding defect complexes.

- A-type: In this Cu-poor/Zn-rich off-stoichiometric type zinc on copper antisites and copper vacancies are present forming the defect complex $[Zn_{Cu}^{+} + V_{Cu}^{-}]$.

- B-type: Another Cu-poor/Zn-rich type is characterized by the substitution of copper and tin forming the defect complex $[2Zn_{Cu}^{+} + V_{Sn}^{2-}]$.

- C-type: This type can be seen as the reverse of the B-type. It is Cu-rich/Zn-poor with copper on tin antisites forming the defect complex $[2Cu_{Zn}^- + Sn_{Zn}^{2-}]$.

- D-type: This type is another Cu-rich/Zn-poor type and the opposite of the A-type. Zinc antisites and copper interstitials are present forming the defect complex $[Cu_{Zn}^- + Cu_i^+]$.

Recently, Valle-Rios et al. [31] reported on the flexibility of CZTS(Se) composition of kesterite powder samples. They introduced a new off-stoichiometry type, the F-type. The reverse type would be the E-type which first showed up in a work by Gurieva et al. [32].

- E-type: This Cu-poor/Zn-poor type can be characterized by two different substitution schemes, either forming $[Sn_{Zn}^{2+} + 2V_{Cu}^-]$ or $[Sn_{Cu}^{3+} + V_{Cu}^- + V_{Zn}^{2-}]$ defect clusters.

- F-type: It is the opposite of the E-type. Again, two defect complexes are possible, namely $[Zn_{Sn}^{2-} + 2Cu_i^+]$ or $[Cu3_{Sn}^- + Cu_i^+ + Zn2_i^+]$.
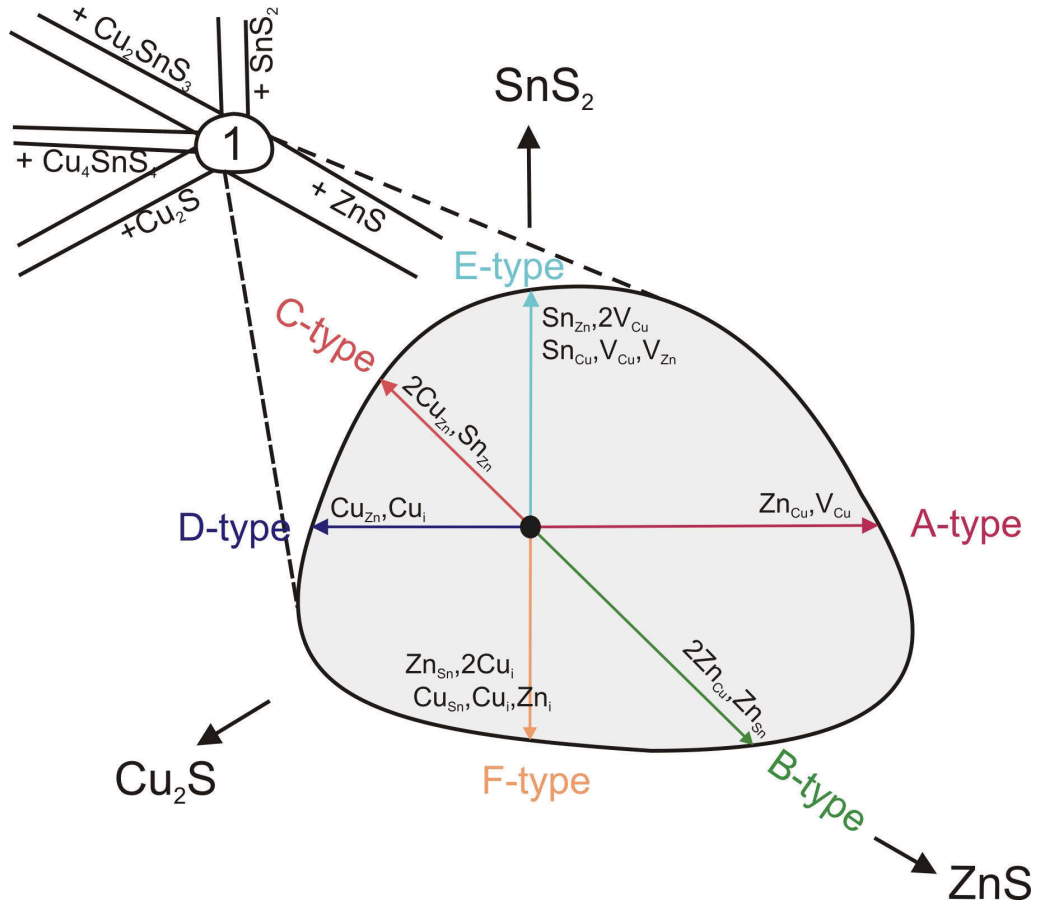
Figure 2.5.: Homogeneity range of CZTS (1) in the ternary phase diagram (see Figure 2.1) according to Scragg [39]. The lines correspond to the CZTS off-stoichiometric types.

Lafond et al. [33] were able to synthesize single phase A-, B-, and C-type off-stoichiometric CZTS samples. Referring to the above mentioned generation of CZTS related defect complexes [14, 22] (Figure 2.4 (b,c)), these off-stoichiometric types seem to be generally formed easily, as their formation energy is relatively low. No single phase D-type sample has been reported in literature so far, apart from samples having C-D- and D-F-type mixtures with kesterite as major phase, but additional secondary phases were obtained by Valle-Rios et al. [31]. They could also prepare samples having B-F-type mixture up to an F-type fraction of 76 %. However, no additional information about single phase CZTS exhibiting E- or F-type can be found in literature. The formation energy for the defect complexes of E- and F-type has not been calculated up to now, but the high formation energy of Sn_{Cu} and Zn_i compared to other point defects in the CZTS system make single E- or F-type samples rather unlikely. A summary of all off-stoichiometric types, including their cation substitution reactions is shown in Table 7.1. In Figure 2.6 a schematic representation of the homogeneity region of CZTS in the ternary phase diagram is depicted, whereas in Figure 7.1 the cation ratio plot Cu/(Zn+Sn) vs. Zn/Sn is shown, both including six lines that correspond to the off-stoichiometric CZTS types.

Despite the efforts that have been made to understand the distinctive feature of CZTS to tolerate deviations from the stoichiometric composition, further investigations are required to experimentally clarify the defects that are produced by off-stoichiometric samples and their impact on opto-electronic properties of CZTS.

2.1.4. Related systems and compounds

In this section, the quasi-binary phase diagrams, limiting the above described quasi-ternary system Cu_2S-ZnS-SnS_2 and the corresponding two-element systems will be discussed briefly. The chapter closes with an overview of all potential secondary phases that can be formed besides CZTS. A summary of the available structure data and other relevant information is given in Table 2.3.

2.1.4.1. Cu-Zn-S

Different experimental data on this material system can be found in literature. In early works of Moh [40] and Clark et al. [41] reports on ternary compounds with the formula Cu_5ZnS_6 and a more copper-poor phase close to the composition Cu_3ZnS_4 can be found, respectively. However, when repeating the experiments in the system, Moh [16] could not observe any Cu-Zn-Sn ternary phases and his former results were attributed to contamination by iron and oxygen. Furthermore, in later studies of Craig and Kullerud [42] and Trishchuk et al. [43] no evidence for the existence of ternary phases was found. In Fig-

ure 2.6(a) the phase diagram of the Cu$_2$S-ZnS quasi-binary system according to Olekseyuk et al. [15] is depicted.

2.1.4.2. Zn-Sn-S

Neither Moh [16] nor Olekseyuk et al. [15] reported the formation of ternary phases in their studies on the system Zn-Sn-S. Based on a detailed series of experiments Olekseyuk et al. [15] established the pseudo-binary phase diagram with the endmembers ZnS and SnS$_2$, which is depicted in Figure 2.6(b). The ZnS-SnS$_2$ system can be characterized by a very low solubility within the two components, reaching values up to 5 and 1 mol%, respectively.
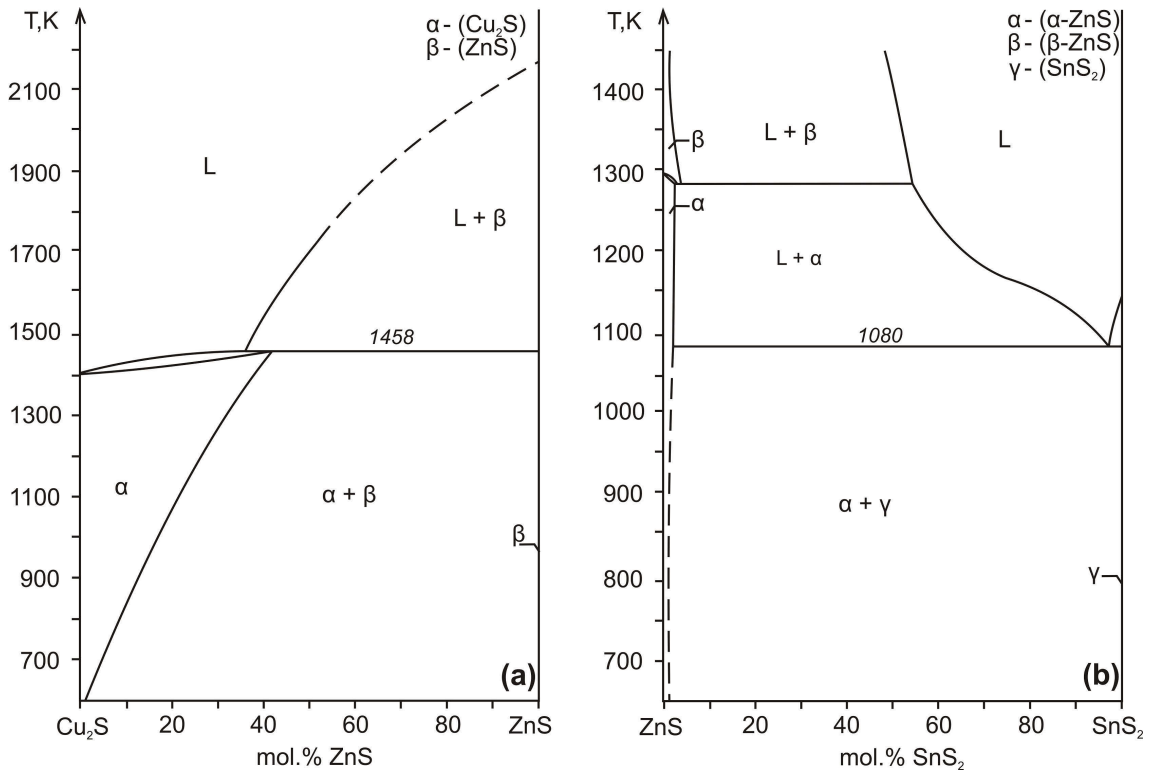
Figure 2.6.: Binary phase diagram of the systems Cu$_2$S-ZnS (a) and ZnS-SnS (b) according to Piskach et al. [44].

2.1.4.3. Cu-Sn-S

The Cu-Sn-S system has been investigated repeatedly [16, 44–50]. It is a rather complex ternary system and the existence of different ternary phases is reported. Most of the detected phases are situated along the quasi-binary tie-line Cu$_2$S-SnS$_2$ or close to it. A representation of the quasi-binary phase diagram after Piskach et al. [44] is depicted in Figure 2.7.

Moh [16, 45] studied the ternary phase diagram Cu-Sn-S at a temperature of $600\,°C$ and reported the formation of ternary phases, namely Cu_4SnS_4, Cu_2SnS_3 (mohite), and a phase with a composition from $Cu_2Sn_2S_5$ to $Cu_2Sn_3S_7$. All three lie on the Cu_2S-SnS_2 tie line. For an isothermal section at $500\,°C$ Wu et al. [48] found the same three phases and additionally reported the formation of two phases next to the quasi-binary tie line, the tetragonal $Cu_{10}Sn_2S_3$ and $Cu_5Sn_2S_7$, for which they did not give any structural data.
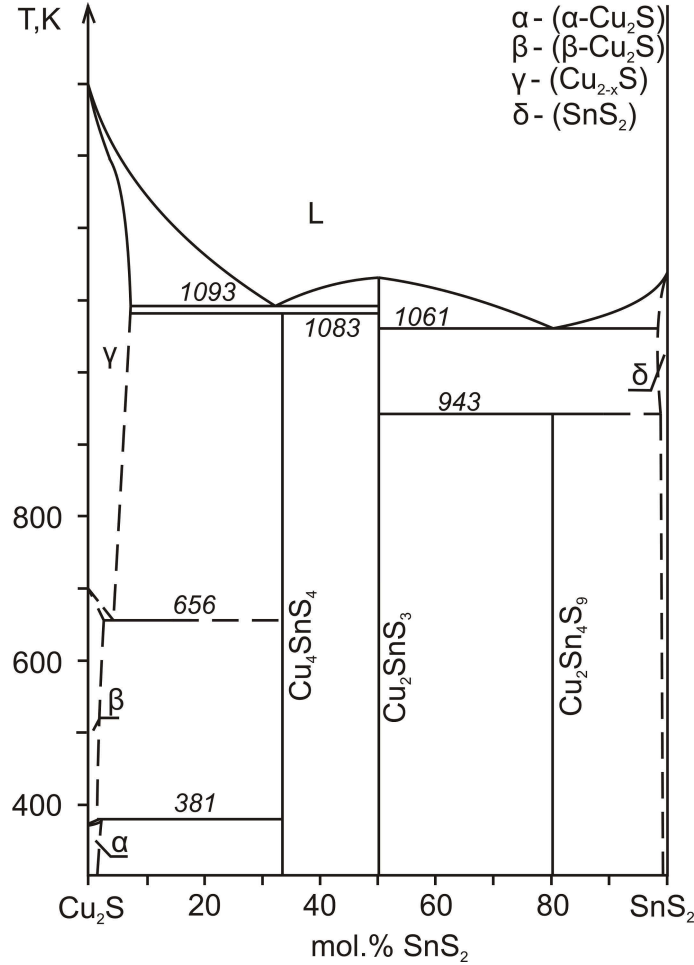
Figure 2.7.: Binary phase diagram of the systems Cu_2S-SnS (a) according to Olekseyuk et al. [15].

The Cu-rich compound Cu_4SnS_4, which can be found in other different works [44, 46–49, 51], crystallizes in an orthorhombic structure. The polymorphic phase Cu_2SnS_3 (often referred as CTS) has been reported to crystallize either in tetragonal [45, 52], triclinic [16, 46, 48], or monoclinic structure [47, 53]. At temperatures above $775 - 780\,°C$ the cubic high temperature modification of Cu_2SnS_3 is formed [16, 45, 54], which melts incongruently at

842 °C. For both phases, Cu_4SnS_4 and Cu_2SnS_3, no evidence of the solubility in adjacent phases can be found in literature.

According to Moh [16] the third phase has a composition range from $Cu_2Sn_2S_5$ to $Cu_2Sn_3S_7$. However, in studies of Wang et al. [46] and Wu et al. [48] the existence of $Cu_2Sn_2S_5$ was doubted. $Cu_2Sn_3S_7$ was assigned to a monoclinic structure [16, 46, 48]. Khanafer et al. [47] published a paper, where the formation of an additional cubic ternary phase on the Cu_2S-SnS_2 tie line close to $Cu_2Sn_3S_7$, namely $Cu_2Sn_4S_9$, is reported, whereas in another publication of Wang et al. [50] it was described as $Cu_2Sn_{3.5}S_8$. In recent investigations by Fiechter et al. [49] the composition of this third compound could be finally clarified. It was observed that the phase has a wide homogeneity field, ranging from $75-80$ mol% SnS_2 at elevated temperatures, resulting in the composition $Cu_2Sn_{3+x}S_{7+2x}$. The crystal structure of the compound was described as thio-spinel defect structure.

A fourth ternary phase in the Cu_2S-SnS_2 system was introduced by Khanafer [47], which is formed at high temperatures. Fiechter et al. [49] detected, that this $Cu_4Sn_3S_8$ is only stable between 685 and 785 °C. No crystal data for this phase is given. In another study by Piskach et al. [44] no evidence for this high temperature phase was found and consequently not included in their phase diagram version of the Cu_2S-SnS_2 system (see Figure 2.7).

Near the Cu_2S-SnS_2 section of the ternary Cu-Sn-S system another phase occurs with the empirical formula Cu_3SnS_4 (Kuramit). The existence of this compound was already reported by Moh [40, 55], who claimed that the compound is polymorphic with superstructures of the wurtzit and zincblende structure types. According to Kovalenker et al. [56] Cu_3SnS_4 crystallizes in a tetragonal structure. Other works confirmed these findings [57–59], different authors reported an orthorhombic structure [54, 60]. A phase with the composition Cu_4SnS_6 is reported by several authors. According to Wang [61] and Chen [62] this compound crystallizes in a layered structure with rhombohedral symmetry.

2.1.4.4. Cu-S

Investigations on this complex binary system were carried out by Chakrabarti and Laughlin [63], who establish a phase diagram version shown in Figure A.4 of the appendix. Several crystalline phases have been investigated in the system: chalcocite (Cu_2S), djurleite ($Cu_{\sim 1.95}S$), digenite ($Cu_{2-x}S$), anilite ($Cu_{1.75}S$), and covellite (CuS). Furthermore, the metastable phase villamaninite (CuS_2) is known. The Cu-rich compound Cu_2S crystallizes at room temperature in a monoclinic modification (α- Cu_2S). Above a temperature of 104 °C the phase transforms to a hexagonal structure (β-Cu_2S) and at 435 °C β-Cu_2S decomposes to (Cu) and the less Cu-rich phase $Cu_{2-x}S$. This cubic compound has a broad phase field and the variable x can reach a value up to $x = 0.3$. The Cu-rich boundary of digenite is approximately at the stoichiometric composition Cu_2S and has a melting point of 1130 °C. Digenite with a Cu-poor composition is stable above 72 °C. Below this temper-

ature $Cu_{2-x}S$ turns to the orthorhombic anilite phase. The orthorhombic djurleite has a nominal composition of $Cu_{1.95\pm x}S$ and is stable up to $72-93\,°C$ depending on the actual at%-amount of copper ($x = 0.015$). The hexagonal compound covellite of stoichiometry CuS decomposes according to a peritectic reaction at $507\,°C$ to digenite and sulfur melt.

2.1.4.5. Zn-S

According to the phase diagram in Figure A.5 of the appendix, which was established by Sharma and Chang [64], ZnS is the only binary phase that forms in the system. However, ZnS is a polymorphic phase and the phase transition from low temperature α-ZnS to the high temperature form β-ZnS occurs at $1020\,°C$. α-ZnS crystallizes in the cubic sphalerite-type structure, whereas β-ZnS corresponds to the hexagonal wurtzite-type structure. The melting point of ZnS was determined at $\sim 1718\,°C$. For wurtzite a numerous of polytypes are known from literature [65, 66]. These polytypes show a different stacking sequence along the c-axis. Additionally, a metastable rhombohedral modification [67] and a high pressure phase of ZnS [68] were reported.

2.1.4.6. Sn-S

A detailed description of this binary system was published by Sharma and Chang [69], which is depicted in Figure A.6 of the appendix. According to their investigations, three stable binary compounds are present in the system. For all three phases herzenbergite (SnS), ottemannite (Sn_2S_3), and berndtite (SnS_2) high temperature modifications are formed. SnS exists in two polymorphic modifications. The transition temperature from α-SnS to the high temperature form β-SnS lies at $602\,°C$. β-SnS, which can dissolve excess sulfur up to $50.5\,at\%$, melts congruently at $880\,°C$. Both forms crystallize in an orthorhombic crystal structure. Besides the orthorhombic low temperature form of Sn_2S_3, three high temperature modifications up to the peritectic melting temperature of $760\,°C$ were reported by Moh [70]. The high temperature forms are able to dissolve additional sulfur as well as tin. In Sn_2S_3, the Sn atoms have a mixed oxidation state of $+$ II and $+$ IV. The sulfur-rich phase SnS_2 crystallizes in a hexagonal structure. The high temperature modification β-SnS_2 is slightly tin-rich and melts congruently at $865\,°C$.

Table 2.3.: Secondary phases for the Cu-Zn-Sn-S system. Mineral name, crystal structure, and sulfur content is given for each phase.

Phase	Mineral name	Crystal system	Space group	at% S	Ref.
Quaternary					
Cu_2ZnSnS_4	kesterite	tetragonal	$I\bar{4}$	50	[71]
Cu_2ZnSnS_4	stannite	tetragonal	$I\bar{4}2m$	50	[34]
Cu_2ZnSnS_4(HT)	-	cubic	$F\bar{4}3m$	50	[30]
Ternary					
Cu_4SnS_4	-	orthorhombic	$Pnma$	44.44	[47]
Cu_2SnS_3	mohite	tetragonal	$I\bar{4}2m$	50	[52]
		triclinic	$P1$		[46]
		monoclinic	Cc		[53]
Cu_2SnS_3 (HT)	mohite	cubic	$F\bar{4}3m$	50	[45]
$Cu_4Sn_3S_8$	-	-	-	53.33	[47]
Cu_3SnS_4	kuramite	tetragonal	$I\bar{4}2m$	50	[56]
		orthorhombic	$Pmn2_1$		[54]
Cu_4SnS_6	-	rhombohedral	$R\bar{3}m$	54.54	[62]
$Cu_2Sn_{3+x}S_{7+2x}$	-	monoclinic	Cc or $C2/c$	$56.25-58.33$	[46]
		cubic	$F4_132$		[47]
$Cu_{10}Sn_2S_3$	-	tetragonal	-	20	[48]
Binary					
α-Cu_2S	chalcocite	monoclinic	$P2_1/c$	33.33	[63]
β-Cu_2S	chalcocite	hexagonal	$P6_3/mmc$	33.33	[63]
$Cu_{1.95\pm x}S$	djurleite	orthorhombic	$Pmnm$	$33.7-34.1$	[63]
$Cu_{2-x}S$	digenite	cubic	$Fm\bar{3}m$	$35.5-36.2$	[63]
$Cu_{1.75}S$	anilite	orthorhombic	$Pnma$	$36.32-36.40$	[63]
CuS	covellite	hexagonal	$P6_3/mmc$	50	[63]
α-ZnS	sphalerite	cubic	$F\bar{4}3m$	50	[64]
β-ZnS	wurtzite	hexagonal	$P6_3mc$	50	[64]
α-SnS	herzenbergite	orthorhombic	$Pnma$	50	[69]
β-SnS	herzenbergite	orthorhombic	$Cmcm$	$50.0-50.5$	[69, 72]
Sn_2S_3	ottemannite	orthorhombic	$Pnma$	60	[69]
SnS_2	berndtite	hexagonal	$P\bar{3}m1$	66.67	[69]

The most common binary and ternary compounds, which may form as secondary phases in CZTS, include copper sulfides such as CuS, $Cu_{2-x}S$, ZnS, SnS, SnS_2, and Cu_2SnS_3 [31, 35, 73]. The detection of secondary phases is a challenging problem. Some compounds such as SnS, SnS_2, CuS, and Cu_2S can be easily detected using X-ray diffraction techniques, as their crystal structure is differing from CZTS, whereas ZnS and CTS have a similar symmetry and lattice parameters and are difficult to detect. For a reliable way to identify secondary phases, electron microprobe analysis or X-ray absorption spectroscopy can be used. These methods will be discussed briefly in chapter 3. Another common alternative to distinguish secondary phases is Raman spectroscopy. In literature, different studies are found reporting characteristic Raman shifts of CZTS and related secondary phases [74–77].

2.1.5. CZTS as absorber material

The outstanding semiconductor properties of CZTS were already indicated as promising for thin-film applications by Ito and Nakazawa [78] in 1988. Thereafter, a great number of different works focused on the development of the material as absorber layer in thin film devices.

CZTS is a p-type semiconductor and, according to theoretical and experimental studies, the material has a direct band gap of around 1.5 eV [11, 21, 22, 79]. The material shows a high absorption coefficient of $\sim 10^4$ cm^{-1}, which means that the absorption of incoming light occurs within 100 nm of the surface, making the material suitable as thin film photovoltaic absorber layer.

Two main categories can generally be distinguished, when talking about the fabrication of CZTS thin films. In the single-stage process, the whole crystalline film is synthesized in one step. A common technique is the co-evaporation of all corresponding elements onto a heated substrate, a method that is also successfully used for record CIGS devices [80]. On the other hand, so called two-stage processes are applied, which include a variety of available preparation methods. The first step is the preparation of a precursor that contains only the metallic elements or all corresponding elements in an unreacted and non-crystalline form. Different methods are available for this first process, such as sputtering, electron beam evaporation, spray pyrolysis, nanoparticle printing, pulsed laser deposition, or electrodeposition [75, 81–86]. In the second step, the precursor is annealed in sulfur atmosphere, so called sulfurization. This heating induces the crystallization of the film.

The extensive research in the field of CZTS results in a continuous and fast improvement of the solar cell performance. In 2008 an efficiency of 6.7 % was reported by Katagari et al. [82], some years later a value of 8.4 % was reached [13], which is still the highest efficiency for a CZTS based device. This value has been exceeded by devices that additionally contained selenium ($Cu_2ZnSn(S,Se)_4$), produced by Wang et al. [12], who obtained the record efficiencies of 12.6 %.

Despite the significant improvements of CZTS based solar cells, the performances are still far away from the theoretical limit of 30 % [8]. The low open-circuit voltage (V$_{oc}$) has been determined to be the primary limiting factor. Even for the best solar cells, V$_{oc}$ remains much lower than it could be expected [87]. It is assumed that this behavior can be attributed to the occurrence of band gap fluctuations [88, 89]. Several factors have been stated to be responsible for these band gap fluctuations, such as the formation of $[2Cu_{Zn}^- + Sn_{Zn}^{2+}]$ defect pairs [90] or the inclusion of stannite, which has a lower band gap as kesterite [73, 91]. In a recent study by Scragg et al. [92], theoretical and experimental results were presented, showing that the fluctuations in the range of $100 - 200$ meV are primary caused by the disorder among the two cations Cu and Zn on the two Wyckoff positions $2c$ and $2d$. The effective band gap is significantly reduced, due to the high number of $[Cu_{Zn}^- + Zn_{Cu}^+]$ defects complexes. It was shown by *ab initio* calculations that these defect pairs are able to cluster in the structure [92]. It seems to be essential to control the disorder of Cu and Zn, in order to improve the performance of CZTS based solar cells.

Another major challenge that has to be overcome to further increase the material quality of CZTS, is the control of intrinsic defects and phase stability. The formation of certain secondary phases is detrimental for the photovoltaic performance, for example copper or tin sulfides as well as Cu-Sn ternary phases seem to be very harmful, due to their lower band gap [73]. Using a Cu-poor and Zn-rich composition, the formation of copper sulfide phases can be prevented. The highest efficiencies of CZTS based devices were obtained with absorber layers having such a composition [13]. However, the Zn-rich composition can cause the formation of ZnS secondary phase. The effect of ZnS on the solar cell performance is still not clear. Too much of this secondary phase is detrimental, as it affects the CZTS grain size and the carrier transportation behavior, whereas it was shown that ZnS at the space charge region can improve the open-circuit voltage due to the reduction of the heterojunction interface recombination rate [93].

Apart from the improvement of the absorber layer, it is also required to optimize the solar cell architecture in order to further increase device efficiencies, which will not be discussed here.

3. Methodology

3.1. Preparative methods

3.1.1. Mechanochemical synthesis

Mechanical alloying is a solid-state process and describes the treatment of powder samples in a high energy ball mill. The aim is the preparation of homogenous material, starting from mixed elemental or compound powders. The term mechanical alloying was introduced by Benjamin et al., who developed the process and provided a detailed description in several studies [94–96]. With this technique it is possible to synthesize a variety of different materials including equilibrium alloys, metastable crystalline, quasicrystalline, or amorphous phases, nanostructures, and even supersaturated solid solutions [97].

A number of different high-energy ball mills, which differ in capacity, efficiency, or maximal operation speed are available for mechanical alloying. Detailed reviews of these ball mill types are found in literature [97, 98].

A commonly used mill for sample processing and material development is the planetary ball mill [99]. Characteristic for this type of high energy ball mill is the planet-like movement of the grinding unit, which is arranged on a rotating support disc. The unit turns on its own axis whereas the support disc rotates in the opposite direction. These movements produce two opposing centrifugal forces that act alternately on the content of the grinding bowl, which consists of sample material and grinding balls. As a result, the grinding balls run down the inner wall of the bowl (friction effect) and after crossing the chamber at high speed they hit the opposite wall (impact effect). Additionally, the impact between grinding balls themselves further affect the ground sample material [97]. A schematic illustration of the milling operation is depicted in Figure 3.1.

Planetary ball mills are used for a wide range of applications in science and industry. One popular approach is their utilization for mechanochemical synthesis. In these mechanochemical processes the mechanical energy of the milling treatment is used to induce a chemical reaction in order to synthesize new compounds. Mechanochemistry finds a widespread use due to the possibility of rapid, highly efficient, and usually solvent-free chemical synthesis. Furthermore, it is feasible to synthesize compounds that cannot be obtained via a conventional solid-state routes.
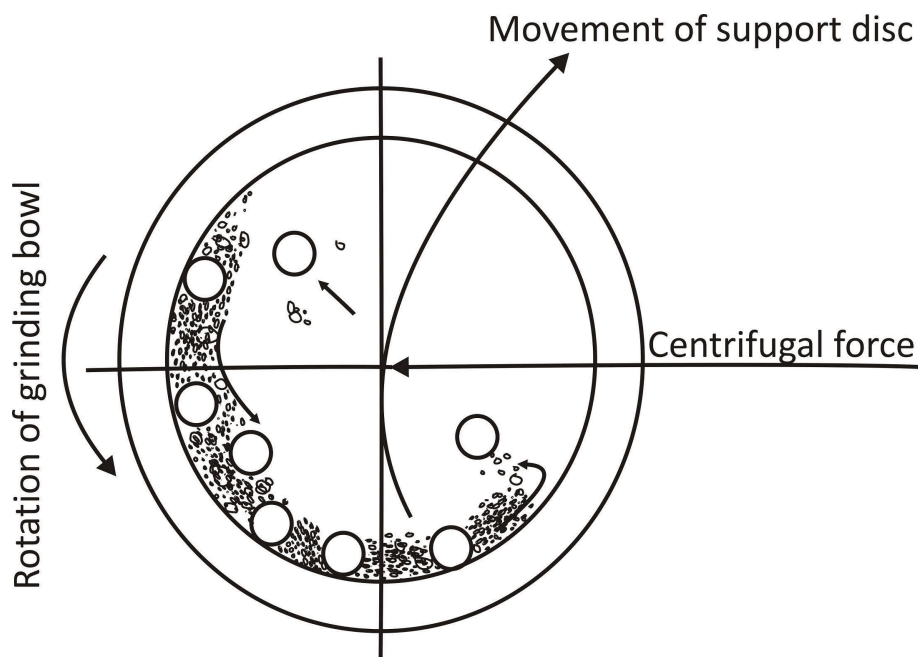
Figure 3.1.: Schematic illustration of the grinding ball motion inside a planetary ball mill (horizontal section) according to Ref.[97]

During mechanochemical synthesis the reaction kinetics of the chemical reaction is enhanced. Because of the constant movement of the powder in the planetary ball mill the area of contact between the reactants is increased. Additionally, particle size reduction during the milling process provides new surface regions to encounter repeatedly. In contrast to conventional solid-state reactions, where continuous growth of the product phase at the interfaces of the reactants is achieved by diffusion processes at elevated temperature, reaction milling do not require diffusion through already formed product layers. Consequently, it is possible to reduce the reaction temperatures significantly. Reactions that normally require high temperatures can be performed in the ball mill without using any external heat sources [97].

It must also be noted that the reduction of the reaction time and temperature as well as the possibility of solvent-free reactions materials and energy can be used more efficiently. Consequently, this leads to economic and environmental benefits.

Two different reaction types are known in mechanochemical processes [97, 99]. During a gradual transformation the product phase is formed gradually with milling time. Each ball collision in the planetary ball mill increases the total provided energy and, consequently, the yield of the desired compound. Another possibility is a mechanically induced self-sustaining reaction (MSR), where after a certain activation time, called ignition time (t_{ig}), the reaction rate starts to increase. This causes a sudden rise of temperature in the grinding

unit, followed by the ignition of a rapid exothermic reaction. This self-propagating process is only possible in highly exothermic powder mixtures.

Mechanochemical synthesis is a highly complex process and several variables influence the milling results. Hence, the determination of the ideal milling conditions for each individual system is very important. Following parameters have to be considered in order to achieve the desired product phase:

- Material and size of grinding container

- Type, size, and number of grinding balls

- Milling speed

- Milling time (reaction time)

- Milling atmosphere (air, nitrogen, argon)

- Filling ratio of sample material (ball to powder ratio)

In this study, a PULVERISETTE 6 classic line planetary ball mill, manufactured by Fritsch GmbH (Germany), was used. Milling experiments were carried out in an 80 ml agate grinding bowl, filled with 5 agate grinding balls of 20 mm diameter (See Figure 3.2). The grinding container was filled under Ar-atmosphere.

Figure 3.2.: Ball mill PULVERISETTE 6 and agate grinding bowl/balls

3.1.2. H₂S furnace

For crystallization of the CZTS material a conventional tube furnace from GERO GmbH (Germany), equipped with a SiO_2-tube (inner diameter 70 mm), was used (see Figure 3.3). During the reaction, the powder sample was placed in a corundum boat in the center of the furnace, and gaseous hydrogen sulfide (Air liquide 99.5 %) was flowing through the furnace over the sample. Reaction temperature and time was set using an external controller, temperature in the furnace was controlled by a Pt-Rh/Pt-thermocouple. Unreacted H_2S-gas was introduced into diluted sulfuric acid (H_2SO_4 20 %) and afterwards into a 15 % solution of sodium hydroxide. In this way, the harmful H_2S is converted into nontoxic Na_2SO_3, according to following reaction (Equation 3.1):

$$H_2S + H_2SO_4 \rightarrow SO_2 + S + 2\,H_2O \qquad (3.1)$$

$$SO_2 + NaOH \rightarrow NaHSO_3$$

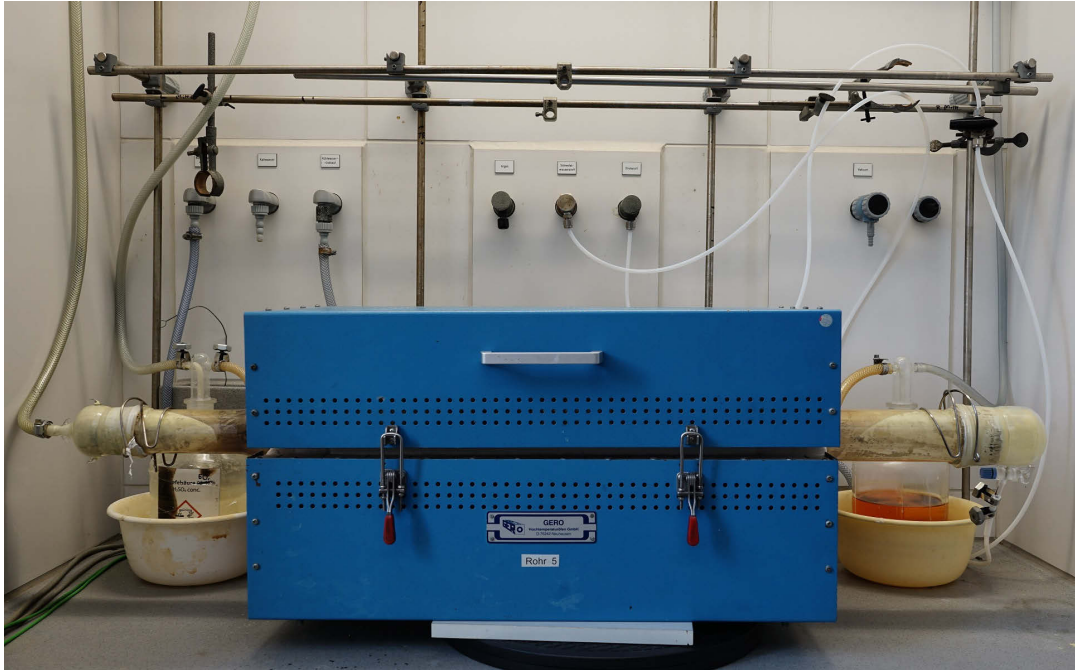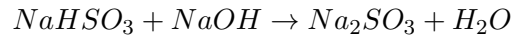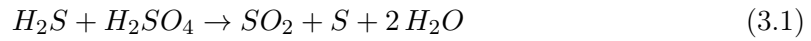$$NaHSO_3 + NaOH \rightarrow Na_2SO_3 + H_2O$$

Figure 3.3.: Tube furnace that was used for the crystallization of the as-milled CZTS powder with gaseous H_2S.

3.2. Diffraction methods

3.2.1. X-ray and neutron diffraction

Diffraction methods are among the most important analytical characterization techniques in solid state chemistry. They are employed for structure determination in crystalline materials, and can be used to identify structural properties such as lattice parameters, phase composition, epitaxy, preferred orientation, or grain size. The technique is based on the diffraction of X-rays or neutrons at the atoms of the crystal lattice. The crystal lattice consists of parallel planes with distance d thst are identified by Miller indices (h, k, l). Because of the interatomic distances in the order of magnitude of $\sim 10^{-10}$ m, especially X-rays and slow thermal neutrons are suitable for scattering experiments. The fundamental principle is based on the interaction between X-ray photons and the electron shell or the neutrons and the atomic nuclei, respectively. The theoretical principle of the diffraction phenomenon is described by Bragg's law (Equation 3.2):

$$n\lambda = 2d \cdot sin\theta \tag{3.2}$$

n - integer
λ - wavelength of incident beam (X-ray or neutron)
d - distance between atomic layers (hkl)
ϑ - diffraction angle

The equation describes the interaction of the incident beam with the sample and defines the general condition for constructive interference. It is assumed that the crystal consists of layers, on which the radiation is reflected, and constructive interference occurs when the path length difference is an integer number of the wavelength. The diffracted waves of different atomic layers cause a certain diffraction pattern, which contains information about the atomic arrangement in the crystalline material.

As mentioned above, X-rays are scattered at the electrons of the shell, whereas neutron scattering happens at the nucleus of the atom, resulting in specific advantages and disadvantages. Regarding X-rays, the scattering power of an atom is described by the atomic form factor f_i, which depends linearly on the number of electrons in the atom. Hence, it is easier to distinguish between elements with a large difference in electron number. Furthermore, the atomic form factor is a function of the wavelength and the diffraction angle, resulting in decreasing intensities with increasing angles.

On the other hand, the atomic nucleus can be regarded as a point compared to the electron shell, thus, in neutron scattering no atomic form factor is considered. The interaction of the neutron beam with the crystal is described by the scattering length, which is independent of the scattering angle. Furthermore, the scattering length of the nuclei does not

depend linearly on the atomic number. Instead, it varies for different isotopes and shows an irregular dependence on the atomic number. This opens both – the possibility of both measuring light elements, e.g. lithium, and the distinction between elements with similar atomic number, such as copper and zinc. However, due to the relatively weak scattering intensity of neutrons, large amount of sample and long measurement times are necessary in comparison to X-ray diffraction.

3.2.2. Instruments

Different instruments were used for diffraction measurements during the present study.

The X-ray diffraction measurements were carried out on a PANalytical X'Pert Pro diffractometer (PANalytical B.V, Almelo, Netherlands) in Bragg-Brentano geometry using a ϑ/ϑ arrangement. The X-ray radiation is generated by a copper X-ray tube. A nickel foil is used for filtering the Bremsstrahlung and the CuK_β-radiation. As the diffractometer is not equipped with a monochromator, both, the $CuK_{\alpha 1}$- ($\lambda = 154.056$ pm) and the $CuK_{\alpha 2}$-radiation ($\lambda = 154.438$ pm), with an intensity ratio of about 2:1, are hitting the sample. The signal detection was carried out via a PIXcel solid state detector.

For in situ high temperature X-ray diffraction measurements, a STOE STADI P diffractometer (STOE & CIE GmbH, Darmstadt) in Debye-Scherrer geometry was used. The instrument uses MoK_{a1}-radiation, the unwanted MoK_{a2}-radiation is filtered via a Ge(111)-single crystal monochromator. The diffractometer is equipped with a STOE IP-PSD image plate-detector and a STOE furnace using a Ni/CrNi thermocouple. For data collection the sample was encapsulated in an evacuated silica capillary.

Neutron diffraction measurements of kesterite samples were carried out at the Forschungs-Neutronenquelle Heinz Maier Leibnitz Zentrum (FRM II, Garching), using the high resolution powder diffractometer SPODI [100], as well as the Berlin Research Reactor BER II at the Helmholtz-Zentrum Berlin für Materialien und Energie (HZB, Berlin), using the fine resolution powder diffractometer FIREPOD E9 [101]. The former (SPODI) works in Debye-Scherrer geometry and is equipped with a Ge(551)-single crystal monochromator. In standard configuration, the thermal neutrons have a wavelength of $\lambda = 154.83$ pm. Detection is carried out by 80 position-sensitive ^{3}He detectors, placed in vertical direction. The compressed air driven detectors have an active height of 300 mm and cover an angular range of $2\vartheta = 160°$, which means, each detector covers $2\vartheta = 2°$. For the measurements the samples were encapsulated in a vanadium container with a wall thickness of 0.15 mm and an inner diameter of $9 - 10$ mm.

In the second neutron diffraction instrument (E9), a Ge(511)-single crystal monochromator is used, the wavelength is $\lambda = 179.8$ pm. The diffractometer is equipped with eight individual area ^{3}He detectors (300 x 300 mm) with additional oscillating radial collimators

for background reduction. The samples were encapsulated in vanadium containers of 6 mm inner diameter. Data were collected at ambient temperature.

3.2.3. Evaluation of diffraction data

A method for the evaluation of X-ray or neutron diffraction data is the Rietveld refinement [102, 103]. It is a mathematical approach for fitting a theoretical, already known crystal structure to the measured powder diffraction data. By adapting the structure model to the measured diffraction pattern, it is possible to determine changes of the unit cell parameters, such as lattice parameters, atomic position, or ordering of the atoms. The refinement according to Rietveld works with an algorithm that is based on the method of least squares. For each point of the diffraction pattern the theoretical intensity is calculated and compared to the observed one.

The quality of a Rietveld refinement is evaluated according to the agreement of the observed values y_i(obs) with the calculated values y_i(calc), and is given by residual values (R-values). The value R_{wp} (weighted R-value) indicates the mean deviation of the calculated data to the observed diffraction pattern and is minimized during the refinement.

$$R_{wp} = \sqrt{\frac{\sum w_i(y_i(obs) - y_i(calc))^2}{\Sigma w_i(y_i(obs))^2}} \tag{3.3}$$

w_i - weighting factor at point i

y_i (obs) - measured intensity at point i

y_i(calc) - calculated intensity at point i

Ideally this value is zero, which can never be achieved due to the signal to noise ratio, thus the R_{exp} value is calculated, indicating the best possible value and the accuracy of the measurement.

$$R_{exp} = \sqrt{\frac{N - P + C}{\Sigma w_i(y_i(obs))^2}} \tag{3.4}$$

N - Number of measured points

P - Number of parameters

C - Number of parameter linkings

In contrast, the value R_{Bragg} is calculated from the intensities of the n reflections that are present in the pattern.

$$R_{Bragg} = \sqrt{\frac{\sum | I_n(obs) - I_n(calc) |}{\Sigma I_n(obs)}} \tag{3.5}$$

I_n(obs) - measured integral intensity of the n reflection

I_n(calc) - calculated integral intensity of the n reflection

The goodness of fit S is formed by the ratio of the two former R-values R_{wp} and R_{exp}. In the ideal case S should approach a value of 1.

$$S = \frac{R_{wp}}{R_{exp}} \tag{3.6}$$

In this work the program package FULLPROF Suite [104] was used for the Rietveld analysis.

3.2.4. Determination of crystallite size

Using the Scherrer Equation [105] (Equation 3.7) the crystallite sizes can be calculated using the full width at half maximum (FWHM) of an individual reflections. These FWHM values were determined using the program STOE WinXPOW.

$$\triangle(2\theta) = \frac{K\lambda}{Lcos\theta_0} \tag{3.7}$$

$\Delta(2\theta)$ - line broadening at half the maximum intensity (FWHM),

K - Scherrer-form factor, (in this study $K = 1$)

λ - wavelength

L - mean size of crystallite

θ_0- diffraction angle.

$\Delta(2\theta)$ has to be corrected for reflex broadening coming from the instrument according to $\triangle(2\theta) = (\beta_M^2 - \beta_I^2)^{\frac{1}{2}}$ (β_M is the measured FWHM and β_I is the correction factor for instrument broadening).

3.3. Analytical methods

3.3.1. Electron microprobe analysis

Electron microprobe analysis is a powerful analytic tool for non-destructive chemical analysis of solid samples. It can be used for the identification of the phases that are present in a sample as well as the precise determination of the chemical composition of these phases. When high energy electrons are accelerated onto a specimen, atoms of the target material are excited and X-rays of a characteristic wavelength, depending on the analyzed elements, are emitted.

For imaging the surface of the sample back-scattered electron (BSE) are used, as it is possible to show differences in mean atomic number. Phases with distinct compositions are distinguishable because the image varies in brightness, depending on the average atomic

number of the phases. Heavy elements have a higher backscatter coefficient than light elements, thus, phases with a high average atomic number appear brighter.

For quantitative analysis wavelength dispersive spectroscopy (WDS) is applied. The X-ray photons that are excited by the incident focused electron beam are analyzed in a wavelength dispersive X-ray-spectrometer. It consists of an oriented single crystal that allows only X-rays of desired wavelength to enter detector. The wavelength is varied by changing the position of the analyzing crystal relative to the sample. Several crystals are used to cover a wide range of wavelengths and for simultaneous measurement of multiple elements. In order to get reliable results proper calibration is required, which can be done by pure elements or compounds with definite composition. Furthermore, the X-ray intensities have to be corrected for matrix effects, employing the ZAF correction method (Z – atomic number, A – absorption, and F – fluorescence).

In the current work, a JEOL JXA 8200 SuperProbe (JEOL Ltd., Japan) was used for electron microprobe measurements. The electron beam is generated by a LaB_6 electron source and the instrument is equipped with one energy dispersive (EDS) and five wavelength dispersive spectrometers (WDS). Elemental standards Cu, Zn, Sn as well as the mineral chalcopyrite for S were used for the calibration of the system.

3.3.2. X-ray absorption spectroscopy (XAS)

X-ray absorption spectroscopy (XAS) is a continuously evolving analytical technique which is used for structural analysis in a wide range of scientific areas. It is an element specific and local bonding sensitive method and it provides detailed information about the local crystal structure and the chemical environment of a selected element in a compound. It can be seen as a fingerprint of the analyzed sample [106].

The fundamental principle of the method is the X-ray photoelectric effect [106, 107]. In the X-ray absorption process the sample is irradiated with X-rays in a certain energy range in order to measure the energy dependence of the X-ray absorption coefficient $\mu(E)$. Generally, as the energy increases, the absorption coefficient smoothly decreases ($\sim 1/E^3$). At a specific energy, denoted as absorption edge (K, L, M-edge, depending on the observed absorption edge), a steep rise of the absorption is observed due to the excitation of an electron of the core level. This excitation energy is specific for the absorbing element [108]. Beyond the absorption edge at higher photon energy, the absorption does not decrease monotonically but exhibits characteristic oscillations, due to the scattering of the generated electron wave at the adjacent atoms. The outgoing photoelectron wave of the absorber atom interferes with the scattered electron waves depending on the geometry of the absorber surrounding and the wavelength of the photoelectron. These interference effects (constructive or destructive) influence the absorption probability, resulting in an
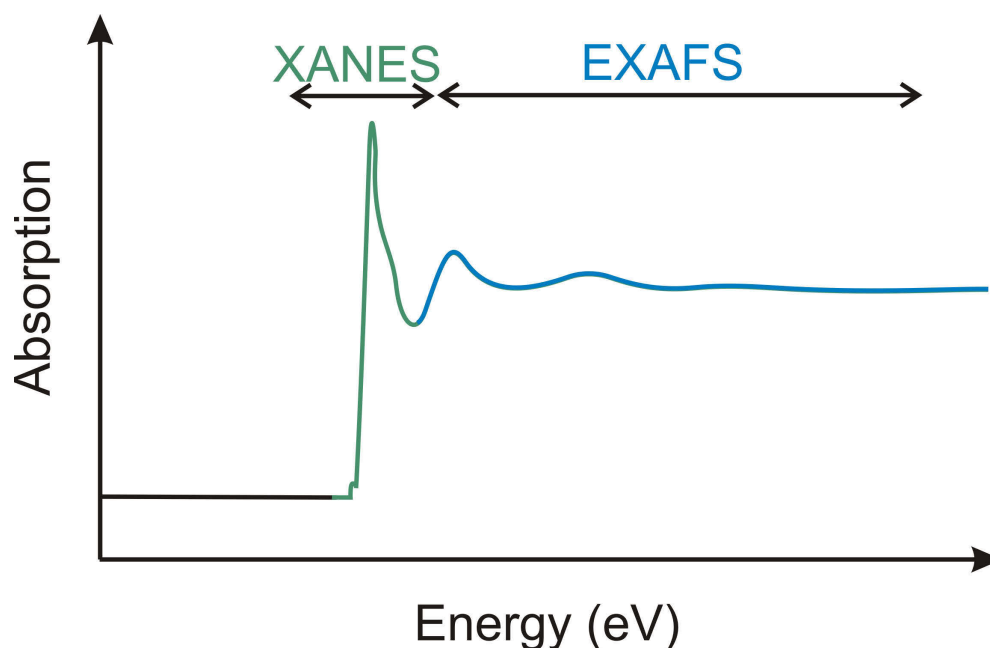
Figure 3.4.: Schematic illustration of a normalized X-ray absorption spectrum showing the XANES and the EXAFS regions

energy-dependent variation of the absorption coefficient and creating a fine structure of the absorption spectrum [109].

A schematic illustration of an X-ray absorption spectrum is depicted in Figure 3.4. It can be divided into two main regions, depending on the occurring scattering events of the photoelectrons. The extended X-ray absorption fine structure (EXAFS) can be subjected to single scattering whereas the X-ray absorption near edge structure (XANES) represents multiple scattering events.

The XANES region is normally located in a $30-50$ eV range around the absorption edge [106, 109]. The pre-edge region is related to the transitions of photoelectrons from the core level to an unoccupied bound state [109]. XANES is sensitive to chemical bonding and therefore provides information about the local electronic structure of the absorbing atom, such as the oxidation states and the coordination geometries. The multiple scattering effects depend on the three-dimensional geometry of the crystal structure; hence it is possible to distinguish between different phases of the sample [108].

The XANES part of the spectrum is followed by the EXAFS region at higher energy up to 1000 eV above the edge and it is independent of the chemical bonding. EXAFS contains geometrical information about the chemical environment of the absorber and it is possible to acquire knowledge about the distance, coordination number and species of the adjacent atoms [109].

For the collection of X-ray absorption data high energy X-rays with a continuous spectrum are required, therefore the use of synchrotron radiation is necessary. Interpretation of the absorption spectra can be performed with the help of reference spectra of known compounds. By using linear combination fitting, quantitative analysis of the phases, which are present in the sample, is possible.

In this work, X-ray absorption spectroscopy experiments were performed at the soft X-ray double crystal monochromator beamline KMC-1 at synchrotron light source Bessy II of the Helmholtz-Zentrum Berlin (HZB), Germany. The measurements were carried out in transmission mode at the sulfur K-edge (2472 eV) at a range of 70 eV below and 200 eV above the absorption edge. Analysis of the spectra including energy calibration, normalization, background subtraction, and fitting was using the software package IFEFFIT [110, 111].

Bibliography

[1]   Renewable Energy Policy Network for the 21st Century (REN21), *Renewables 2015 Global status report*, **2015**.

[2]   BP Global, *BP Statistical Review of World Energy June 2015*, **2015**.

[3]   United Nations, Department of Economic and Social Affairs (Population Division), *World Population 2015 Wallchart (World Population Prospects: The 2015 Revision)*, **2015**.

[4]   Bundesanstalt für Geowissenschaften und Rohstoffe (BGR), *Energiestudie 2015: Reserven,Ressourcen und Verfügbarkeit von Energierohstoffen*, **2015**.

[5]   U. S. Energy Information Administration (EIA), Office of Integrated and International Energy Analysis, *Annual Energy Outlook 2015 (AEO2015)*, **2015**.

[6]   International Energy Agency (IEA), *CO2 emission from fuel combustion (Highlights, 2015 Edition)*, **2015**.

[7]   International Atomic Energy Agency (IAEA), *Storage of spent nuclear fuel (Specific saftey guide No. SSG-15)*, **2012**.

[8]   K. Mertens, *Photovoltaik - Lehrbuch zu Grundlagen, Technologie und Praxis*, Hanser Verlag, **2013**.

[9]   Bundesministerium für Umwelt, Naturschutz und Reaktorsicherheit (BMU), *Erneuerbare Energien, Innovationen für eine nachhaltige Energiezukunft*, **2011**.

[10] National Renewable Energy Laboratory (NREL), *Best research-cell efficiencies*, **2016**.

[11] S. Chen, X. G. Gong, A. Walsh, S.-H. Wei, *Appl. Phys. Lett.* **2009**, *94*, 041903/1–041903/3.

[12] W. Wang, M. T. Winkler, O. Gunawan, T. Gokmen, T. K. Todorov, Y. Zhu, D. B. Mitzi, *Adv. Energy Mater.* **2014**, *4*, 1301465/1–1301465/5.

[13] B. Shin, O. Gunawan, Y. Zhu, N. A. Bojarczuk, S. J. Chey, S. Guha, *Prog. Photovoltaics* **2013**, *21*, 72–76.

[14] G. Brammertz, M. Buffiere, S. Oueslati, H. El Anzeery, K. Ben Messaoud, S. Sahayaraj, C. Koeble, M. Meuris, J. Poortmans, *Appl. Phys. Lett.* **2013**, *103*, 163904/1–163904/4.

[15]   I. D. Olekseyuk, I. V. Dudchak, L. V. Piskach, *J. Alloys Compd.* **2004**, *368*, 135–143.

[16]   G. H. Moh, *Chem. Erde* **1975**, *34*, 1–61.

[17]   D. M. Berg, M. Arasimowicz, R. Djemour, L. Gutay, S. Siebentritt, S. Schorr, X. Fontane, V. Izquierdo-Roca, A. Perez-Rodriguez, P. J. Dale, *Thin Solid Films* **2014**, *569*, 113–123.

[18]   B. Pamplin, *Prog. Cryst. Growth Charact.* **1980**, *3*, 179–92.

[19]   S. Schorr, *Thin Solid Films* **2007**, *515*, 5985–5991.

[20]   S. R. Hall, J. T. Szymanski, J. M. Stewart, *Can. Mineral.* **1978**, *16*, 131–137.

[21]   J. Paier, R. Asahi, A. Nagoya, G. Kresse, *Phys. Rev. B: Condens. Matter Mater. Phys.* **2009**, *79*, 115126/1–115126/8.

[22]   C. Persson, *J. Appl. Phys.* **2010**, *107*, 053710/1–053710/8.

[23]   S. Schorr, *Sol. Energy Mater. Sol. Cells* **2011**, *95*, 1482–1488.

[24]   L. Choubrac, M. Paris, A. Lafond, C. Guillot-Deudon, X. Rocquefelte, S. Jobic, *Phys. Chem. Chem. Phys.* **2013**, *15*, 10722–10725.

[25]   S. Schorr, H.-J. Hoebler, M. Tovar, *Eur. J. Mineral.* **2007**, *19*, 65–73.

[26]   S. Schorr, M. Tovar, *BENSC Experimental Report* **2006**.

[27]   S. Chen, J.-H. Yang, X. G. Gong, A. Walsh, S.-H. Wei, *Phys. Rev. B: Condens. Matter Mater. Phys.* **2010**, *81*, 245204/1–245204/10.

[28]   A. Nagoya, R. Asahi, R. Wahl, G. Kresse, *Phys. Rev. B Condens. Matter Mater. Phys.* **2010**, *81*, 113202/1–113202/4.

[29]   J. J. S. Scragg, L. Choubrac, A. Lafond, T. Ericson, C. Platzer-Bjoerkman, *Appl. Phys. Lett.* **2014**, *104*, 041911/1–041911/4.

[30]   S. Schorr, G. Gonzalez-Aviles, *Phys. Status Solidi A* **2009**, *206*, 1054–1058.

[31]   L. E. Valle Rios, K. Neldner, G. Gurieva, S. Schorr, *J. Alloys Compd.* **2016**, *657*, 408–413.

[32]   G. Gurieva, M. Dimitrievska, S. Zander, A. Perez-Rodriguez, V. Izquierdo-Roca, S. Schorr, *Phys. Status Solidi C* **2015**, *12*, 588–591.

[33]   A. Lafond, L. Choubrac, C. Guillot-Deudon, P. Deniard, S. Jobic, *Z. Anorg. Allg. Chem.* **2012**, *638*, 2571–2577.

[34]   L. Choubrac, A. Lafond, C. Guillot-Deudon, Y. Moelo, S. Jobic, *Inorg. Chem.* **2012**, *51*, 3346–3348.

[35]   S. Chen, A. Walsh, X.-G. Gong, S.-H. Wei, *Adv. Mater.* **2013**, *25*, 1522–1539.

[36] S. Chen, X. G. Gong, A. Walsh, S.-H. Wei, *Appl. Phys. Lett.* **2010**, *96*, 021902/1–021902/3.

[37] S. Chen, L.-W. Wang, A. Walsh, X. G. Gong, S.-H. Wei, *Appl. Phys. Lett.* **2012**, *101*, 223901/1–223901/4.

[38] A. Walsh, S. Chen, S.-H. Wei, X.-G. Gong, *Adv. Energy Mater.* **2012**, *2*, 400–409.

[39] J. J. S. Scragg, Annealing of CZTS, Kestcells 18 month workshop, **2014**.

[40] G. H. Moh, *Neues Jahrb. Mineral. Abh.* **1960**, *94*, 1125–1146.

[41] A. H. Clark, R. H. Sillitoe, *Amer. Mineral.* **1970**, *55*, 1021–1025.

[42] J. R. Craig, G. Kullerud, *Carnegie Inst. Wash. Yearb.* **1969**, *67*, 177–179.

[43] L. I. Trishchuk, G. S. Oleinik, I. B. Misetskaya, *Thermochim. Acta* **1985**, *92*, 611–613.

[44] L. V. Piskach, O. V. Parasyuk, I. D. Olekseyuk, *J. Alloys Compd.* **1998**, *279*, 142–152.

[45] G. H. Moh, *Year Book - Carnegie Inst. Washington* **1963**, 199–200.

[46] N. Wang, *Neues Jahrb. Mineral. Monatsh.* **1974**, *9*, 424–31.

[47] M. Khanafer, J. Rivet, J. Flahaut, *Bull. Soc. Chim. Fr.* **1974**, 2670–2676.

[48] D. Wu, C. R. Knowles, L. L. Y. Chang, *Mineral. Mag.* **1986**, *50*, 323–325.

[49] S. Fiechter, M. Martinez, G. Schmidt, W. Henrion, Y. Tomm, *J. Phys. Chem. Solids* **2003**, *64*, 1859–1862.

[50] N. Wang, *Spec. Publ. Soc. Geol. Appl. Miner. Deposits* **1982**, *2*, 726–734.

[51] S. Jaulmes, J. Rivet, P. Laruelle, *Acta Crystallogr. Sect. B* **1977**, *B33*, 540–542.

[52] X.-A. Chen, H. Wada, A. Sato, M. Mieno, *J. Solid State Chem.* **1998**, *139*, 144–151.

[53] M. Onoda, X. a Chen, A. Sato, H. Wada, *Mater. Res. Bull.* **2000**, *35*, 1563–1570.

[54] P. A. Fernandes, P. M. P. Salome, A. F. da Cunha, *J. Phys. D: Appl. Phys.* **2010**, *43*, 215403/1–215403/11.

[55] G. H. Moh, *Neues Jahrb. Mineral. Abh.* **1982**, *144*, 291–342.

[56] V. A. Kovalenker, T. L. Evstigneeva, N. V. Troneva, *International Geology Review* **1979**, *23*, 365–370.

[57] X. Chen, X. Wang, C. An, J. Liu, Y. Qian, *J. Cryst. Growth* **2003**, *256*, 368–376.

[58] H. Hu, Z. Liu, B. Yang, X. Chen, Y. Qian, *J. Cryst. Growth* **2005**, *284*, 226–234.

[59] M. Bouaziz, J. Ouerfelli, M. Amlouk, S. Belgacem, *Phys. Status Solidi A* **2007**, *204*, 3354–3360.

[60] V. M. Dzhagan, A. P. Litvinchuk, M. Kruszynska, J. Kolny-Olesiak, M. Y. Valakh, D. R. T. Zahn, *J. Phys. Chem. C* **2014**, *118*, 27554–27558.

[61] N. Wang, *Neues Jahrb. Mineral. Monatsh.* **1981**, 337–343.

[62] X. a Chen, H. Wada, A. Sato, *Mater. Res. Bull.* **1999**, *34*, 239–247.

[63] D. J. Chakrabarti, D. E. Laughlin, *Bull. Alloy Phase Diagrams* **1983**, *4*, 254–271.

[64] R. C. Sharma, Y. A. Chang, *J. Phase Equilib.* **1996**, *17*, 261–266.

[65] C. Frondel, C. Palache, *Science* **1948**, *107*, 602.

[66] I. T. Steinberger, S. Mardix in, W. A. Benjamin, Inc., pp. 167–78.

[67] D. C. Buck, L. W. Strock, *Am. Mineral.* **1956**, *40*, 192–200.

[68] G. A. Samara, H. G. Drickamer, *Phys. Chem. Solids* **1962**, *23*, 457–461.

[69] R. C. Sharma, Y. A. Chang, *Bull. Alloy Phase Diagrams* **1986**, *7*, 269–273.

[70] G. H. Moh, *Neues Jahrb. Mineral. Abh.* **1969**, *111*, 227–263.

[71] P. Bonazzi, L. Bindi, G. P. Bernardini, S. Menchetti, *Can. Mineral.* **2003**, *41*, 639–647.

[72] H. Wiedemeier, F. J. Csillag, *Z. Kristallogr.* **1979**, *149*, 17–29.

[73] S. Siebentritt, S. Schorr, *Prog. Photovoltaics* **2012**, *20*, 512–519.

[74] M. Altosaar, J. Raudoja, K. Timmo, M. Danilson, M. Grossberg, J. Krustok, E. Mellikov, *Phys. Status Solidi A* **2008**, *205*, 167–170.

[75] H. Yoo, J. Kim, *Thin Solid Films* **2010**, *518*, 6567–6572.

[76] P. A. Fernandes, P. M. P. Salome, A. F. da Cunha, *Thin Solid Films* **2009**, *517*, 2519–2523.

[77] P. A. Fernandes, P. M. P. Salome, A. F. da Cunha, *Phys. Status Solidi C* **2010**, *7*, 901–904.

[78] K. Ito, T. Nakazawa, *Jpn. J. Appl. Phys. Part 1* **1988**, *27*, 2094–2097.

[79] J. J. Scragg, P. J. Dale, L. M. Peter, G. Zoppi, I. Forbes, *Phys. Status Solidi B* **2008**, *245*, 1772–1778.

[80] Zentrum fuer Sonnenenergie- und Wasserstoff-Forschung Baden -Wuerttemberg, *ZSW Sets New World Record for Thin-film Solar Cells*, *Vol. 2016*, **2016**, Press release 9/2016.

[81] H. Katagiri, N. Sasaguchi, S. Hando, S. Hoshino, J. Ohashi, T. Yokota, *Sol. Energy Mater. Sol. Cells* **1997**, *49*, 407–414.

[82] H. Katagiri, K. Jimbo, S. Yamada, T. Kamimura, W. S. Maw, T. Fukano, T. Ito, T. Motohiro, *Appl. Phys. Express* **2008**, *1*, 041201/1–041201/2.

[83] Y. Zhang, T. Yoshihara, A. Yamada, *Appl. Phys. Express* **2012**, *5*, 012301/1–012301/3.

[84] K. Moriya, K. Tanaka, H. Uchiki, *Jpn. J. Appl. Phys.* **2008**, *47*, 602–604.

[85] H. Yoo, J. Kim, *Sol. Energy Mater. Sol. Cells* **2010**, *95*, 239–244.

[86] J. J. Scragg, P. J. Dale, L. M. Peter, *Electrochem. Commun.* **2008**, *10*, 639–642.

[87] D. B. Mitzi, O. Gunawan, T. K. Todorov, K.-J. Wang, S. Guha, *Sol. Energy Mater. Sol. Cells* **2011**, *95*, 1421–1436.

[88] T. Gokmen, O. Gunawan, T. K. Todorov, D. B. Mitzi, *Appl. Phys. Lett.* **2013**, *103*, 103506/1–103506/5.

[89] T. Gokmen, O. Gunawan, D. B. Mitzi, *Appl. Phys. Lett.* **2014**, *105*, 033903/1–033903/5.

[90] M. Grossberg, T. Raadik, J. Raudoja, J. Krustok, *Current Applied Physics* **2014**, *14*, 447–450.

[91] R. Djemour, A. Redinger, M. Mousel, L. Gutay, S. Siebentritt, *J. Appl. Phys. (Melville NY U. S.)* **2014**, *116*, 073509/1–073509/9.

[92] J. J. S. Scragg, J. K. Larsen, M. Kumar, C. Persson, J. Sendler, S. Siebentritt, C. Platzer Bjoerkman, *Phys. Status Solidi B* **2016**, *253*, 189–196.

[93] W. Li, J. Chen, C. Yan, X. Hao, *J. Alloys Compd.* **2015**, *632*, 178–184.

[94] J. S. Benjamin, T. E. Volin, *Met. Trans.* **1974**, *5*, 1929–1934.

[95] J. S. Benjamin, *Sci. Am.* **1976**, *234*, 40–48.

[96] P. S. Gilman, J. S. Benjamin, *Annu. Rev. Mater. Sci.* **1983**, *13*, 279–300.

[97] C. Suryanarayana, *Prog. Mater. Sci.* **2000**, *46*, 1–184.

[98] A. C. Suryanarayana, *in: Powder Metal Technologies and Applications*, *Vol. 7*, (Ed.: ASM International Handbook Committee), ASM Handbook, **1998**, pp. 80–90.

[99] C. F. Burmeister, A. Kwade, *Chem. Soc. Rev.* **2013**, *42*, 7660–7667.

[100] M. Hoelzel, A. Senyshyn, N. Juenke, H. Boysen, W. Schmahl, H. Fuess, *Nucl. Instrum. Methods Phys. Res. Sect. A* **2012**, *667*, 32–37.

[101] D. M. Tobbens, N. Stusser, K. Knorr, H. M. Mayer, G. Lampert, *Mater. Sci. Forum* **2001**, *378-381*, 288–293.

[102] H. M. Rietveld, *J. Appl. Crystallogr.* **1969**, *2*, 65–71.

[103] H. M. Rietveld, *Phys. Scr.* **2014**, *89*, 098002/1–098002/6.

[104] J. Rodriguez-Carvajal, *Abstracts of the Satellite Meeting on Powder Diffraction of the XV.Congress of the IUCr* **1990**, 127.

[105] P. Scherrer, *Nachrichten von der Gesellschaft der Wissenschaften zu Goettingen Mathematisch-Physikalische Klasse* **1918**, *1918*.

[106] D. C. Koningsberger, R. Prins, *X-ray Absorption: Principles, Applications, Techniques of EXAFS SEXAFS, and XANES*, John Wiley & Sons, **1988**, 673 pp.

[107] D. C. Koningsberger, R. Prins, Editors, *Chemical Analysis, Vol. 91: X-ray Absorption: Principles, Applications, Techniques of EXAFS SEXAFS, and XANES*, John Wiley & Sons, **1988**, 673 pp.

[108] G. Bunker, *Introduction to XAFS*, Cambridge University Press, Cambridge, **2010**.

[109] M. C. Schnohr, Claudia S. ; Ridgway, *X-Ray absorption spectroscopy of semiconductors*, Springer-Verlag Berlin Heidelberg, **2015**.

[110] M. Newville, *J. Synchrotron Radiat.* **2001**, *8*, 322–324.

[111] B. Ravel, M. Newville, *J. Synchrotron Radiat.* **2005**, *12*, 537–541.

Part II.

Results and Discussion

4. Publication 1

A mechanochemical route to single phase Cu_2ZnSnS_4 powder

Anna Ritscher, Justus Just, Oleksandr Dolotko, Susan Schorr, Martin Lerch

Contribution to publication:

A. Ritscher: Sample preparation, analysis and evaluation, writing.

J. Just: Measurements (XANES), evaluation.

O. Dolotko: Measurements (neutron diffraction).

S. Schorr: General discussion, proofreading.

M. Lerch: General advice and helpful comments, proofreading

Overall contribution of A. Ritscher to the publication: 80 %

Authors   A. Ritscher [1,2], J. Just [2,3], O. Dolotko [4], S. Schorr [2, 5], M. Lerch *[1]

[1] Institut für Chemie, Technische Universität Berlin, Straße des 17.Juni 115, 10623 Berlin, Germany

[2] Helmholtz-Zentrum Berlin für Materialien und Energie, Hahn-Meitner-Platz 1, 14109 Berlin, Germany

[3] Fachbereich C- Physik, Bergische Universität Wuppertal, Gaußstr. 20, 42119 Wuppertal, Germany

[4] Heinz Maier-Leibnitz Zentrum (MLZ), Technische Universität München, Lichtenbergstr.1, 85748 Garching, Germany

[5] Institut für Geologische Wissenschaften, Freie Universität Berlin, Malteserstr. 74, 12249 Berlin, Germany

* corresponding author

4.1. Abstract

With respect to absorber materials in solar cells, Cu_2ZnSnS_4 (CZTS) has been a focus of interest in recent years. In this work, a new route leading to single phase CZTS powders is presented. For structural characterization X-ray and neutron powder diffraction measurements were performed. Further structural and compositional analysis of the CZTS powder was carried out by means of X-ray absorption near edge spectroscopy (XANES) and wavelength-dispersive X-ray spectroscopy (WDS). The obtained CZTS powder with an actual composition of $Cu_{2.00(4)}Zn_{1.02(2)}Sn_{0.99(2)}S_{4.00(8)}$ adopts the kesterite-type structure. A detailed cation distribution analysis using the average neutron scattering length method revealed a partial disorder of copper and zinc on the $(2c)$ and $(2d)$ sites.

4.2. Introduction

As it consists merely of earth-abundant, non-toxic, and low-cost elements, it would be a suitable alternative to other chalcogenide-based absorber materials such as CdTe or CIGS ($CuInxGa_{(1-x)}Se_2$) that are currently used in thin films. It is a direct band gap p-type semiconductor with an optical band gap energy value of $1.5\,eV$ and has a large absorption coefficient in the order of $10^{-4}\,cm^{-1}$ [1-3]. Up to now record efficiencies of CZTS-based thin films reached values up to $8.4\,\%$ [4]. Yet, compared to the currently used chalcopyrite materials, efficiencies are significantly lower.

In order to enhance the quality and the efficiency of CZTS thin film photovoltaics it is necessary to gain a deeper insight into the absorber material. Systematic analysis of the semiconductor compound and its structural, chemical, and physical properties has been in the focus of interest in the last few years [5-10]. Due to the formation of secondary phases it is challenging to prepare phase-pure CZTS powder, which is important for detailed experiments concerning the correlations between structural and electronic properties. Consequently, the main motivation of the here-presented research is the development of a new chemical route for the synthesis of phase-pure stoichiometric kesterite powder and its structural characterization.

CZTS is a quaternary semiconductor belonging to the I_2-II-IV-VI$_4$ compound family. It adopts a tetragonal structure that can be derived from the zinc blende type by doubling the c-axis of the cubic sphalerite unit cell and by substituting the cations. A substitution scheme from binary ZnS to ternary Cu_2ZnSnS_4 is shown in Figure 4.1.

The correct crystal structure of CZTS has been a controversial issue. Two main structure types are described for quaternary $A^I_2B^{II}C^{IV}X^{VI}_4$ compounds, stannite (see Figure 4.2 a)
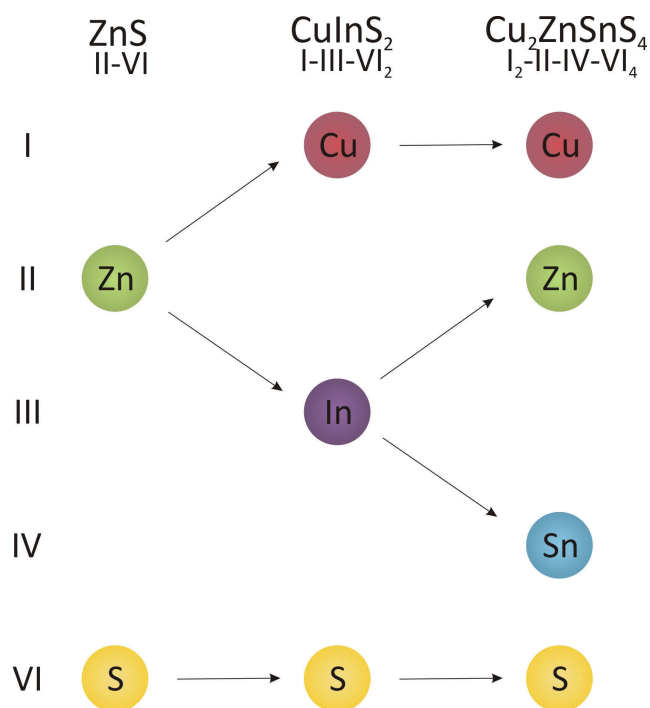
Figure 4.1.: Cross-substitution steps from binary II-VI compound (ZnS) via ternary I-II-VI$_2$ (CuInS$_2$) to quaternary I$_2$-II-IV-VI$_4$ (Cu$_2$ZnSnS$_4$).

and kesterite (see Figure 4.2 b) [11]. In these types the sulfur atoms form a ccp array where half of the tetrahedral voids are occupied by the cation species. The structures are closely connected but differ in the distribution of Cu+, Zn^{2+}, and Sn^{4+}. First reports on the crystal structure of natural specimen suggested the kesterite-type structure, space group $I\bar{4}$ (No. 82) [11], with a complete ordering of Cu$^+$ and Zn^{2+}. Cu fully occupies the Wyckoff position $2a$ $(0, 0, 0)$ whereas remaining Cu and Zn occupy the positions $2c$ $(0, 1/2, 1/4)$ and $2d$ $(0, 1/2, 3/4)$, respectively. Thus, the structure can be described by stacking cation layers Cu/Sn Cu/Zn Sn/Cu Cu/Zn Cu/Sn along the c-axis. Recently, several groups could confirm that Cu$_2$ZnSnS$_4$ adopts the kesterite-type structure [5, 12, 13].

Using conventional X-ray diffraction methods, Cu$^+$ and Zn^{2+} are not distinguishable due to their isoelectronic characteristic. As there is a significant difference in the neutron scattering length ($b_{Cu} = 7.718(4)$ fm, $b_{Zn} = 5.680(5)$ fm), neutron diffraction is the method of choice. Neutron diffraction studies of Cu$_2$ZnSnS$_4$ powder samples confirm the kesterite-type structure, yet report a partial [14] or complete disorder [5] of Cu and Zn on the $2c$ and $2d$ positions. Kesterite-type phases exhibiting a statistical distribution of Cu/Zn can be described in space group $I\bar{4}2m$ (No. 121) with Zn and Cu occupying the $4d$ Wyckoff position $(1/2, 0, 1/4)$ which is called disordered kesterite [15] (see Figure 4.2 c).
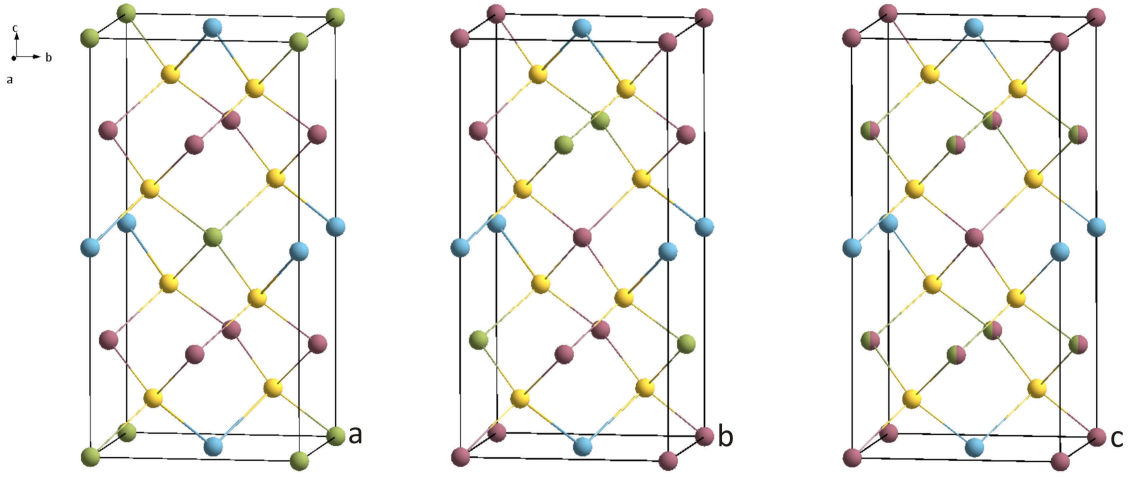
Figure 4.2.: Unit cells of the (a) stannite, (b) kesterite, and (c) disordered kesterite structure; Cu (red) Zn (green) Sn (blue) S (yellow)

It was also suggested by *ab initio* calculations [16, 17] that point defects Cu_{Zn} and Zn_{Cu} have very low formation energies, which underlines the possibility for Cu/Zn disorder. Recent studies on CZTS thin films determined the critical temperature for the transition from ordered to disordered kesterite to be at $260 \pm 10\,°C$ [18], which is also visible by a kink in the temperature dependent lattice parameter variation [6].

As four elements are present in the material, the formation of secondary phases such as CuS, Cu_2S, ZnS, SnS, SnS_2, and Cu_2SnS_3 seems probable. According to theoretical and experimental work [1, 19] the homogeneity region of the CZTS phase in the ternary phase diagram is rather small. Due to its small enthalpy of formation ZnS is likely to form and has been found to have a detrimental influence on solar cell performance [7, 8, 20]. Identification and quantification of the secondary phases ZnS and Cu_2SnS_3 by X-ray and neutron diffraction is difficult because of diffraction pattern overlap. As reported in [7] it is possible to identify the most important secondary phases with X-ray absorption spectroscopy (XAS).

In this study we investigate chemical composition and structural properties of a stoichiometric CZTS powder synthesized by a newly developed mechanochemical process. Phase purity and composition was determined by WDS and XANES. X-ray and neutron diffraction measurements were used to identify the crystal structure with a closer look to the cation distribution of the powder sample. Two refinement strategies will be discussed.

4.3. Experimental

4.3.1. Synthesis

The quaternary sulfide with the general formula Cu_2ZnSnS_4 was prepared by mechanical milling in a Fritsch Planetary Mono Mill PULVERISETTE 6 starting from the corresponding binary sulfides CuS, ZnS, and SnS followed by an annealing step.

Starting chemicals were prepared either by precipitation (CuS), sulfidation of the oxide (ZnS) or solid state reaction of the elements (SnS). Copper monosulfide (CuS) was precipitated from a 0.1 M $Cu(NO_3)_2$-solution (Merck, 99.5 %) with H_2S (Air Liquide, 99.5 %) and annealed at 230 °C in H_2S atmosphere for 2 h in a tube furnace. For the preparation of zinc sulfide (ZnS) reaction of the oxide ZnO (Merck, 99.5 %) in a tube furnace with H_2S-gas at 650 °C for 3 h was performed. Tin monosulfide (SnS) was synthesized by a solid state reaction of the elements Sn (Merck, 99.9 %) and S (Fluka, 99.99 %) in an evacuated and sealed silica ampoule in a muffle furnace. Stoichiometric amounts of tin and sulfur were loaded in a silica ampoule. Due to the significant vapor pressure of sulfur the sealed and evacuated tube was first heated to 300 °C to avoid explosion. The temperature was increased to 800 °C with a rate of 15 °C/h and the sample was annealed for 30 h. According to [21] the compound was sublimed three times in the ampoule (750 °C → 550 °C) to ensure complete reaction. Identification of the binary compounds was done by powder X-ray diffraction.

For the synthesis of the quaternary sulfide the binary sulfides CuS, ZnS, and SnS were mixed in an atomic ratio of 2:1:1 without any additional fluid medium and filled into an agate jar under Ar atmosphere in a glove box. A grinding bowl of 80 ml capacity is filled with 5 grinding balls with a diameter of 20 mm. Milling was performed in a high energy planetary ball mill using a rotational speed of 400 rpm and a milling time of 3 h with additional pauses of 30 min every hour to prevent the jar of heating up. The result of the mechanochemical treatment is a poorly crystalline product.

In order to get a well-crystalline product the sample was annealed in a conventional tube furnace equipped with a SiO_2-tube with an inner diameter of 70 mm in H_2S-atmosphere. The as-milled powder was placed in a small alumina boat inside the tube and heated under flowing reaction gas for 3 h at 500 °C. After reaction the sample was cooled down with a cooling rate of 60 K/h.

4.3.2. Characterization

The product was characterized both by X-ray and neutron powder diffraction. A Panalytical X'Pert PRO diffractometer (Bragg-Brentano geometry, Cu-K_a radiation) was used for powder XRD measurements. Neutron powder diffraction data were collected at the Forschungs-Neutronenquelle Heinz-Maier-Leibnitz Zentrum (MLZ, Garching) using the

high resolution powder diffractometer SPODI (Ge (551) $\lambda = 154.831$ pm) [22]. For neutron experiments the sample was encapsulated in a vanadium container with 0.15 mm wall thickness and 9 mm inner diameter (Ar atmosphere). Structural refinements were performed by the Rietveld method [23] using the program FULLPROF Suite Version 2015 [24] by applying a pseudo-Voigt [24] for the X-ray data and a Thompson-Cox-Hastings pseudo-Voigt function [25] for the neutron data, respectively.

Investigations of the chemical composition were performed by electron microprobe analysis (EMPA) with a JEOL JXA 8200 SuperProbe equipped with 5 wavelength dispersive X-ray spectrometers (WDS) and an energy dispersive X-ray spectrometer (EDS). X-ray absorption near edge structure measurements (XANES) at the sulfur K-edge (2472 eV) were carried out at the soft X-ray double crystal monochromator beamline KMC-1 at Bessy II (HZB) in transmission mode. The spectra were recorded with a pre-edge range of 70 eV and a range of 200 eV above the edge. Analysis of the spectra including energy calibration, background subtraction, normalization and fitting was performed with the IFEFFIT software package [26, 27].

In addition, possible contamination with nitrogen and oxygen were determined by a hot gas extraction with a LECO TC-300/EF-300 N/O analyzer. ZrO_2 and steel were used for calibration of the system (accuracy of N/O contents $\sim 2\%$).

4.4. Results

4.4.1. Mechanochemical synthesis and annealing

Attempts to prepare single-phase CZTS have been met with varying levels of success. Up to this time, bulk material of the quaternary sulfide has been usually synthesized by solid state reactions of the pure elements in evacuated and sealed silica ampoules [5] according to the standard technique described in [28]. Due to the high sulfur vapor pressure it is necessary to apply a defined temperature program and homogenization is obtained by a second annealing step at 750 °C. All these factors result in a long reaction time and an enhanced possibility of the formation of secondary phases.

As mentioned in the introduction, the main motivation of our work is to develop a new chemical route for an easier and faster synthesis of phase-pure CZTS powder. The main idea is to create a formation process where the annealing temperature of 750 °C is decreased in order to avoid thermal segregation and the formation of secondary phases. This can be realized by a mechanochemical approach and the synthesis of a precursor where the elements are already mixed at an atomic level. The first synthesis step is the reaction of the corresponding binary sulfides CuS, ZnS, and SnS in a high energy planetary ball mill as described in the experimental section.
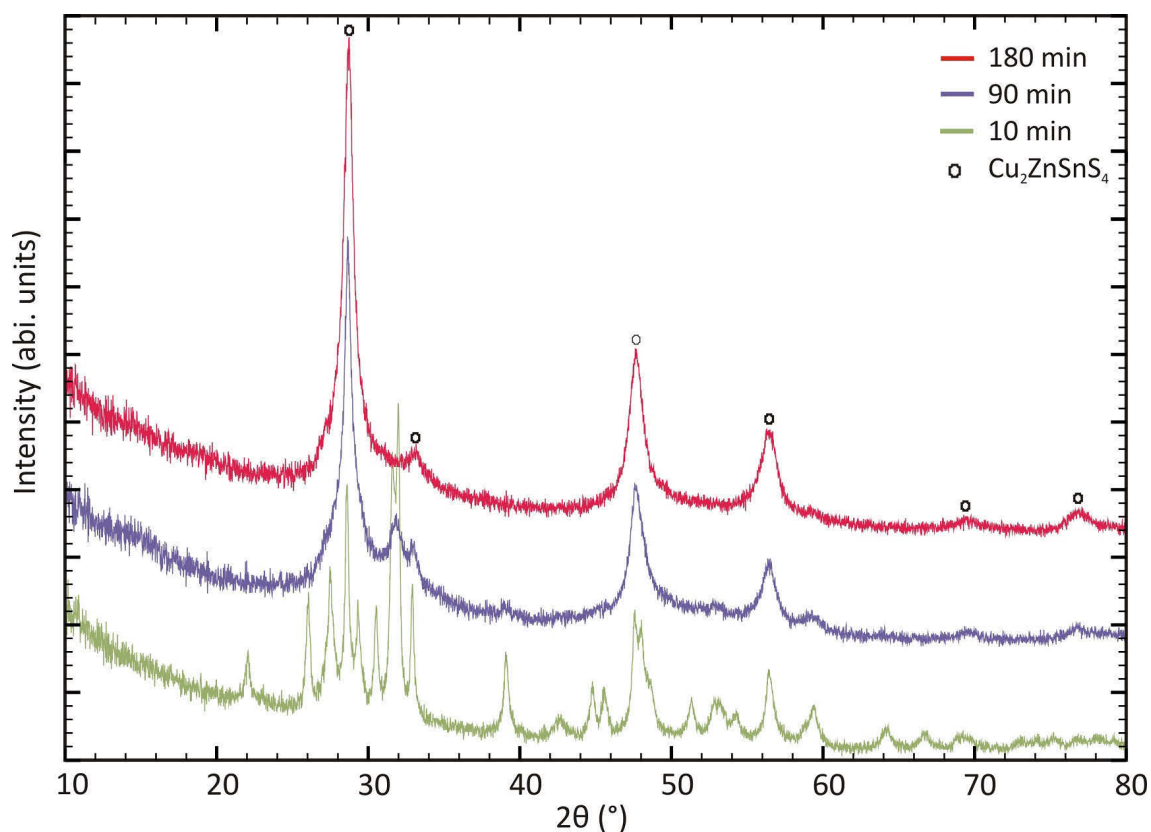
Figure 4.3.: Diffraction patterns of samples milled for 10, 90, and 180 minutes, respectively.

Additionally, a time experiment following the reaction during the milling process was performed within a time range of 10 min to 180 min. During the milling process a small amount of powder was withdrawn at time intervals of $10-30$ min from the grinding bowl. Selected diffraction patterns are depicted in Figure 4.3: after 10 minutes of milling the reflections of the binary sulfides are still present in the sample. After 3 hours of milling the reflections of the binary phases have vanished. Afterwards, the diffraction pattern did not change significantly, thus at this stage the powder was further processed.

In a second step the precursor powder is annealed in a tube furnace in H_2S atmosphere at 500 °C. This crystallization temperature is comparable to the temperature of actual thin film growth experiments which are often around 550 °C [29, 30]. The result of this annealing step is a product with good crystallinity. In Figure 4.4 the diffraction pattern of the as-milled sample as well as the crystalline sample after the annealing step is depicted. The crystal structure of the annealed sample was refined with the Rietveld method (for details see below). It should be mentioned that the milling step is essential for the synthesis of the above described quaternary sulfide. Annealing of the binary sulfides without a preceding milling process leads to the formation of secondary phases such as ZnS and SnS.
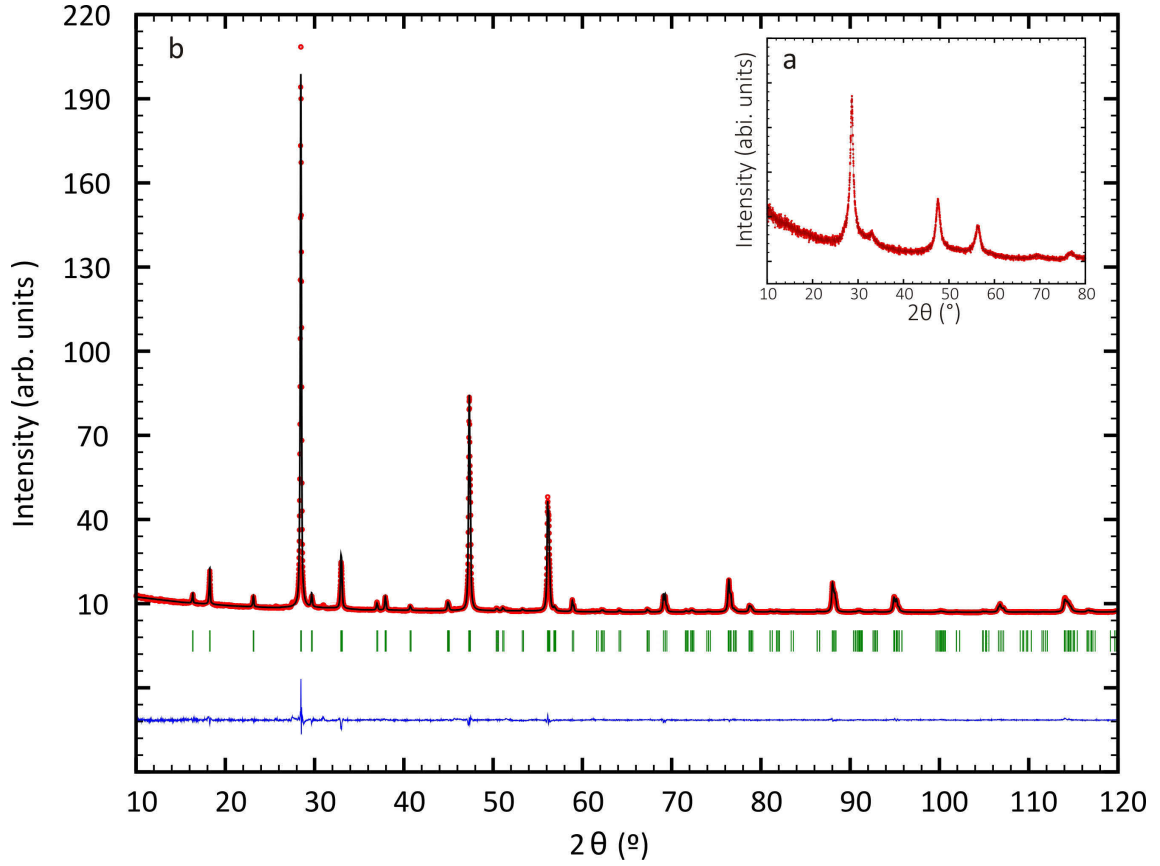
Figure 4.4.: X-ray diffraction pattern of the as-milled (a) and annealed (b) CZTS sample together with the results of the Rietveld refinement (kesterite-type structure).

4.4.2. Chemical composition and phase purity

In order to determine the exact chemical composition of the synthesized sample, the powder was analyzed by WDS. A calibration of the microprobe system was done by using elemental standards in order to achieve reliable compositional parameters. High accuracy of the chemical composition could be obtained by measuring 50 grains of the CZTS phase averaging over 30 point measurements within each grain. The results of the phase analysis showed a homogenous composition, no secondary phases were found. The Cu/(Zn+Sn) and Zn/Sn ratio of the single phase CZTS sample were determined as 1.00 and 1.03, respectively, thus by taking into account the measurement error of the microprobe system the sample can be considered as stoichiometric, perhaps with a tendency of Zn excess resulting in a slight B-type off-stoichiometry (Figure 4.5). These off-stoichiometric models were first introduced in Ref. [31] and extended by Ref. [32]. Finally, the integral chemical composition can be calculated as $Cu_{2.00(4)}Zn_{1.02(2)}Sn_{0.99(2)}S_{4.00(8)}$.
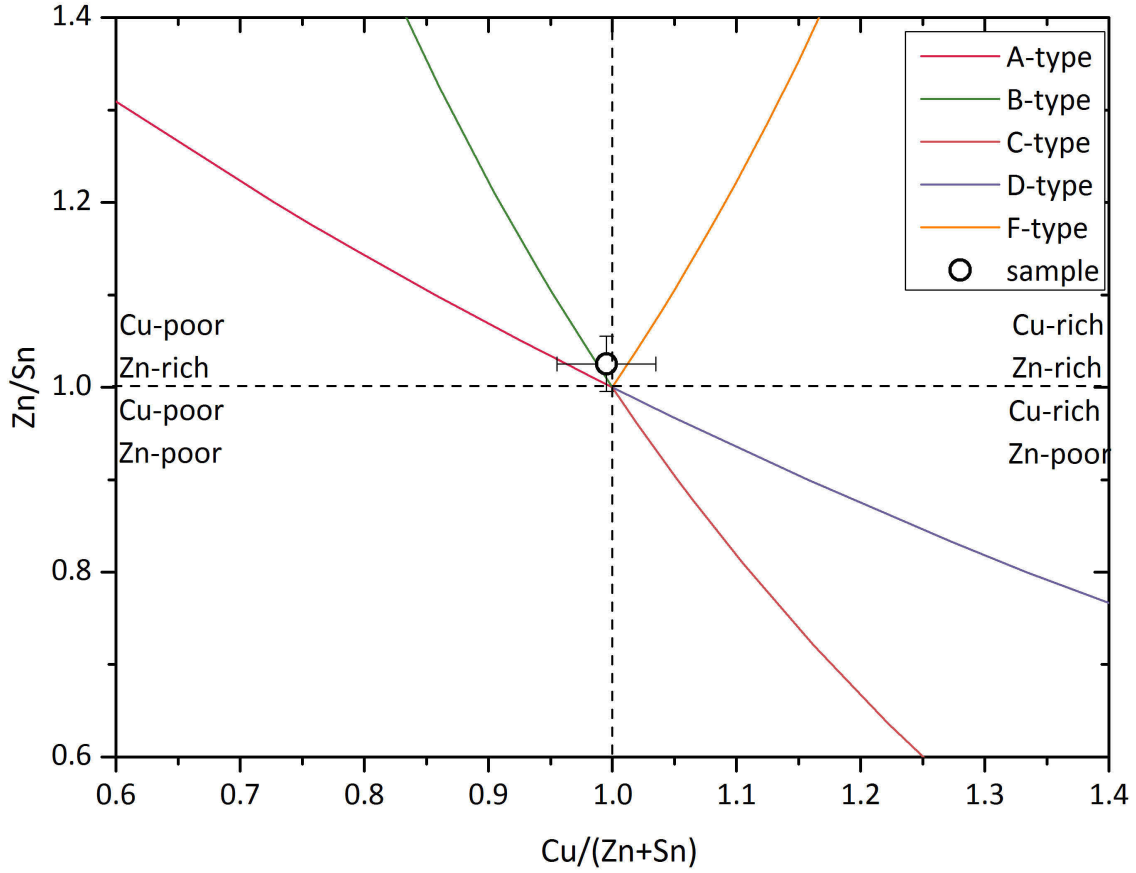
Figure 4.5.: Cu/(Zn+Sn) – Zn/Sn plot showing the position of the mechanochemically prepared CZTS sample

Furthermore, phase purity was investigated by XANES. As explained in Ref. [7], X-ray absorption near edge structure analysis at the sulfur K-edge (2472 eV) gives information about the chemical environment of the selected atom, in this case sulfur, the electronic density of the unoccupied states, and the local crystal structure. It can be considered as a fingerprint for the identification of different materials [33]. The spectra of the binary phases CuS, ZnS, and SnS as well as that of CZTS are depicted in Figure 4.6. As already shown in [7] the spectra significantly differ from each other.

Therefore, it is possible to identify secondary phases in CZTS samples. To perform a quantitative analysis of the secondary phases the measured spectrum was compared to a reference sample which can be assumed to be single phase CZTS and was already measured in Ref. [7]. The spectrum was fitted with a linear combination of the reference spectrum and the spectra of CuS, SnS, and ZnS. The absolute error of the linear combination analysis depends on the fitting details as well as the reference sample purity and was estimated to be $\pm 3\%$ [7]. Both spectra slightly differ around energies of 2469 eV and 2473 eV. The
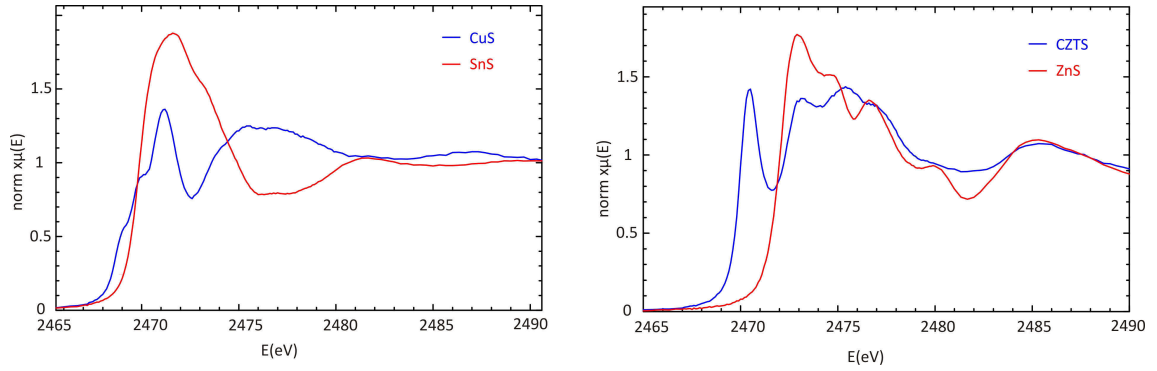
Figure 4.6.: Edge step normalized XANES spectra at the sulfur K-edge of CZTS and corresponding binary sulfides

origin of these differences could so far not be identified. However, with linear combination analysis the presence of CuS, SnS or ZnS in significant amounts ($> 3\,\%$) could be excluded. Additionally, in Figure 4.7 the CZTS sample is comparison with the CZTS reference sample is shown.

The results of the quantitative analysis by hot gas extraction showed that no significant amounts of nitrogen or oxygen are present in the sample.
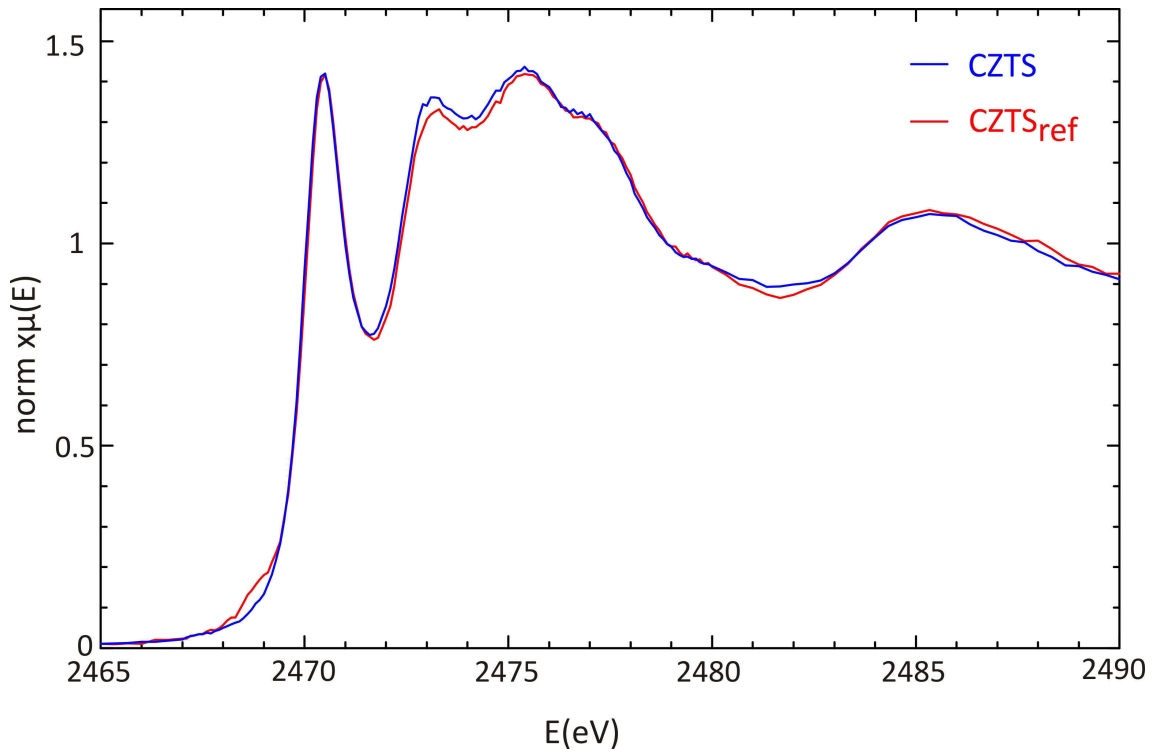
Figure 4.7.: Measured and edge step normalized XANES spectra of the CZTS powder in comparison with the reference sample $CZTS_{ref}$

4.4.3. Structural characterization

As mentioned above, the crystal structure of the synthesized black powder was refined with the help of the Rietveld method. As structural starting model we used the kesterite type (space group $I\bar{4}$). As the powder was detected to be stoichiometric within the standard deviation the stoichiometric composition Cu_2ZnSnS_4 was used for the structural refinement. The X-ray powder diffraction pattern with the results of the Rietveld refinement is depicted in Figure 4.4 b. Looking at the difference plot it is obvious that refinement succeeded very well, thus the experimental data are in a very good agreement with the theoretical ones. Refined lattice parameters and residual values of the sample are summarized in Table 4.1

Table 4.1.: Lattice parameters and residual values of the Rietveld refinement of CZTS sample

X-ray diffraction	
Structure type	kesterite
Crystal system	tetragonal
Space group	$I\bar{4}$ (No.82)
Diffractometer	Panalytical X'Pert PRO
Wavelength	154.06 pm, 154.44 pm
2ϑ range	$10-120°$
Z	2
a / pm	543.409(3)
c / pm	1084.210(11)
R_{Bragg} / %	3.89
R_{wp} / %	1.98
R_{exp} / %	1.07
S	1.85

As it is not possible to differentiate between Zn and Cu with conventional X-ray powder diffraction methods, this experiment can only be used to distinguish between Cu/Zn and Sn. Following constraints were applied:

- The stoichiometric composition Cu_2ZnSnS_4 was used
- The sum of Cu/Zn on all positions is 3
- The sum of Sn on all positions is 1
- Each cation position has a total occupancy of 1
- For the thermal motion an overall Debye-Waller factor was used

Table 4.2 lists the final atomic and additional structural parameters from the X-ray refinement. In conformity with literature data Sn was found on Wyckoff position $2b$ $(0, 0, 1/2)$,

Table 4.2.: Refined structural parameters of CZTS from X-ray diffraction data. Occ for each cation position ($2a$, $2c$, $2d$, $2b$) was constraint to 1. Values larger than 1 or below 0 are not meaningful and have to be considered as 1 and 0, respectively.

Atom	Wyckoff	x	y	z	B_{iso}	occ
Cu/Zn	$2a$	0	0	0	0.991(9)	1.008(2)
Sn	$2a$	0	0	0	0.991(9)	-0.008(2)*
Cu/Zn	$2c$	0	1/2	1/4	0.991(9)	1.001(9)
Sn	$2c$	0	1/2	1/4	0.991(9)	-0.001(9)*
Cu/Zn	$2d$	0	1/2	3/4	0.991(9)	0.967(10)
Sn	$2d$	0	1/2	3/4	0.991(9)	0.033(10)
Cu/Zn	$2b$	0	0	1/2	0.991(9)	0.023(2)
Sn	$2b$	0	0	1/2	0.991(9)	0.977(2)
S	$8g$	0.755(3)	0.757(3)	0.8718(2)	0.991(9)	4

whereas Cu/Zn is located on $2a$ $(0, 0, 0)$, $2c$ $(0, 1/2, 1/4)$, and $2d$ $(0, 1/2, 3/4)$ sites. No Sn was found on positions $2a$ and $2c$. However, around $3\,\%$ of Sn, that is present in the sample, is found on $2d$ site. Missing Sn on the $2b$ site is replaced by Cu/Zn.

With the aim to reveal also the copper/zinc cation ordering on the four crystallographic sites, neutron diffraction measurements of the product were performed. Two strategies for the refinement were tested.

Strategy A:

- The stoichiometric composition Cu_2ZnSnS_4 was applied
- The sum of Cu on all positions is 2
- The sum of Zn on all positions is 1
- The values of Sn were adopted to the values of the XRD-refinement and not refined
- Each cation position has a total occupancy of 1

As described above, the occupancy values for Sn were fixed to the values obtained from our X-ray refinement (Wyckoff positions $2d$ and $2b$) whereas the occupancy values of Cu and Zn were refined on positions $2a$ $(0, 0, 0)$, $2c$ $(0, 1/2, 1/4)$, $2d$ $(0, 1/2, 3/4)$, and $2b$ $(0, 0, 1/2)$. The neutron powder diffraction pattern together with the results of the Rietveld refinements is depicted in Figure 4.8. The final atomic and additional structural parameters are summarized in Table 4.4. Looking at the site occupancy factors it can be seen that the $2a$ site is primarily occupied by Cu with small amounts of additional Zn. However, within the error of the refinement the Zn content on this position can be considered as zero. Cu is also the dominant element on the $2c$ site whereas the $2d$ position

is mainly occupied with Zn. This is in good agreement with the literature data of ordered
kesterite phases where Cu fully occupies the $2c$ and Zn the $2d$ position. No Zn was found
on the $2b$ site. This is summarized in Figure 4.8.

Table 4.3.: Lattice parameters and residual values of the Rietveld refinement from Neutron
diffraction data

	X-ray diffraction	
Structure type	kesterite	
Crystal system	tetragonal	
Space group	$I\bar{4}$ (No. 82)	
Diffractometer	SPODI	
Wavelength	154.83 pm	
2ϑ range	$10-150°$	
Z	2	
a / pm	543.547(2)	543.547(2)
c / pm	1084.438(7)	1084.438(7)
R_{Bragg} / %	1.68	1.76
R_{wp} / %	2.45	2.45
R_{exp} / %	1.62	1.62
S	1.51	1.51

Table 4.4.: Refined structural parameters from neutron diffraction data (strategy A). *re-
fined values from X-ray diffraction data

Atom	Wyckoff	x	y	z	B_{iso}	occ
Cu	$2a$	0	0	0	2.28(10)	0.97(4)
Zn	$2a$	0	0	0	2.28(10)	0.04(4)
Cu	$2c$	0	1/2	1/4	0.9(2)	0.75(7)
Zn	$2c$	0	1/2	1/4	0.9(2)	0.25(7)
Cu	$2d$	0	1/2	3/4	0.6(2)	0.26(4)
Zn	$2d$	0	1/2	3/4	0.6(2)	0.71(4)
Sn	$2d$	0	1/2	3/4	0.6(2)	0.033*
Cu	$2b$	0	0	1/2	0.92(8)	0.001(9)
Zn	$2b$	0	0	1/2	0.92(8)	0.023(2)
Sn	$2b$	0	0	1/2	0.92(8)	0.977*
S	$8g$	0.758(2)	0.751(3)	0.8756(10)	0.85(3)	4

Strategy B:

As a second approach the method of the average neutron scattering length, which was introduced by Schorr [34] for determination of the cation distribution of different semiconductor compounds, was applied (strategy B). For this refinement the slight off-stoichiometric composition $Cu_{2.00(4)}Zn_{1.02(2)}Sn_{0.99(2)}S_{4.00(8)}$ was used. As starting model the cations were distributed on the four lattice sites as follows: Cu on the Wyckoff positions $2a$ $(0, 0, 0)$ and $2c$ $(0, 1/2, 1/4)$, Zn on $2d$ $(0, 1/2, 3/4)$, and Sn on $2b$ $(0, 0, 1/2)$. Refined parameters are summarized in Table 4.5. The neutron powder diagram together with the results of the Rietveld refinements is depicted in Figure 4.8.

Table 4.5.: Refined structural parameters from neutron diffraction data (strategy B).

Atom	Wyckoff	x	y	z	B_{iso}	occ
Cu	$2a$	0	0	0	2.33(10)	1.02(2)
Cu	$2c$	0	1/2	1/4	0.8(2)	0.91(3)
Zn	$2d$	0	1/2	3/4	0.7(2)	1.11(4)
Sn	$2b$	0	0	1/2	0.96(8)	1.01(2)
S	$8g$	0.750(3)	0.758(2)	0.8757(10)	0.83(3)	4

The refined site occupancies are used to calculate the experimental average neutron scattering lengths according to Equation 1.

$$\bar{b}_{2a}^{exp} = occ_{2a} \cdot b_{Cu} \tag{4.1}$$

$$\bar{b}_{2c}^{exp} = occ_{2c} \cdot b_{Cu}$$

$$\bar{b}_{2d}^{exp} = occ_{2d} \cdot b_{Zn}$$

$$\bar{b}_{2b}^{exp} = occ_{2b} \cdot b_{Sn}$$

where $\bar{b}^{exp}$ is the experimental determined average neutron scattering length of the site, occ the occupancy of the respective site, and b is the scattering length of the particular cation ($b_{Cu} = 7.718\,\mathrm{fm}$, $b_{Zn} = 5.680\,\mathrm{fm}$, $b_{Sn} = 6.225\,\mathrm{fm}$).

The obtained values for the average neutron scattering lengths are compared with the neutron scattering lengths of Cu, Zn, and Sn. An occurring deviation from the initial value shows that the cation sites $2c$ and $2d$ are not exclusively occupied by the presumed atom. For the calculation of the cation distribution Equation 1.2 is used.

$$\bar{b}_i = X_i \cdot b_{Cu} + Y_i \cdot b_{Zn} + Z_i \cdot b_{Sn} \tag{4.2}$$

where $\bar{b}_i$ is the average neutron scattering length of site i ($2a$, $2c$, $2d$, $2b$), X_i, Y_i, and Z_i the fraction of Cu, Zn, and Sn on the respective site, and b is again the scattering length of the cation. In the global optimization procedure all values were simultaneously optimised and the following conditions have to be fulfilled: minimisation of the difference between $\bar{b}^{exp}$ and $\bar{b}_i$ each position is fully occupied; there is no deviation from the given stoichiometry.

From strategy B following supposition can be made: $2a$ is fully occupied by copper. The average neutron scattering length of the $2c$ site is significantly lower than compared to full occupancy with Cu, suggesting the presence of Zn_{Cu} or Sn_{Cu} antisites. However, significant amounts of Sn_{Cu} antisites on the $2c$ site were excluded by the X-ray refinement. An indication for Cu_{Zn} antisites is suggested on the $2d$ site due to the significantly higher average neutron scattering length compared to the value of Zn. The value for Sn on the $2b$ site would suggest that only Sn is present on this position. All this is summarized in Figure 4.9.
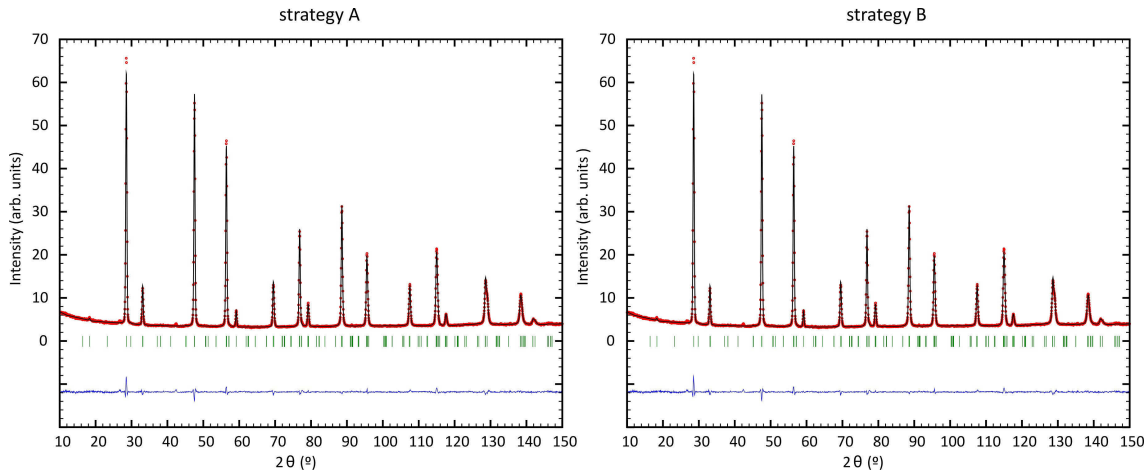
Figure 4.8.: Neutron powder diffraction pattern with results of Rietveld refinements using the kesterite-type structure as starting model. (left – strategy A, right – strategy B)

From the results presented in Table 4.3 it is obvious that both refinements succeeded very well. Comparing the lattice parameters, residual values, and structural parameters no significant differences are observed. However, two deviations of the results of both refinements have to be mentioned. Zn was found in the amount of 4 % on the $2a$ site in strategy A whereas in strategy B no Zn was found on this position. By taking into account the error of the refined parameter Zn_{2a} in strategy A the Zn content can be considered as zero though. Secondly, Sn_{Zn} of ~ 2 % are found on the $2d$ site in strategy A, assuming a stoichiometric composition Cu_2ZnSnS_4. Using the composition $Cu_{2.00(4)}Zn_{1.02(2)}Sn_{0.99(2)}S_{4.00(8)}$ in strategy B, the entire amount of Sn is on the $2b$ site.
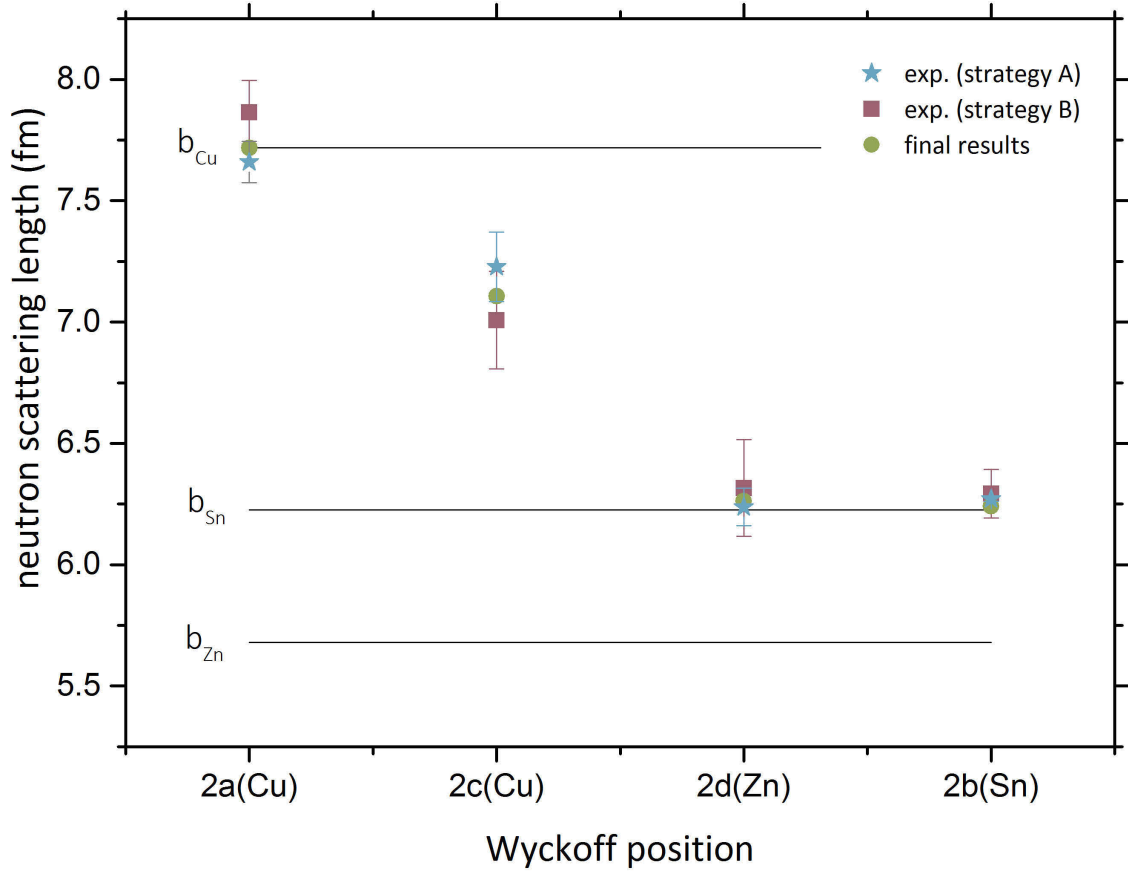
Figure 4.9.: Experimentally determined values of the average neutron scattering length $\bar{b}$ of the $2a$, $2c$, $2d$, and $2b$ sites for strategy A and B and final values resulting from both strategies

In Figure 4.9 the experimentally determined average neutron scattering lengths for the cation sites for both refinement strategies and the calculated values ($\bar{b}_i$) are compared. It can be easily seen that the values for both strategies are in good agreement with each other.

Independently from the refinement strategy the following statements can be made: cation site 2a is fully occupied by copper. On the $2c$ site the presence of Zn_{Cu} antisites is clearly seen (~28 %). An additional indication comes from the occupancy factors of the $2d$ site (presence of Cu_{Zn} in the order of ~28 %). The determined values for the $2b$ site suggest that within the experimental error this site is only occupied by tin. This is summarized in Figure 4.10 and Figure 4.10.
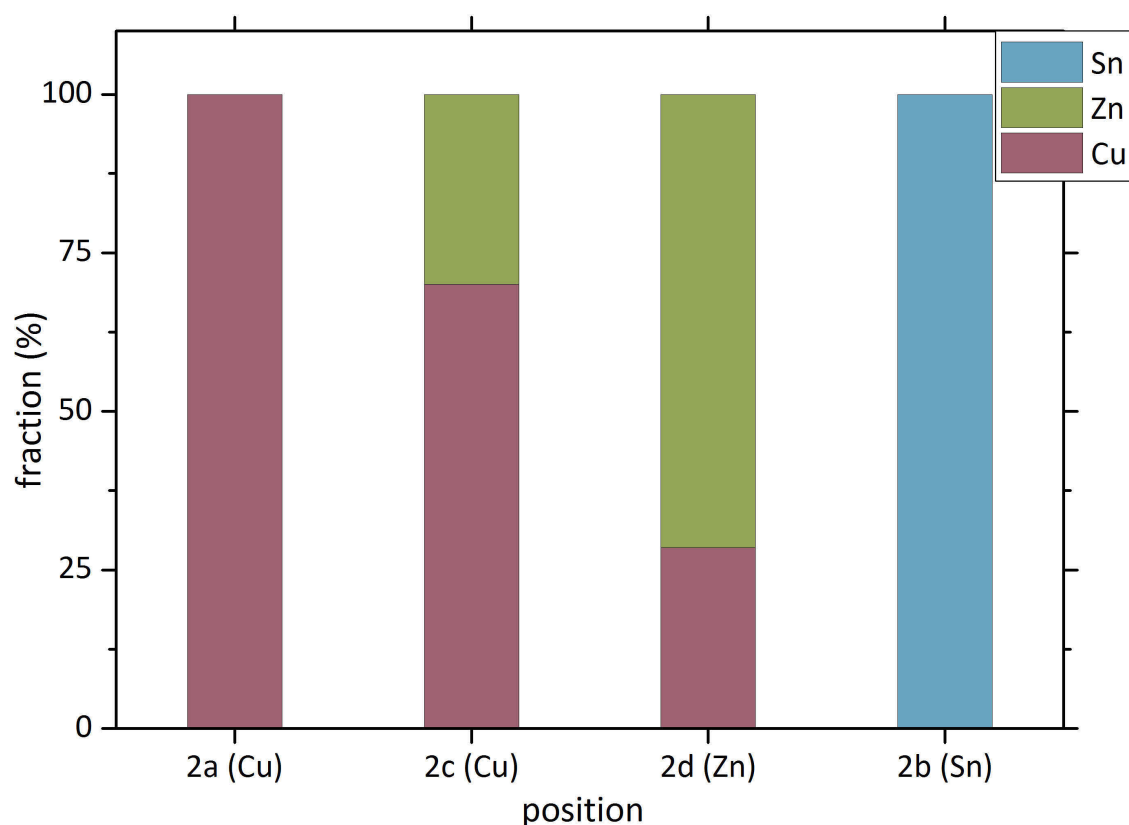
Figure 4.10.: Cation distribution of the synthesized sample

4.5. Conclusions

A mechanochemical synthesis route to CZTS was successfully developed. The synthesis process includes a milling step, which is essential to produce phase pure powder, and an annealing step at $500\,°C$. This reaction temperature is favorable as it is comparable to the temperatures actually used during thin films growth and is close to the real technical process conditions. WDS measurements confirmed a stoichiometric chemical composition of $Cu_{2.00(4)}Zn_{1.02(2)}Sn_{0.99(2)}S_{4.00(8)}$ and no secondary phases were found in XANES. The results of diffraction studies showed that the powder crystallizes in the kesterite-type structure. The cation distribution was determined by neutron powder diffraction measurements and revealed a partially disordered kesterite type. The ordering of the cations should significantly depend on the cooling rate of the sample during preparation. For different cooling procedures we expect a differing distribution of the cations. In order to investigate this phenomenon, additional neutron scattering experiments are scheduled.

With the developed mechanochemical route it is nicely possible to control the composition of the synthesized powder. Therefore, additional experiments to prepare phase-pure off-stoichiometric CZTS material are planned.

Acknowledgement

References

[1] S. Chen, X.G. Gong, A. Walsh, S.-H. Wei, *Appl. Phys. Lett.* **2009**, *94*, 041903/1 − 041903/3.

[2] J.J. Scragg, P.J. Dale, L.M. Peter, G. Zoppi, I. Forbes, *Phys. Status Solidi B* **2008**, *245*, 1772 − 1778.

[3] S. Siebentritt, S. Schorr, *Prog. Photovoltaics* **2012**, *20*, 512 − 519.

[4] B. Shin, O. Gunawan, Y. Zhu, N.A. Bojarczuk, S.J. Chey, S. Guha, *Prog. Photovoltaics* **2013**, *21*, 72 − 76.

[5] S. Schorr, H.-J. Hoebler, M. Tovar, *Eur. J. Mineral.* **2007**, *19*, 65 − 73.

[6] S. Schorr, G. Gonzalez-Aviles, *Phys. Status Solidi A* **2009**, *206*, 1054 − 1058.

[7] J. Just, D. Luetzenkirchen-Hecht, R. Frahm, S. Schorr, T. Unold, *Appl. Phys. Lett.* **2011**, *99*, 262105/1 − 262105/3.

[8] S. Chen, X.G. Gong, A. Walsh, S.-H. Wei, *Appl. Phys. Lett.* **2010**, *96*, 021902/1 − 021902/3.

[9] S. Chen, L.-W. Wang, A. Walsh, X.G. Gong, S.-H. Wei, *Appl. Phys. Lett.* **2012**, *101*, 223901/1 − 223901/4.

[10] A.J. Jackson, A. Walsh, *J. Mater. Chem. A*, **2014**, 7829 − 7836.

[11] S.R. Hall, J.T. Szymanski, J.M. Stewart, *Can. Mineral.* **1978**, *16*, 131 − 137.

[12] S. Schorr, *Sol. Energy Mater. Sol. Cells* **2011**, *95*, 1482 − 1488.

[13] L. Choubrac, A. Lafond, C. Guillot-Deudon, Y. Moelo, S. Jobic, *Inorg. Chem.* **2012**, *51*, 3346 − 3348.

[14] S. Schorr, M. Tovar, B*ENSC Experimental Report* **2006**.

[15] M.Y. Valakh, V.M. Dzhagan, I.S. Babichuk, X. Fontane, A. Perez-Rodriquez, S. Schorr, *JETP Lett.* **2013**, *98*, 255 − 258.

[16] A. Nagoya, R. Asahi, R. Wahl, G. Kresse, *Phys. Rev. B Condens. Matter Mater. Phys.* **2010**, *81,* 113202/1 – 113202/4.

[17] S. Chen, J.-H. Yang, X.G. Gong, A. Walsh, S.-H. Wei, *Phys. Rev. B: Condens. Matter Mater. Phys.* **2010**, *81*, 245204/1 – 245204/10.

[18] J.J.S. Scragg, L. Choubrac, A. Lafond, T. Ericson, C. Platzer-Bjoerkman, *Appl. Phys. Lett.* **2014**, *104*, 041911/1 – 041911/4.

[19] I.D. Olekseyuk, I.V. Dudchak, L.V. Piskach, *J. Alloys Compd.* **2004**, *368*, 135 – 143.

[20] J. Timo Waetjen, J. Engman, M. Edoff, C. Platzer-Bjoerkman, *Appl. Phys. Lett.* **2012**, *100*, 173510/1 – 173510/3.

[21] H. Wiedemeier, F.J. Csillag, *Thermochim. Acta* **1979**, *34,* 257 – 265.

[22] M. Hoelzel, A. Senyshyn, N. Juenke, H. Boysen, W. Schmahl, H. Fuess, *Nucl. Instrum. Methods Phys. Res., Sect. A* **2012**, *667*, 32 – 37.

[23] H.M. Rietveld, *J. Appl. Crystallogr.* **1969**, *2*, 65 – 71.

[24] J. Rodriguez-Carvajal, *Abstracts of the Satellite Meeting on Powder Diffraction of the XV.Congress of the IUCr* **1990**, 127.

[25] P. Thompson, D.E. Cox, J.B. Hastings, *J. Appl. Crystallogr.* **1987**, *20*, 79 – 83.

[26] M. Newville, *J. Synchrotron Radiat.* **2001**, *8*, 322 – 324.

[27] B. Ravel, M. Newville, *J. Synchrotron Radiat.* **2005**, *12*, 537 – 541.

[28] G.P. Bernardini, P. Bonazzi, M. Corazza, F. Corsini, G. Mazzetti, L. Poggi, G. Tanelli, *Eur. J. Mineral.* **1990**, *2*, 219 – 225.

[29] J.J. Scragg, T. Ericson, X. Fontane, V. Izquierdo-Roca, A. Perez-Rodriguez, T. Kubart, M. Edoff, C. Platzer-Bjoerkman, *Prog. Photovoltaics* **2014**, *22*, 10 – 17.

[30] B.-A. Schubert, B. Marsen, S. Cinque, T. Unold, R. Klenk, S. Schorr, H.-W. Schock, C. Platzer-Bjoerkman, *Prog. Photovoltaics* **2011**, *19*, 93 – 96.

[31] A. Lafond, L. Choubrac, C. Guillot-Deudon, P. Deniard, S. Jobic, *Z. Anorg. Allg. Chem.* **2012**, *638*, 2571 – 2577.

[32] L.E. Valle Rios, K. Neldner, G. Gurieva, S. Schorr, *J. Alloys Compd.* **2016**, *657*, 408 – 413.

[33] D.C. Koningsberger, R. Prins, *X-ray Absorption: Principles, Applications, Techniques of EXAFS SEXAFS, and XANES*, John Wiley & Sons, **1988**, 673.

[34] S. Schorr, C. Stephan, T. Toerndahl, R. Mainz in, Wiley-VCH Verlag GmbH & Co. KGaA, **2011**, 347 – 363.

5. Publication 2

The order-disorder transition in Cu_2ZnSnS_4 – a neutron scattering investigation

Anna Ritscher, Markus Hoelzel, Martin Lerch

Contribution to publication:

A. Ritscher:	Sample preparation, analysis and evaluation, writing.
M. Hoelzel:	Measurements (neutron diffraction).
M. Lerch:	General advice and helpful comments, proofreading.

Overall contribution of A. Ritscher to the publication: 90 %

Authors   A. Ritscher [1,2], M. Hoelzel [3], M. Lerch [*][1]

[1] Institut für Chemie, Technische Universität Berlin, Straße des 17.Juni 115, 10623 Berlin, Germany

[2] Helmholtz-Zentrum Berlin für Materialien und Energie, Hahn-Meitner-Platz 1, 14109 Berlin, Germany

[3] Heinz Maier-Leibnitz Zentrum (MLZ), Technische Universität München, Lichtenbergstr.1, 85748 Garching, Germany

[*] corresponding author

5.1. Abstract

In this work a series of stoichiometric Cu_2ZnSnS_4 (CZTS) samples annealed at different temperatures in the range of $473-623\,K$ were investigated. The temperature dependence of the Cu/Zn-order-disorder behavior was analyzed by neutron powder diffraction measurements. Cu fully occupies the $2a$ and Sn the $2b$ position within the whole temperature range. For Zn and the remaining Cu on sites $2d$ and $2c$, a clear change from ordered to disordered kesterite structure is found. The critical temperature T_c for this Landau-type second order transition was determined as $552 \pm 2\,K$. It was found that in Cu_2ZnSnS_4 very long annealing times are necessary to reach equilibrium at low temperatures.

5.2. Introduction

The quaternary chalcogenide Cu_2ZnSnS_4 and related compounds recently attract much attention as prospective absorber materials for thin film solar cell technology. This direct band gap p-type semiconductor with an optical band gap energy value of $1.5\,eV$ and an absorption coefficient in the order of $10^{-4}\,cm^{-1}$ contains only abundant and non-toxic elements [1-3]. Consequently, it would be a suitable alternative to other chalcogenide-based absorber materials such as CdTe or CIGS $(CuIn_xGa_{(1-x)}Se_2)$ that are currently used. Up to now record efficiencies of CZTS-based thin films of $12.6\,\%$ are reported for devices that additionally contain selenium [4]. Yet, compared to the currently used chalcopyrite materials, efficiencies are significantly lower due to the limiting open-circuit voltage V_{oc}. It is assumed that the low V_{oc} is caused by the existence of band gap fluctuations. Various reasons for the decrease of the effective band gap such as inclusions of stannite or the occurrence of $[Cu^-_{Zn} + Sn^{2+}_{Zn}]$ defect complexes were suggested [3, 5]. Recently, it was shown by experimental and theoretical studies that the band gap fluctuations of $100-200\,meV$ can be primary attributed to the disorder among the Cu and Zn cations in the crystal structure [6]. The significant reduction of the effective band gap is caused by the high number of $[Cu_{Zn} + Zn_{Cu}]$ defect pairs and the clustering of those defect pairs was studied by *ab initio* calculations [6].

Cu_2ZnSnS_4 crystallizes in the kesterite type (space group $I\bar{4}$) [7, 8]. Four different cation sites are available in the structure. In the fully ordered kesterite structure Sn is located on site $2b$ $(0, 0, 1/2)$, one Cu occupies the $2a$ $(0, 0, 0)$ position, the remaining Cu is located on position $2c$ $(0, 1/2, 1/4)$, Zn on $2d$ $(0, 1/2, 3/4)$. The sphalerite-type derived crystal structure can be described by the stacking of cation layers along the c-axis (Cu/Sn on $z = 0$ and $z = 1/2$; Cu/Zn at $z = 1/4$ and $z = 3/4$) separated by layers of sulfur atoms. Diffraction studies of CZTS powder samples report a partial [9, 10] or complete disorder [11] of Cu and Zn on the $2c$ and $2d$ positions. Kesterite-type phases exhibiting a statistical

distribution of Cu and Zn on the two latter sites can be described in space group $I\bar{4}2m$ with Zn and Cu occupying the $4d$ $(0, 1/2, 1/4)$ Wyckoff position which is called disordered kesterite [12]. Consequently, the cation layers at $z = 1/4$ and $z = 3/4$ are involved in the order-disorder process. Furthermore, it was shown by *ab initio* calculations [13, 14] that the point defects Cu_{Zn} and Zn_{Cu} have very low formation energies and thus Cu/Zn disorder is highly possible. In Figure 5.1 the fully ordered and the disordered kesterite structure are depicted.
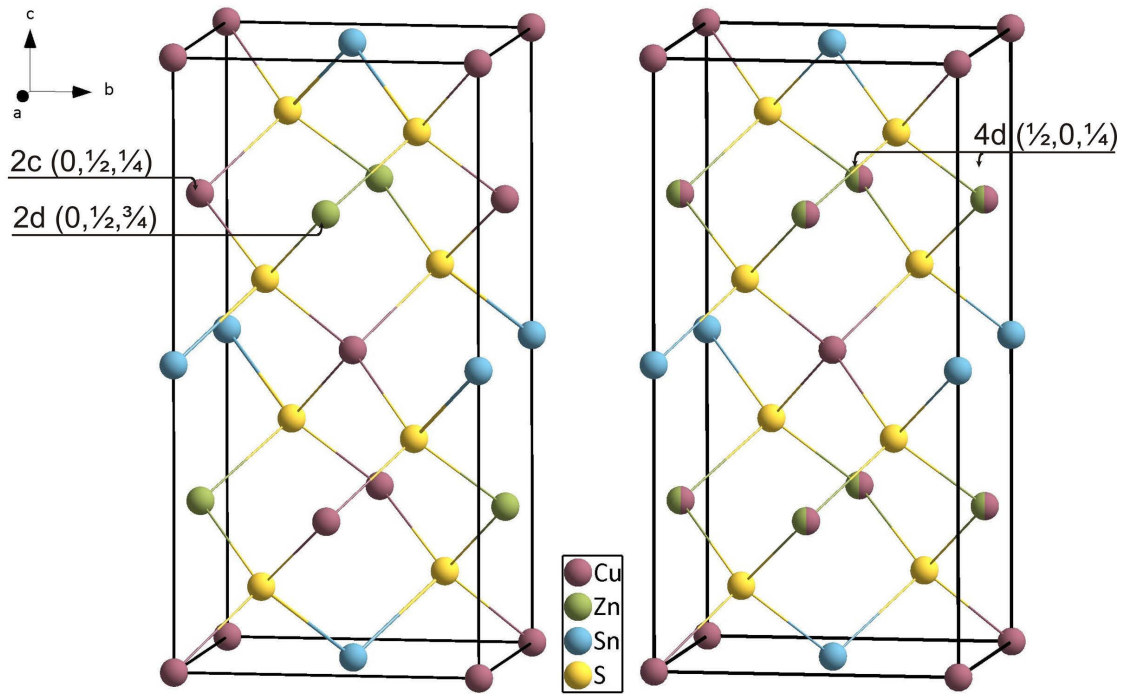
Figure 5.1.: Unit cells of ordered (left) and disordered kesterite (right); sites involved in the order-disorder transition are labeled. In the ordered kesterite Cu occupies position $2c$ whereas Zn is located on $2d$. In disordered kesterite the cations are statistically distributed on these two cation positions leading to a change in the space group from $I\bar{4}$ to $I\bar{4}2m$ and consequently a change to Wyckoff position $4d$.

Until now only few studies on the ordering in CZTS were carried out. The local structure of defects in Cu-poor/Zn-rich material was investigated by solid-state NMR and Raman spectroscopy [15]. X-ray resonant diffraction measurements at the Cu-K_a and Zn-K_a absorption edge were carried out to analyse the Cu/Zn ordering in a CZTS single crystal [16]. Furthermore, CZTS thin films were studied to track the Cu/Zn disorder [6, 17]. In those studies near-order resonant Raman measurements of Zn rich thin films were carried out. The critical temperature for the transition from ordered to disordered kesterite was determined as 533 ± 10 K. In high temperature X-ray diffraction measurements of a kesterite

powder sample using synchrotron radiation a kink in the temperature dependent lattice parameter variation is observed at 513 K [18].

For a reliable structural characterization, which is essential for tracking the decrease in the cation order, diffraction methods are preferable. Our recent neutron diffraction study of a powder sample cooled down from 773 K predicts that Cu fully occupies the $2a$ position. Zn and the remaining Cu reveal a partial disorder of the cations on the two positions $2c$ and $2d$ (approx.: $2c$: 72 % Cu 28 % Zn, $2d$: 28 % Cu 72 % Zn) [10].

The present work was undertaken to verify the recent results of Scragg et al. [6] and to follow the order-disorder transition in the cationic network of CZTS powder samples by diffraction techniques. Using conventional X-ray diffraction methods, Cu^{+} and Zn^{2+} are not distinguishable due to their isoelectronic character. However, those two cations show a significant difference in their neutron scattering length ($b_{Cu} = 7.718(4)$ fm, $b_{Zn} = 5.680(5)$ fm). Consequently, neutron diffraction is the method of choice. Ten stoichiometric CZTS powder samples were synthesized via our recently developed mechanochemical process [10]. Taking into account the recent work of Scragg et al. [17] it is clear that the time to reach equilibrium is up to more than 24 h, making *in situ*-neutron scattering measurements not useful. Consequently, various samples were prepared by quenching.

5.3. Experimental

5.3.1. Synthesis

Recently, we developed a new route for an easy and fast synthesis of phase-pure and stoichiometric CZTS powders [10] where the quaternary sulfide was prepared by mechanical milling in a high energy planetary ball mill starting from the corresponding binary sulfides CuS, ZnS, and SnS followed by an annealing step in H_2S atmosphere. In this work ten CZTS powder samples were finally annealed in sealed and evacuated silica ampoules at different temperatures in order to follow the order-disorder transition.

For each sample the binary sulfides CuS, ZnS, and SnS were mixed in an atomic ratio of 2:1:1. As described in detail elsewhere [10] the starting compounds were prepared either by precipitation (CuS), sulfidation of the oxide (ZnS) or solid state reaction of the elements (SnS). The mixture was filled into an 80 ml agate grinding bowl with five 20 mm grinding balls under Ar atmosphere in a glove box. Milling was performed in a Fritsch Planetary Mono Mill PULVERISETTE 6 using a rotational speed of 350 rpm and a milling time of 5 h. The result of the mechanochemical treatment was a poorly crystalline powder.

In a second step each sample was annealed in a conventional tube furnace equipped with a SiO_2-tube under flowing reaction gas (H_2S) for 3 h at 773 K. Using inert gas (N_2 or Ar) instead of H_2S, the formation of secondary phases is observed. After reaction the sample

was cooled down with a cooling rate of 60 K/h. The results of this annealing step are CZTS powders with good crystallinity.

In order to obtain powders with different order parameter, a final annealing step at different temperatures in the range of 473 – 623 K was performed. The exact heating temperatures (including sample names) were T = 473 (N1, N10), 493 (N2), 503 (N3), 513 (N4), 523 (N5), 533 (N6), 543 (N7), 553 (N8), and 623 K (N9). For this purpose 4 – 5 g of CZTS powder were loaded and sealed in an evacuated silica ampoule. Each ampoule was inserted into a muffle furnace and heated for 1 week. At the end of each run the silica ampoule was quenched in cold water in order to freeze the equilibrium state and hence the cations order at the annealing temperature. In addition, for the last sample (N10) a second annealing step at a temperature of 473 K for further two weeks was performed before second quenching.

5.3.2. Characterization

Investigations of the chemical composition were performed by electron microprobe analysis (EMPA) with a JEOL JXA 8200 SuperProbe equipped with 5 wavelength dispersive X-ray spectrometers (WDS) and an energy dispersive X-ray spectrometer (EDS). A calibration of the microprobe system was done by using elemental standards Cu, Zn, Sn, and the mineral chalcopyrite for S in order to achieve reliable compositional parameters. High accuracy of the chemical composition could be obtained by measuring 25 grains of the CZTS phase averaging over 15 point measurements within each grain. The measurements of the samples were performed after the final quenching step.

The products were structurally characterized by neutron powder diffraction after checking phase purity and crystallinity by X-ray powder methods. Diffraction data were collected at the Forschungs-Neutronenquelle Heinz-Maier-Leibnitz Zentrum (MLZ, Garching) using the high resolution powder diffractometer SPODI (Ge (551) $\lambda = 154.818(2)$ pm) [19]. For neutron experiments the samples were encapsulated in a vanadium container with 0.15 mm wall thickness and 9 – 10 mm inner diameter and mounted in a sample changer. Structural refinements were performed by the Rietveld method [20] using the program FULLPROF Suite Version 2015 [21] by applying a Thompson-Cox-Hastings pseudo-Voigt function to describe the peak shape profile [22]. The kesterite type structure (space group $I\bar{4}$) was used as starting model for the refinements.

5.4. Results and discussion

In this work ten CZTS samples quenched from different temperatures in the region of $473-623\,\mathrm{K}$ were successfully synthesized. In order to ensure phase pure CZTS and to confirm the chemical composition of the synthesized samples the final powders were analyzed by WDS. This was done as also compositions beside the ideal stoichiometry can exhibit the kesterite structure. Studies on non-stoichiometric CZTS samples were carried out by Lafond et al. [23, 24] and extended by Valle-Rios et al. [25] leading to five off-stoichiometric CZTS types that can be described by different cation substitution reactions and formation of related point defect complexes. The results of our phase analyses show a homogenous composition for each sample, no secondary phases were found. The Cu/(Zn+Sn) and Zn/Sn ratios of the single phase CZTS samples were determined as $0.98-1.01$ and $1.00-1.03$, respectively, thus by taking into account the experimental error of the microprobe system all samples can be considered as stoichiometric (see Figure 5.2).
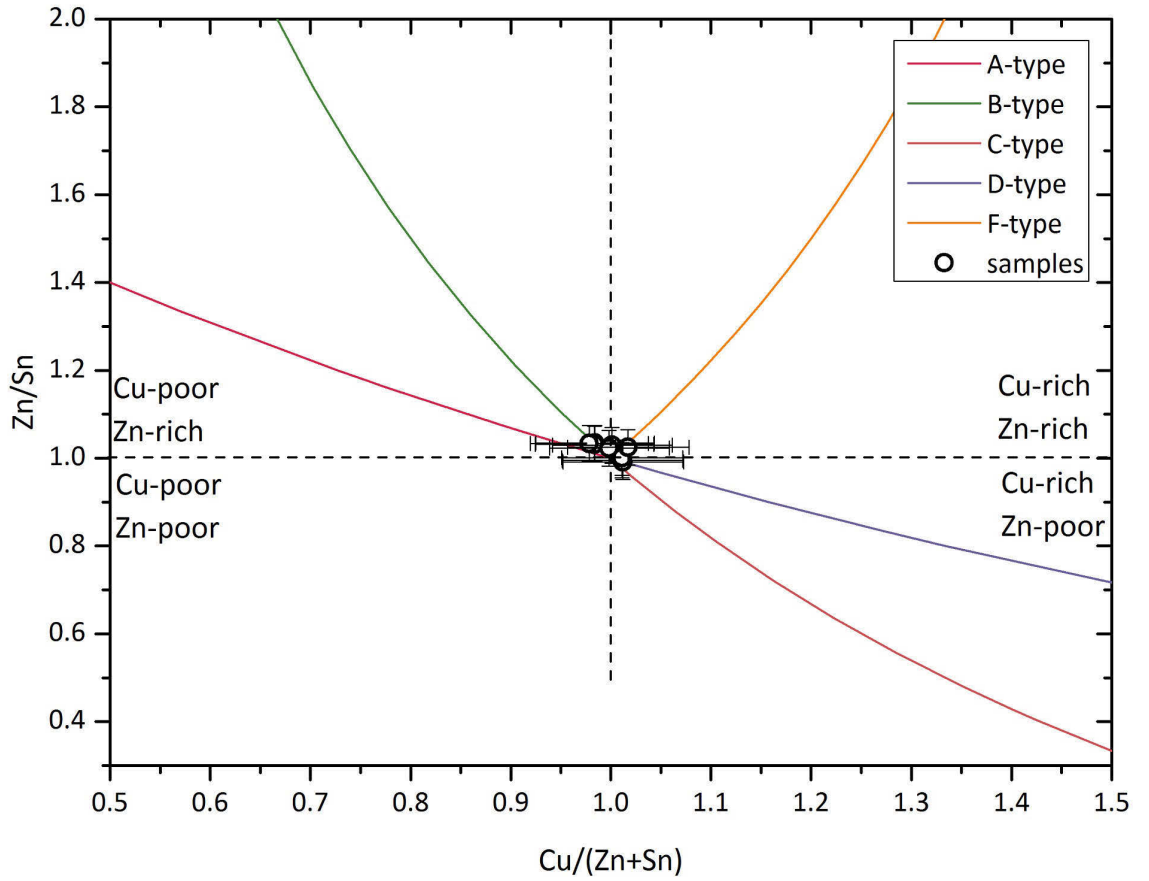
Figure 5.2.: Cu/(Zn+Sn)-Zn/Sn plot showing the position of the ten prepared CZTS samples (lines – off stoichiometric types introduced by [23-25]).

The neutron powder diffraction patterns of all samples are depicted in Figure 5.3. All powders show high crystallinity. Looking at the diffraction patterns (see Figure 5.4) of samples N1, quenched from the lowest temperature (maximum order expected), and N9, quenched from the highest temperature (statistical distribution of Cu and Zn on sites $2c$ and $2d$ expected), it is clearly seen that the intensity of the superstructure reflection at $2\vartheta = 18.3°$ is decreased for sample N9. This is a clear indication for a decreased order of the cations. However, no steady intensity decrease of the superstructure reflection as it is expected for increasing disorder is observed (see Figure 5.3). Hence, in order to track the order-disorder transformation in detail the crystal structure parameters of all nine samples were refined using the Rietveld method [21]. As the powders were all detected to be stoichiometric within the standard deviation the ideal composition Cu_2ZnSnS_4 was used for the structural refinements. The kesterite-type structure (space group $I\bar{4}$) was used as starting model for the refinements. Detailed cation distribution analyses were performed.
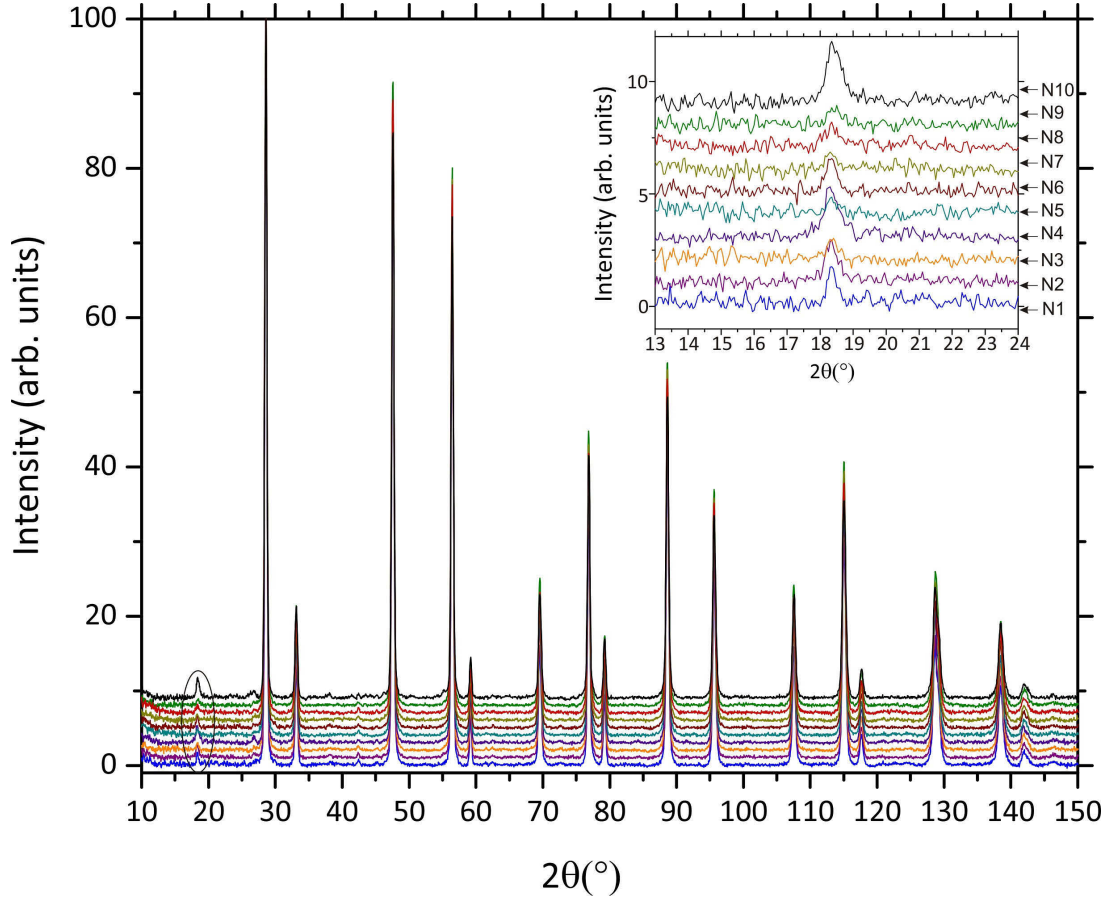
Figure 5.3.: Neutron diffraction patterns of all synthesized samples measured at the high resolution powder diffractometer SPODI ($\lambda = 154.818(2)\,$pm). In the upper right corner an enlarged part of the superstructure reflection at $2\vartheta = 18.3°$ is shown.
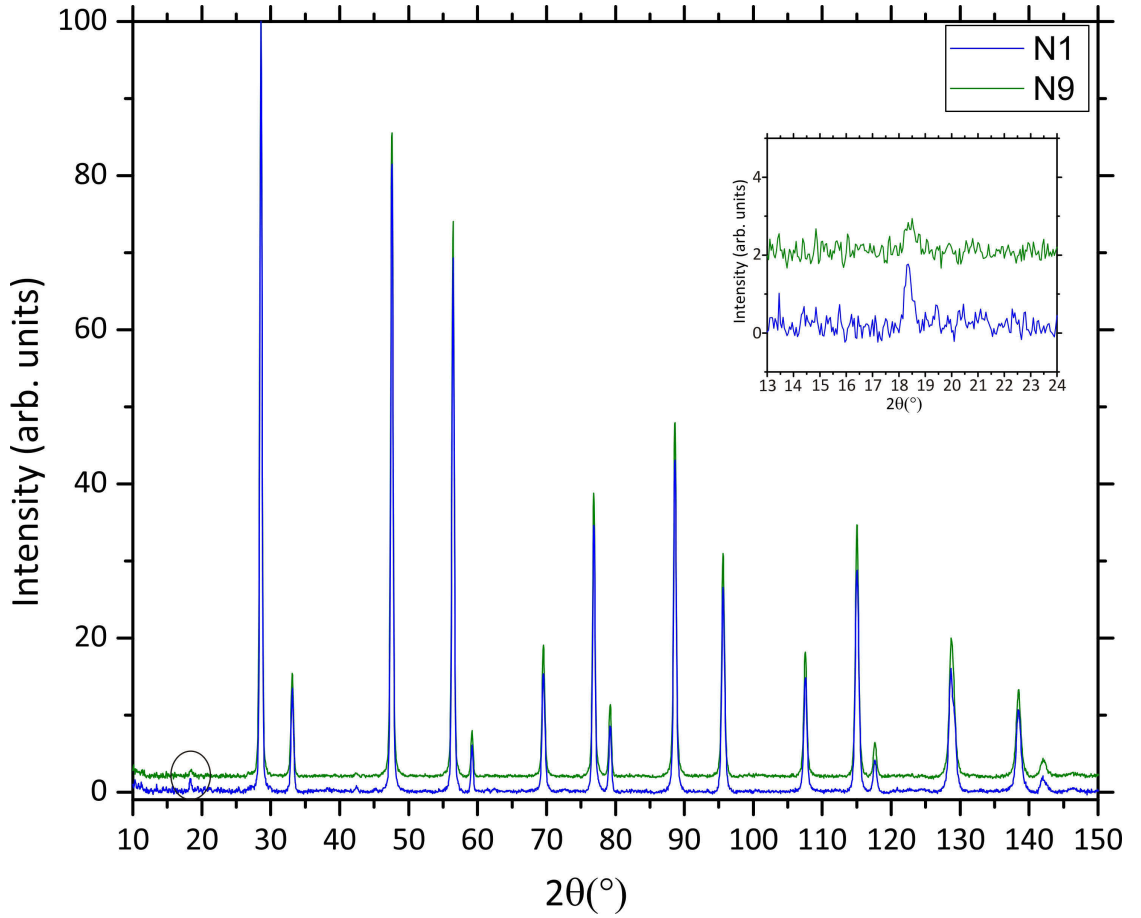
Figure 5.4.: Comparison of the diffraction pattern N1 (473 K) and N9 (623 K). In the upper right corner an enlarged part of the reflection at $2\vartheta = 18.3°$ is shown. Intensity of this superstructure reflection is decreasing which is a clear indication for a decreased order of the cations.

As a first approach the method of the average neutron scattering length was applied for determination of the cation distribution on the four positions. This method, which uses the refined site-occupancy values, was introduced by Schorr et al. [26]. As starting model the cations were distributed as follows: Cu on the Wyckoff positions $2a$ $(0,0,0)$ and $2c$ $(0,1/2,1/4)$, Zn on $2d$ $(0,1/2,3/4)$, and Sn on $2b$ $(0,0,1/2)$. These refined site occupancy value of position i (occ_i) is used to calculate the experimental average neutron scattering lengths $\bar{b}_i^{exp}$ according to Equation 1.1.

$$\bar{b}_i^{exp} = occ_i \cdot b_j \tag{5.1}$$

using the scattering lengths of the particular cation j on position i $(b_{Cu} = 7.718\,fm$, $b_{Zn} = 5.680\,fm$, $b_{Sn} = 6.225\,fm)$.

The obtained values of $\bar{b}_i^{exp}$ are compared with the neutron scattering lengths of Cu, Zn, and Sn. An occurring deviation from the initial value and consequently a discrepancy of the occupancy value would predict that the cation site is not exclusively occupied by the presumed atom. In Figure 5.5 the refined cation site occupancy values occ_{2a}, occ_{2c}, occ_{2d}, and occ_{2b} are depicted. It is clearly seen that the occupancy values for Cu_{2a} and Sn_{2b} are not changing with increasing temperature. Within the standard deviation the nominal value of 1 is reached. From that we can predict that Cu fully occupies the $2a$ and Sn the $2b$ position within the whole temperature range. Looking at Zn and the remaining Cu on positions $2d$ and $2c$, a clear change of the occupancy values is visible. While occ_{2c} is decreasing, occ_{2d} exceeds the value of 1 and a change from ordered to disordered kesterite can be presumed.
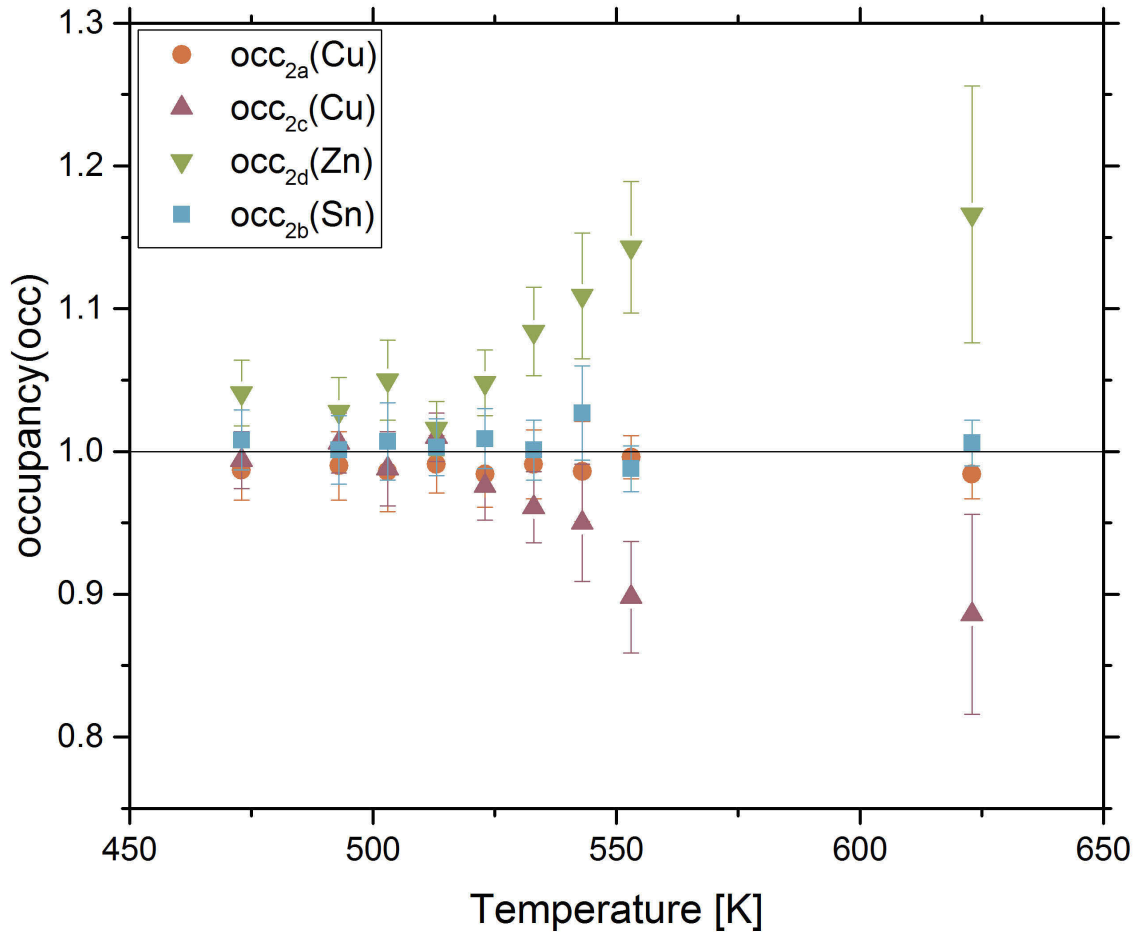
Figure 5.5.: Temperature dependence of site occupancy values occ_{2a}, occ_{2c}, occ_{2d}, and occ_{2b}. Cu fully occupies position 2a and Sn position 2b in the whole temperature range. Clear change visible at Cu_{2c} and Zn_{2d} – transformation from ordered to disordered kesterite
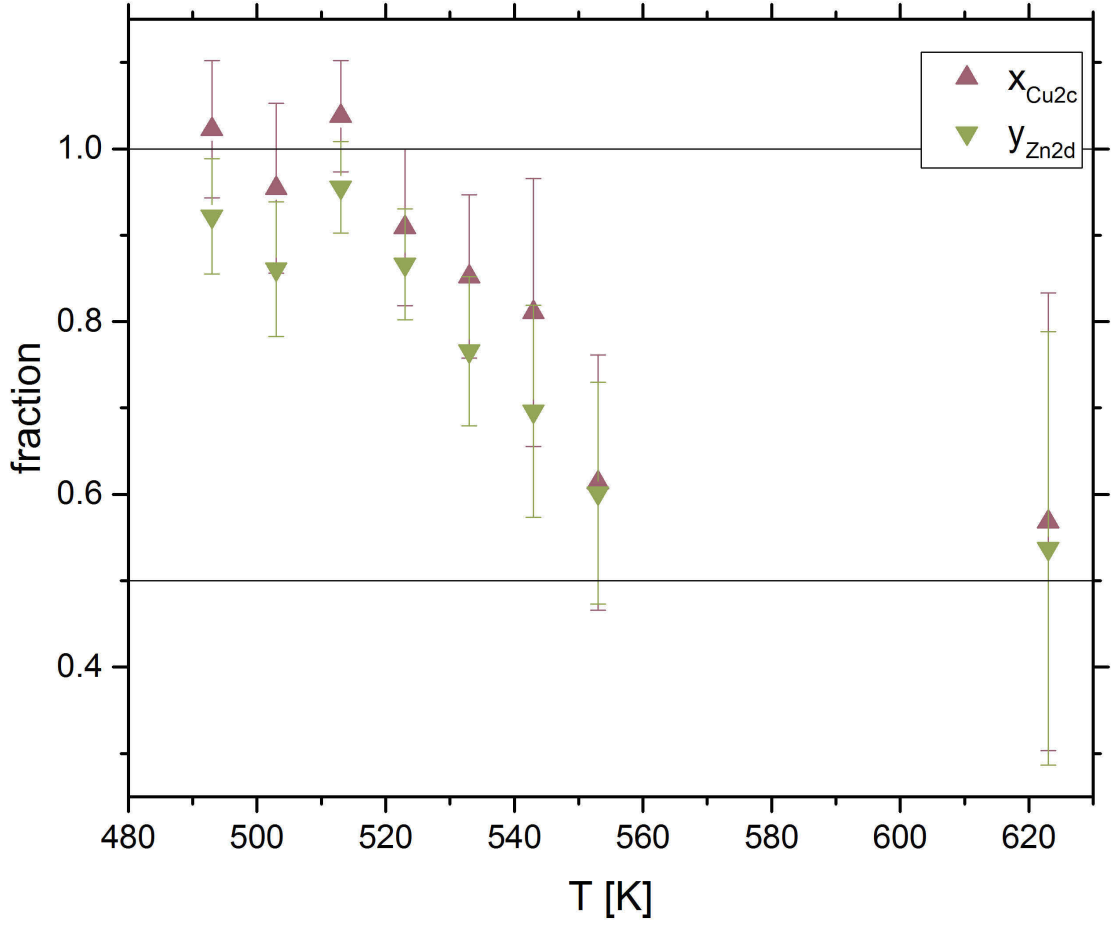
Figure 5.6.: Temperature dependence of the fraction of Cu on cation site 2c and Zn and on the 2d site. A clear change from ordered to disordered kesterite is visible.

For the calculation of the cation distribution of Cu and Zn on positions $2c$ and $2d$ Equation 1.2 is used.

$$\bar{b}_i = x_i \cdot b_{Cu} + y_i \cdot b_{Zn} \tag{5.2}$$

where x_i and y_i are the fraction of Cu and Zn on the respective site. The results of these calculations are depicted in Figure 5.6. This figure shows that the values for site $2c$ and $2d$ differ from each other but lie in the same range within the standard deviation. Due to two consecutive calculation steps the error obtained from the Rietveld refinement is summing up and the error bars are getting very large. In order to achieve more reliable values for the ratio of Cu and Zn on the two cation positions $2c$ and $2d$, and to obtain a single order parameter for each temperature, a second approach was used refining the crystal structure. As the two cations on the sites $2a$ (Cu) and $2b$ (Sn) do not reveal any significant disorder in the whole temperature range these values were set to 1 and not
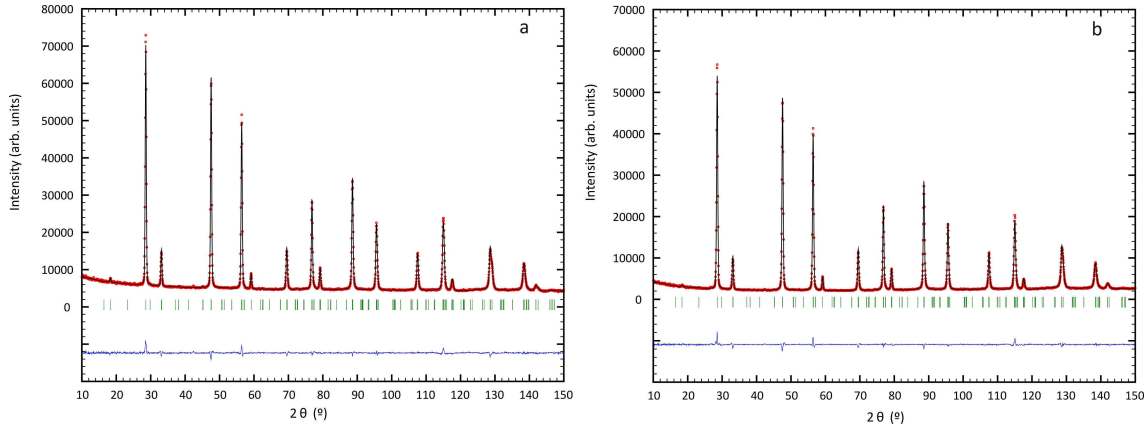
Figure 5.7.: Selected neutron powder diffraction patterns of samples N1 (473 K) (a) and N9 (623 K) (b) with the results of the Rietveld refinements.

refined during the procedure. Additionally, two side conditions were set: the sum of Cu and Zn on positions $2c$ and $2d$ must be 1 and both positions have to be fully occupied. As examples, two refinements for samples N1 and N9 are depicted in Figure 5.7. It is obvious that the refinements for both samples succeeded very well. It can be stated that the quality of the refinements is very good in the whole temperature range (see section Supplementary Data - Refinements).

In order to discuss the ordering behavior within the frame of common phase transition theories an order parameter η, ranging from 0 (disorder) to 1 (complete order), was defined, related to the order-disorder process on the two cation positions $2c$ and $2d$. η is related to the refined chemical order parameter s $(Cu(Cu_sZn_{1\text{-}s})_{Cu}(Zn_sCu_{1\text{-}s})_{Zn}SnS_4$; $1 =$ complete order, $0.5 =$ disorder) by $\eta = 2s - 1$. The observed variation of η with temperature is depicted in Figure 5.8. Three different regions may be discerned:

I. Up to 513 K Cu and Zn are strongly ordered, but no complete order within the standard deviation is reached.

II. Between 513 and 553 K there is a rapid decrease of order and the material is completely disordered at 553 K.

III. As expected, above 553 K complete disorder on $2c/2d$ positions in Cu_2ZnSnS_4 is reached. Cu and Zn show a statistical distribution on these sites. It should be mentioned that, in principle, the structural parameters of these samples (N8, N9) have to be refined in space group $I\bar{4}2m$, which is a minimal non-isomorphic supergroup of $I\bar{4}$ (index 2), as the positions $2c$ and $2d$ become equivalent and the symmetry of the structure increases. However, for better comparability of all samples and the determination of the order parameter these two samples were also refined in space

group $I\bar{4}$. The refinements using space group $I\bar{4}2m$ are presented in the section Supplementary Data - Refinements. The agreement factors are as good as the same.

Common phase transition theories predict a critical power law (CPL) in the region below the critical temperature leading to the following equation for the temperature dependence of η:

$$\eta \propto (\frac{T_c - T}{T_c})^\beta \tag{5.3}$$

with the critical temperature T_c and the critical exponent β. As may be anticipated from Figure 5.8, and known also from other compounds exhibiting an order-disorder transition [27], Equation 1.3 cannot be used for describing the whole low-temperature region. Nevertheless, a satisfactory fit is possible in region II (513−553 K).
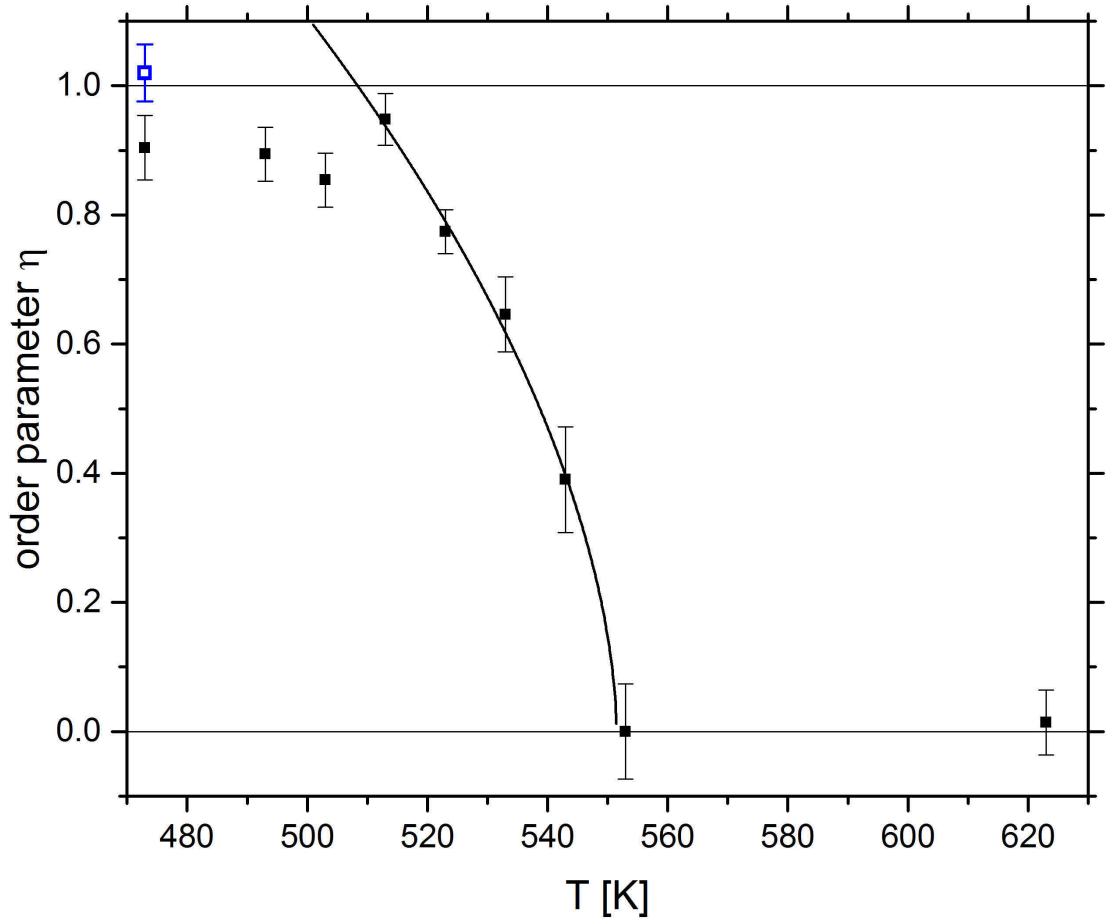
Figure 5.8.: Temperature variation of the order parameter η and fit to Equation 1.3 (open symbol−sample N10). The order-disorder transformation follows a Landau type behavior for a second order transition.
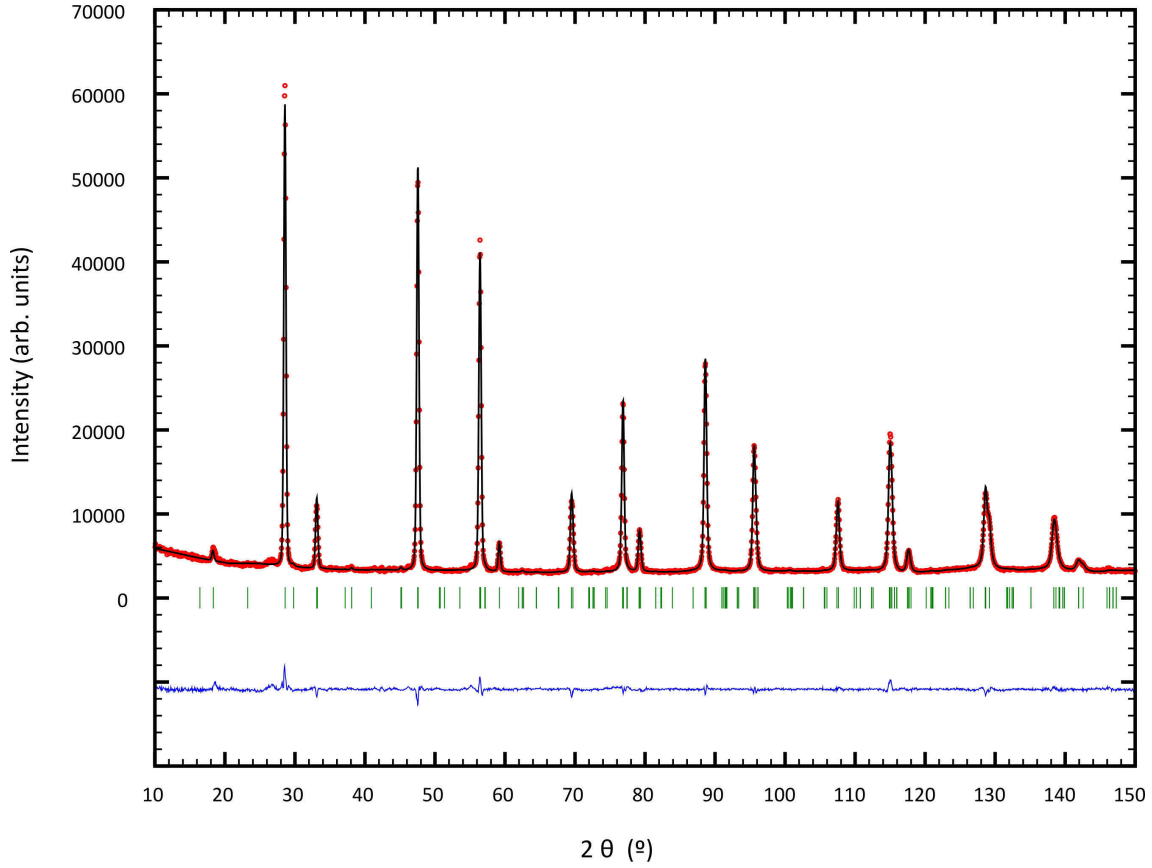
Figure 5.9.: Neutron powder diffraction patterns of samples N10 (473 K) with the results of the Rietveld refinements.

The refined value of the critical exponent β is 0.57 ± 0.06 which is in agreement with a Landau-type behavior for a second order transition ($\beta = 1/2$). The critical temperature T_c for the transformation from ordered to disordered kesterite was determined as $552 \pm 2\,K$. The fitted curve using Equation 1.3 is presented in Figure 5.8.

It is remarkable that a fully ordered kesterite structure ($\eta = 1$ within the standard deviation) was not reached even at the lowest temperatures. Always a slight disorder is found in the samples. This is in agreement with the work of Scragg et al. [6] who claimed that a substantial concentration of disorder will always occur in practical samples. However, the highest value for the order parameter that was realized in his study on thin films was 0.8 for a sample annealed for 600 h (25 d) at 383 K. In our powder samples, a higher ordering could be achieved. The critical temperature determined by our neutron work differs slightly from the one determined by Scragg et al. [17] who published a value of $T_c = 533 \pm 10\,K$. Possible explanations of the difference may be their short annealing times of 1 hour to 24 hours of all their samples except the one described above (600 h) and their use of Zn-rich samples.

Table 5.1.: Lattice parameters and residual values of the Rietveld refinement of sample N10.

Neutron diffraction	
Structure type	kesterite
Crystal system	tetragonal
Space group	$I\bar{4}$ (No.82)
Diffractometer	SPODI
Wavelength	154.82 pm
2θ range	$1-150°$
a / pm	543.336(10)
c / pm	1083.77(2)
R_{Bragg} / %	2.40
R_{wp} / %	2.80
R_{exp} / %	1.68
S	1.66

Table 5.2.: Refined structural parameters of sample N10.

Atom	Wyckoff	x	y	z	Biso	occ
Cu	$2a$	0	0	0	1.3(2)	1.00(3)
Cu	$2c$	0	1/2	1/4	1.8(3)	0.99(3)
Zn	$2d$	0	1/2	3/4	0.5(2)	1.01(3)
Sn	$2b$	0	0	1/2	0.3(2)	1.00(3)
S	$8g$	0.753(4)	0.7589(15)	0.8724(6)	0.728(14)	4

In order to investigate whether equilibrium is reached after an annealing time of 1 week, the sample N10, treated at 473 K, was additionally annealed for two weeks at the same temperature. The results of the Rietveld refinement are depicted in Figure 5.9, Table 5.1, and 5.2. The refinements were carried out using both strategies described above, with similar results. Figure 5.10 (left) represents the experimental average neutron scattering length for the cation positions. The resulting cation distribution on the four sites $2a$, $2b$, $2c$, and $2d$ is depicted in Figure 5.10 (right). As shown in Table 5.2, this sample exhibits a full order (within the standard deviation) of Cu and Zn on their respective positions (for η_I, determined using refinement strategy 2, see Figure 5.8). Consequently, for Cu_2ZnSnS_4 very long annealing times are necessary to reach equilibrium at low temperatures. As a consequence, the above-discussed order parameters at low temperatures may slightly differ from the equilibrium values. This is also supported by the observation that the value at
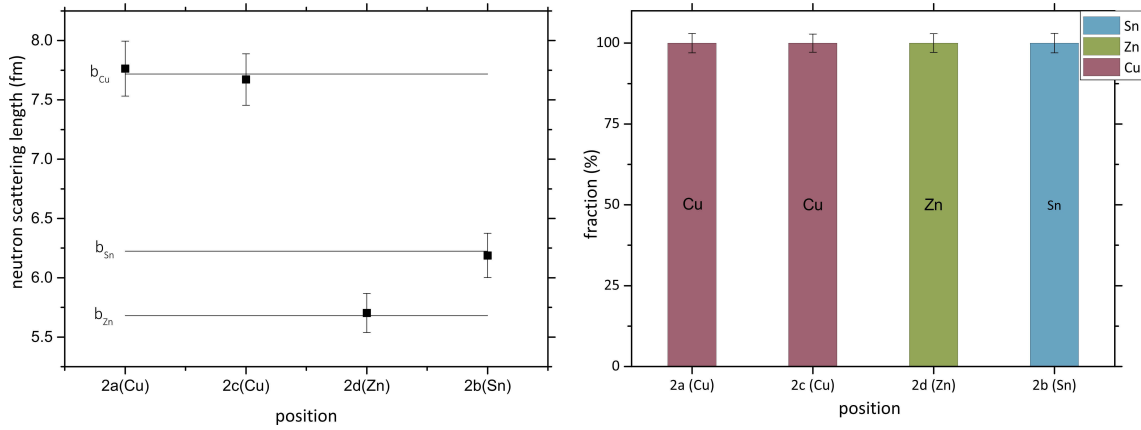
Figure 5.10.: Experimental average neutron scattering length $\bar{b}_i^{exp}$ of the four cation sites of sample N10 (left) and resulting cation distribution (right). Within the standard deviation the sample exhibits a fully ordered kesterite structure.

513 K is larger compared to that of the samples treated at lower temperatures. Looking again at Figure 5.3, the behavior of the superstructure reflection at $2\vartheta = 18.3°$ is easy to understand now. It clearly corresponds to the evolution of the order parameter.

5.5. Conclusions

In this study the order-disorder transition in Cu_2ZnSnS_4 was investigated using neutron diffraction techniques on samples annealed in the range of $473 - 623$ K. A fully ordered (within the standard deviation) sample was prepared with an annealing time of three weeks at 473 K. As it is expected that the degree of order should severely influence the physical properties of Cu_2ZnSnS_4, these investigations offer the possibility for directed preparation of materials with a defined order parameter which are an indispensable prerequisite for a deeper understanding of the correlations between crystal structure and electronic properties.

Acknowledgement

References

[1] S. Chen, X.G. Gong, A. Walsh, S.-H. Wei, *Appl. Phys. Lett.* **2009**, *94*, 041903/1 – 041903/3.

[2] J.J. Scragg, P.J. Dale, L.M. Peter, G. Zoppi, I. Forbes, *Phys. Status Solidi B* **2008**, *245*, 1772 – 1778.

[3] S. Siebentritt, S. Schorr, *Prog. Photovoltaics* **2012**, *20*, 512 – 519.

[4] W. Wang, M.T. Winkler, O. Gunawan, T. Gokmen, T.K. Todorov, Y. Zhu, D.B. Mitzi, *Adv. Energy Mater.* **2014**, *4*, 1301465/1 – 1301465/5.

[5] M. Grossberg, T. Raadik, J. Raudoja, J. Krustok, *Current Applied Physics* **2014**, *14*, 447 – 450.

[6] J.J.S. Scragg, J.K. Larsen, M. Kumar, C. Persson, J. Sendler, S. Siebentritt, C. Platzer Bjoerkman, *Phys. Status Solidi B* **2016**, *253*, 247 – 254 .

[7] S. Schorr, *Sol. Energy Mater. Sol. Cells* **2011**, *95*, 1482–1488.

[8] L. Choubrac, M. Paris, A. Lafond, C. Guillot-Deudon, X. Rocquefelte, S. Jobic, *Phys. Chem. Chem. Phys.* **2013**, *15*, 10722 – 10725.

[9] S. Schorr, M. Tovar, B*ENSC Experimental Report* **2006**.

[10] A. Ritscher, J. Just, O. Dolotko, S. Schorr, M. Lerch, *J. Alloys Compd.* **2016**, *670*, 289 – 296.

[11] S. Schorr, H.-J. Hoebler, M. Tovar, *Eur. J. Mineral.* **2007**, *19*, 65 – 73.

[12] M.Y. Valakh, V.M. Dzhagan, I.S. Babichuk, X. Fontane, A. Perez-Rodriquez, S. Schorr, *JETP Lett.* **2013**, *98*, 255 – 258.

[13] A. Nagoya, R. Asahi, R. Wahl, G. Kresse, *Phys. Rev. B Condens. Matter Mater. Phys.* **2010**, *81,* 113202/1 – 113202/4.

[14] S. Chen, J.-H. Yang, X.G. Gong, A. Walsh, S.-H. Wei, *Phys. Rev. B: Condens. Matter Mater. Phys.* **2010**, *81*, 245204/1 – 245204/10.

[15] M. Paris, L. Choubrac, A. Lafond, C. Guillot-Deudon, S. Jobic, *Inorg. Chem.* **2014**, *53*, 8646 – 8653.

[16] A. Lafond, L. Choubrac, C. Guillot-Deudon, P. Fertey, M. Evain, S. Jobic, Acta Crystallogr., *Sect. B: Struct. Sci., Cryst. Eng. Mater.* **2014**, *70*, 390 – 394.

[17] J.J.S. Scragg, L. Choubrac, A. Lafond, T. Ericson, C. Platzer-Bjoerkman, *Appl. Phys. Lett.* **2014**, *104*, 041911/1 – 041911/4.

[18] S. Schorr, G. Gonzalez-Aviles, *Phys. Status Solidi A* **2009**, *206*, 1054 – 1058.

[19] M. Hoelzel, A. Senyshyn, N. Juenke, H. Boysen, W. Schmahl, H. Fuess, *Nucl. Instrum. Methods Phys. Res., Sect. A* **2012**, *667*, 32 – 37.

[20] H.M. Rietveld, *J. Appl. Crystallogr.* **1969**, *2*, 65 – 71.

[21] J. Rodriguez-Carvajal, *Abstracts of the Satellite Meeting on Powder Diffraction of the XV.Congress of the IUCr* **1990**, 127.

[22] P. Thompson, D.E. Cox, J.B. Hastings, *J. Appl. Crystallogr.* **1987**, *20*, 79 – 83.

[23] A. Lafond, L. Choubrac, C. Guillot-Deudon, P. Deniard, S. Jobic, *Z. Anorg. Allg. Chem.* **2012**, *638*, 2571 – 2577.

[24] L. Choubrac, A. Lafond, C. Guillot-Deudon, Y. Moelo, S. Jobic, *Inorg. Chem.* **2012**, *51*, 3346 – 3348.

[25] L.E. Valle Rios, K. Neldner, G. Gurieva, S. Schorr, *J. Alloys Compd.* **2016**, *657*, 408 – 413.

[26] S. Schorr, C. Stephan, T. Toerndahl, R. Mainz in, Wiley-VCH Verlag GmbH & Co. KGaA, **2011**, 347 – 363.

[27] H. Boysen, F. Frey, M. Lerch, T. Vogt, *Z. Kristallogr.* **1995**, *210*, 328 – 337.

Supplementary Data - Refinements

Neutron powder diffraction patterns of samples N1-N10 with the results of the Rietveld refinements and refined structural parameters.

N1 − 473 K

Table 5.3.: Refined structural parameters of sample N1.

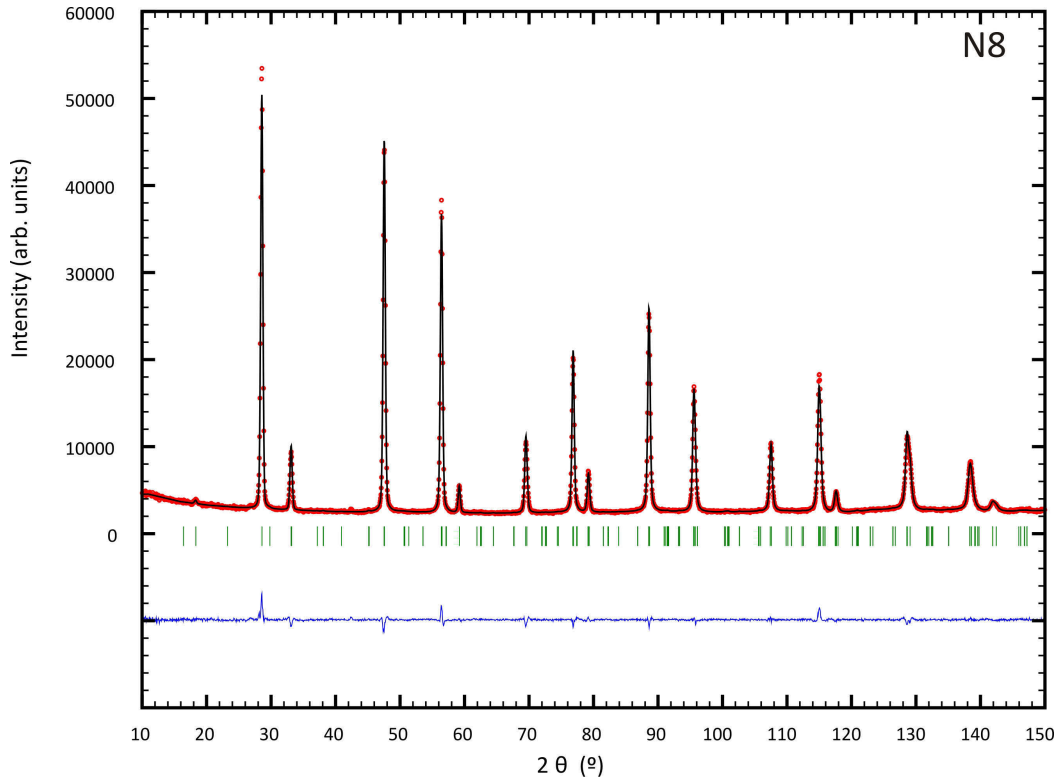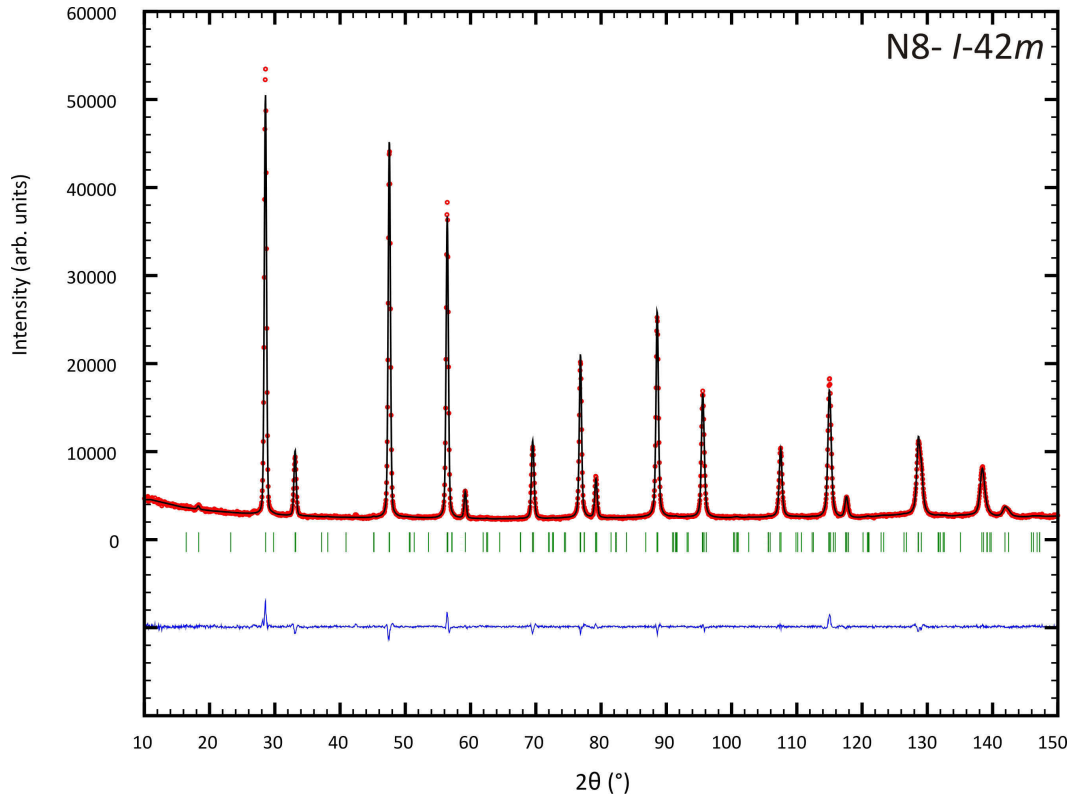| Neutron diffraction		Strategy 2				
Space group		$I\bar{4}$				
a / pm		543.373(9)				
c / pm		1083.92(2)				
R_{Bragg} / %		2.08				
R_{wp} / %		2.21				
R_{exp} / %		1.43				
S		1.54				
Atom	Wyckoff	x	y	z	B_{iso}	occ
Cu	$2a$	0	0	0	1.42(8)	1
Cu	$2c$	0	1/2	1/4	1.91(13)	0.95(3)
Zn	$2c$	0	1/2	1/4	1.91(13)	0.05(3)
Cu	$2d$	0	1/2	3/4	0.67(12)	0.05(3)
Zn	$2d$	0	1/2	3/4	0.67(12)	0.95(3)
Sn	$2b$	0	0	1/2	0.20(7)	1
S	$8g$	0.7584(18)	0.7576(19)	0.8726(6)	0.728(17)	1
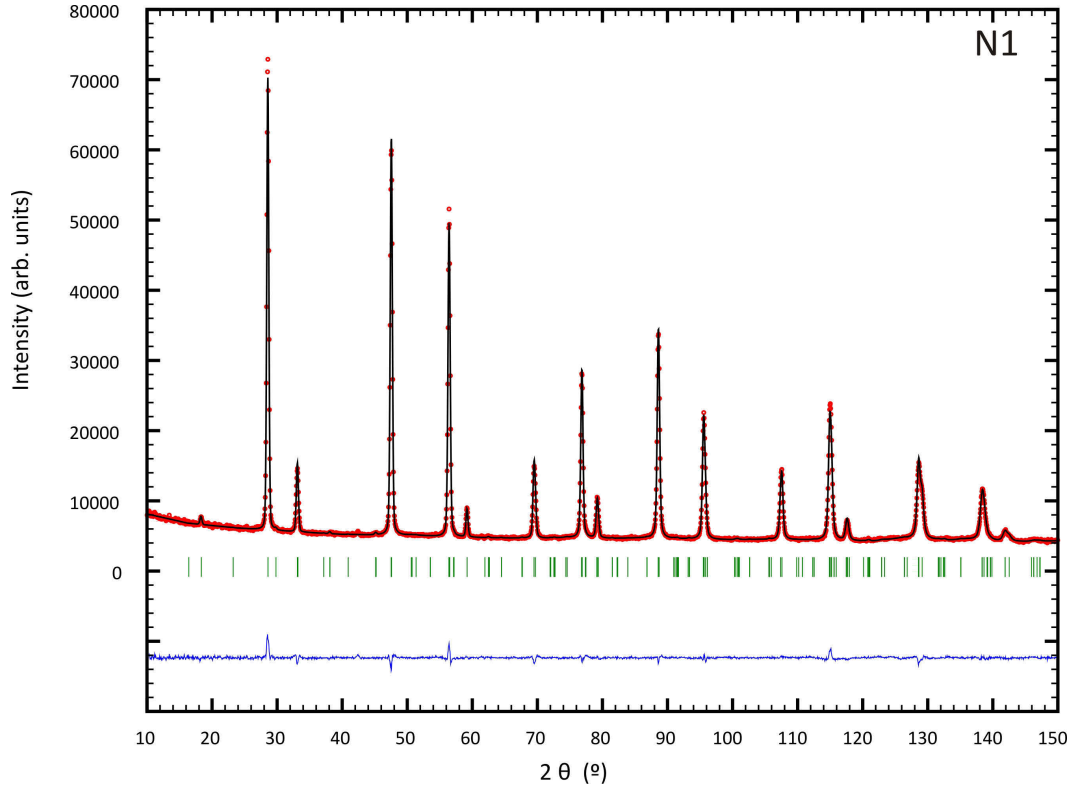
Figure 5.11.: Neutron powder diffraction patterns of samples N1 (473 K) with the results of the Rietveld refinements.

N2 − 493 K

Table 5.4.: Refined structural parameters of sample N2.

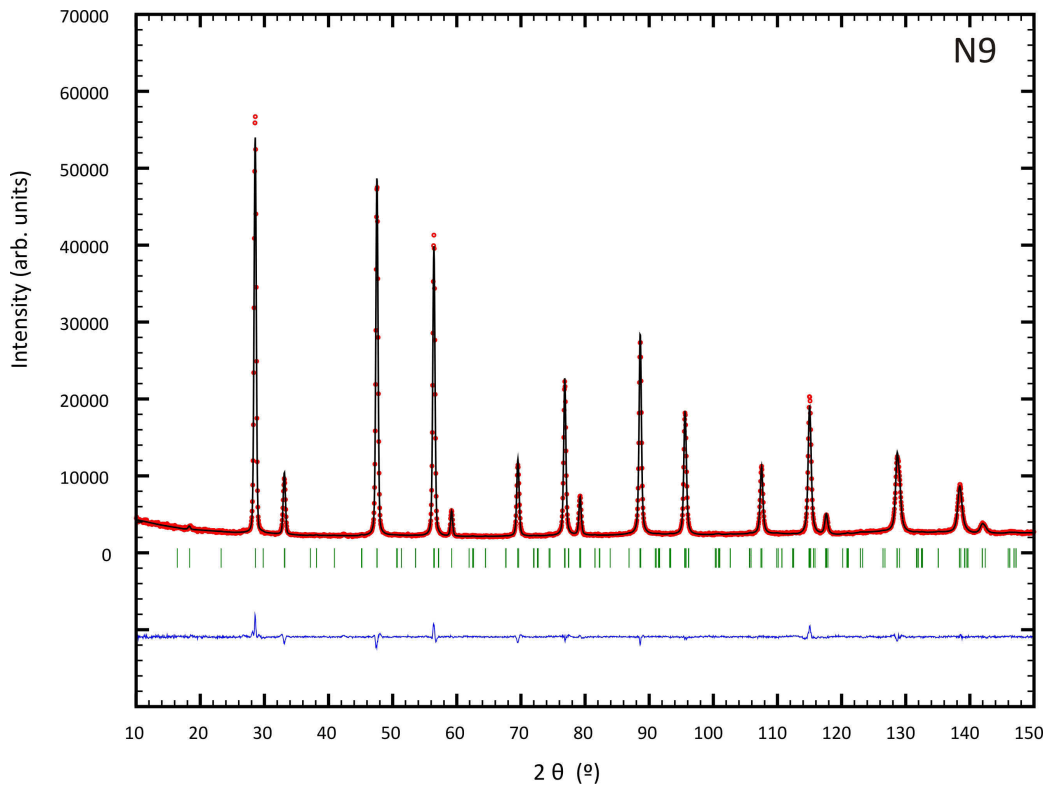| Neutron diffraction		Strategy 2				
Space group		$I\bar{4}$				
a / pm		543.358(9)				
c / pm		1083.83(2)				
R_{Bragg} / %		1.84				
R_{wp} / %		2.40				
R_{exp} / %		1.57				
S		1.53				
Atom	Wyckoff	x	y	z	B_{iso}	occ
Cu	$2a$	0	0	0	1.46(7)	1
Cu	$2c$	0	1/2	1/4	1.89(14)	0.95(2)
Zn	$2c$	0	1/2	1/4	1.89(14)	0.05(2)
Cu	$2d$	0	1/2	3/4	0.75(13)	0.05(2)
Zn	$2d$	0	1/2	3/4	0.75(13)	0.95(2)
Sn	$2b$	0	0	1/2	0.15(5)	1
S	$8g$	0.7567(18)	0.7563(17)	0.8732(8)	0.730(13)	1
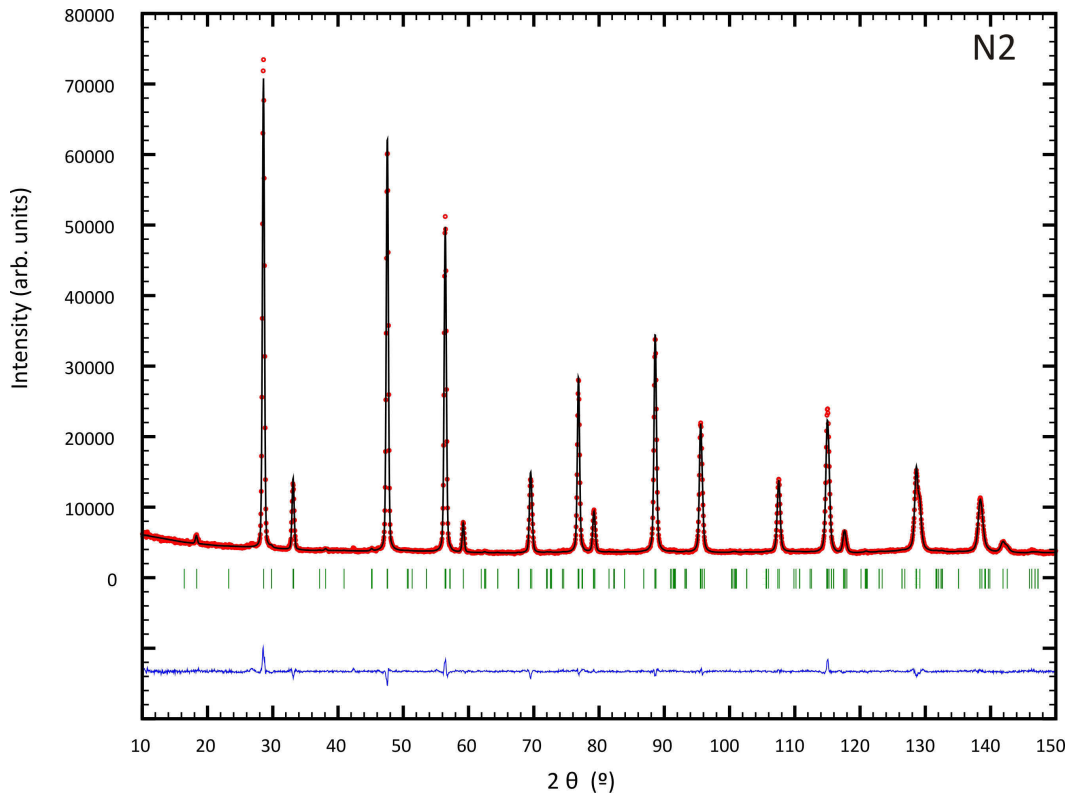
Figure 5.12.: Neutron powder diffraction patterns of samples N2 (493 K) with the results of the Rietveld refinements.

N3 − 503 K

Table 5.5.: Refined structural parameters of sample N3.

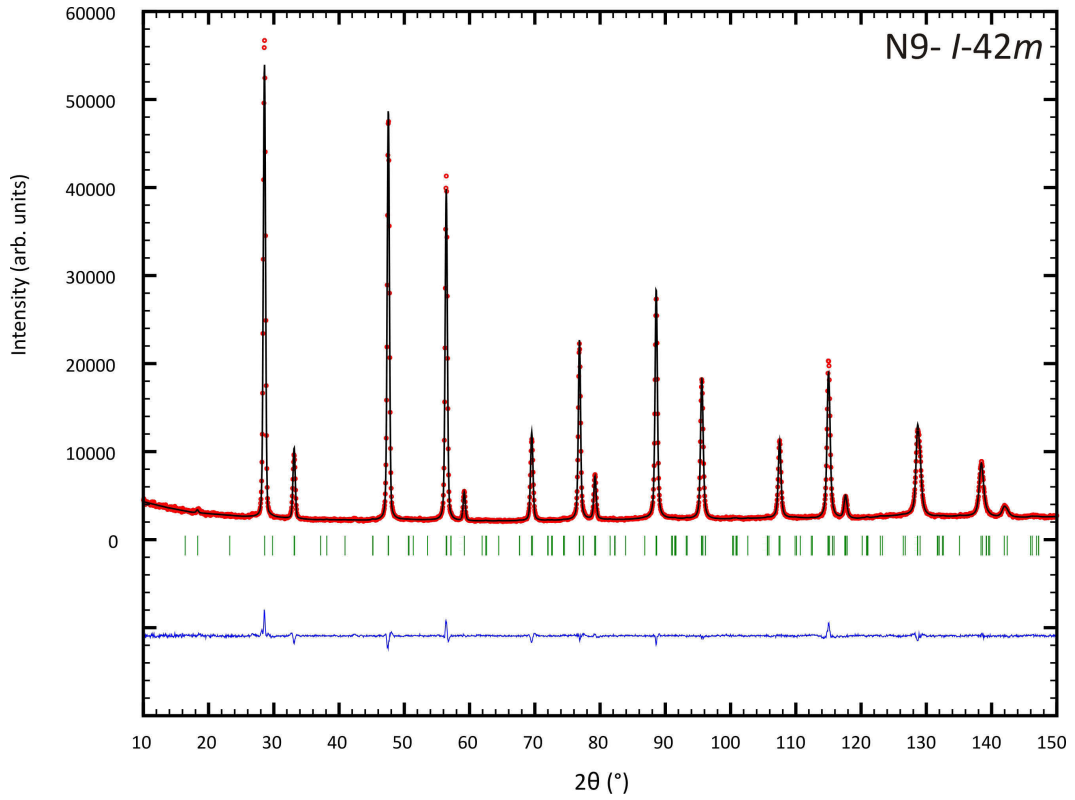| Neutron diffraction			Strategy 2			
Space group			$I\bar{4}$			
a / pm			543.321(8)			
c / pm			1084.17(2)			
R_{Bragg} / %			1.91			
R_{wp} / %			2.55			
R_{exp} / %			1.75			
S			1.46			
Atom	Wyckoff	x	y	z	B_{iso}	occ
Cu	2a	0	0	0	1.54(15)	1
Cu	2c	0	1/2	1/4	2.0(2)	0.93(2)
Zn	2c	0	1/2	1/4	2.0(2)	0.08(2)
Cu	2d	0	1/2	3/4	0.58(19)	0.08(2)
Zn	2d	0	1/2	3/4	0.58(19)	0.93(2)
Sn	2b	0	0	1/2	0.14(12)	1
S	8g	0.753(3)	0.7556(16)	0.8735(7)	0.803(12)	1
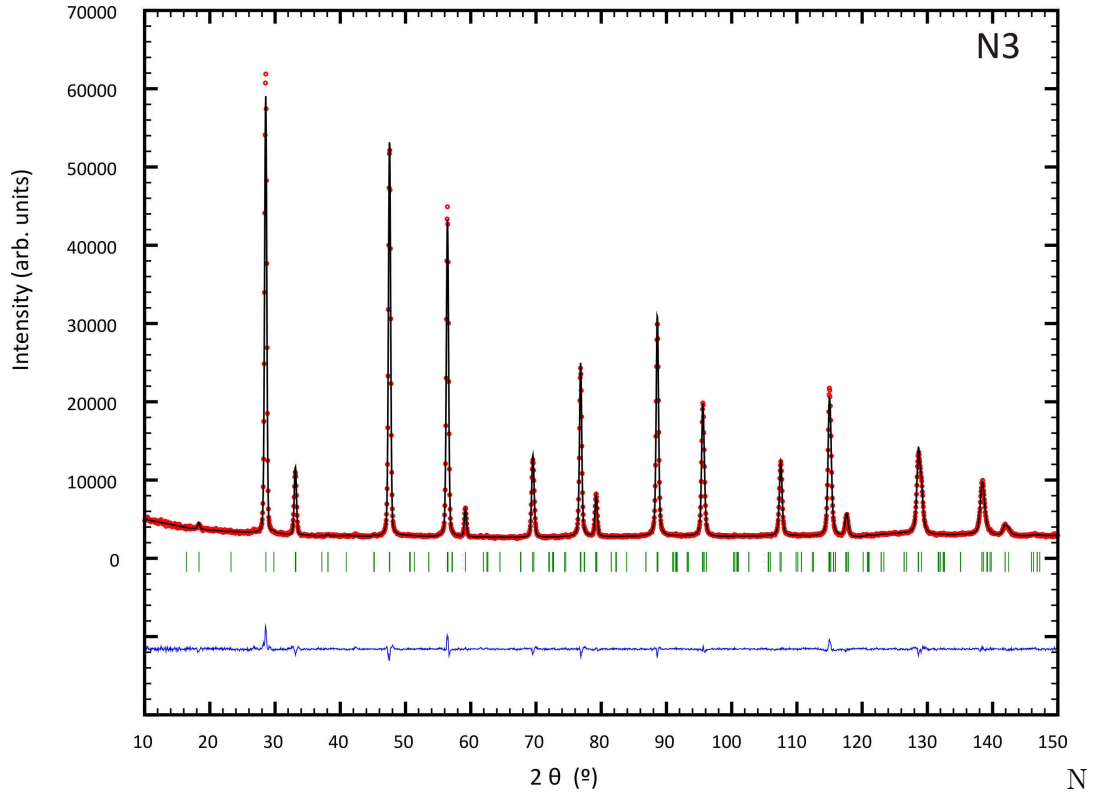
Figure 5.13.: eutron powder diffraction patterns of samples N3 (503 K) with the results of the Rietveld refinements.

N4 − 513 K

Table 5.6.: Refined structural parameters of sample N4.

Neutron diffraction		Strategy 2				
Space group		$I\bar{4}$				
a / pm		543.382(8)				
c / pm		1083.73(2)				
R_{Bragg} / %		1.49				
R_{wp} / %		2.52				
R_{exp} / %		1.72				
S		1.47				
Atom	Wyckoff	x	y	z	B_{iso}	occ
Cu	$2a$	0	0	0	1.43(9)	1
Cu	$2c$	0	1/2	1/4	1.90(12)	0.97(2)
Zn	$2c$	0	1/2	1/4	1.90(12)	0.03(2)
Cu	$2d$	0	1/2	3/4	0.57(12)	0.03(2)
Zn	$2d$	0	1/2	3/4	0.57(12)	0.97(2)
Sn	$2b$	0	0	1/2	0.30(8)	1
S	$8g$	0.757(19)	0.758(15)	0.8740(8)	0.718(12)	1
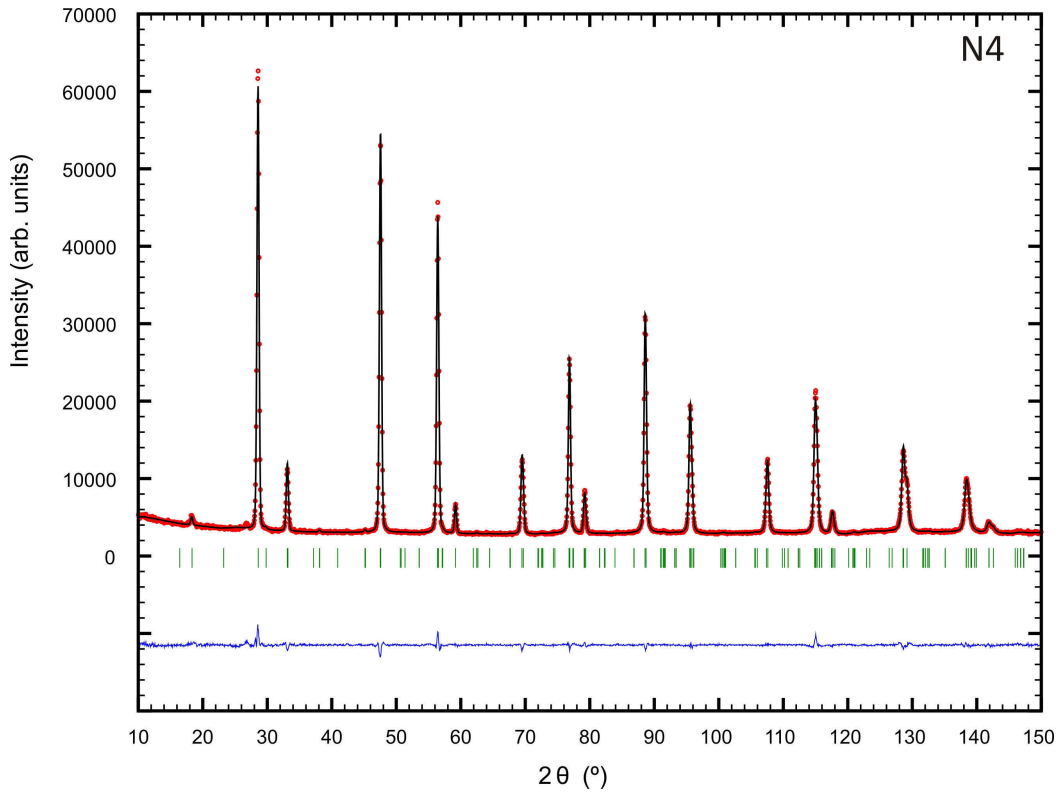
Figure 5.14.: Neutron powder diffraction patterns of samples N4 (513 K) with the results of the Rietveld refinements.

N5 − 523 K

Table 5.7.: Refined structural parameters of sample N5.

Neutron diffraction		Strategy 2				
Space group		$I\bar{4}$				
a / pm		543.260(9)				
c / pm		1084.33(2)				
R_{Bragg} / %		1.86				
R_{wp} / %		2.92				
R_{exp} / %		1.94				
S		1.51				
Atom	Wyckoff	x	y	z	B_{iso}	occ
Cu	2a	0	0	0	1.35(13)	1
Cu	2c	0	1/2	1/4	2.47(7)	0.89(2)
Zn	2c	0	1/2	1/4	2.47(7)	0.11(2)
Cu	2d	0	1/2	3/4	0.38(5)	0.11(2)
Zn	2d	0	1/2	3/4	0.38(5)	0.98(2)
Sn	2b	0	0	1/2	0.34(12)	1
S	8g	0.746(2)	0.754(2)	0.8759(8)	0.852(13)	1
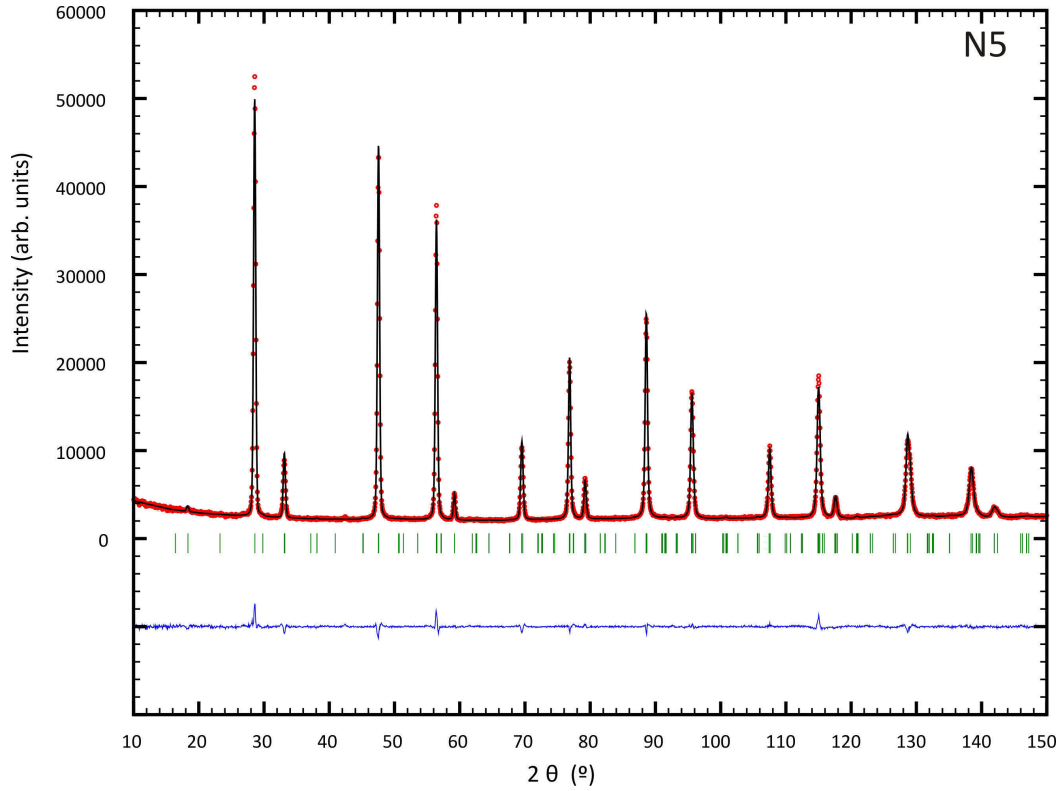
Figure 5.15.: Neutron powder diffraction patterns of samples N5 (523 K) with the results of the Rietveld refinements.

N6 − 533 K

Table 5.8.: Refined structural parameters of sample N6.

Neutron diffraction		Strategy 2				
Space group		$I\bar{4}$				
a / pm		543.355(9)				
c / pm		1083.97(2)				
R_{Bragg} / %		1.77				
R_{wp} / %		2.81				
R_{exp} / %		1.92				
S		1.46				
Atom	Wyckoff	x	y	z	B_{iso}	occ
Cu	$2a$	0	0	0	1.46(6)	1
Cu	$2c$	0	1/2	1/4	1.54(10)	0.82(3)
Zn	$2c$	0	1/2	1/4	1.54(10)	0.18(3)
Cu	$2d$	0	1/2	3/4	1.05(10)	0.18(3)
Zn	$2d$	0	1/2	3/4	1.05(10)	0.82(3)
Sn	$2b$	0	0	1/2	0.22(4)	1
S	$8g$	0.7599(11)	0.7551(19)	0.8742(9)	0.720(12)	1
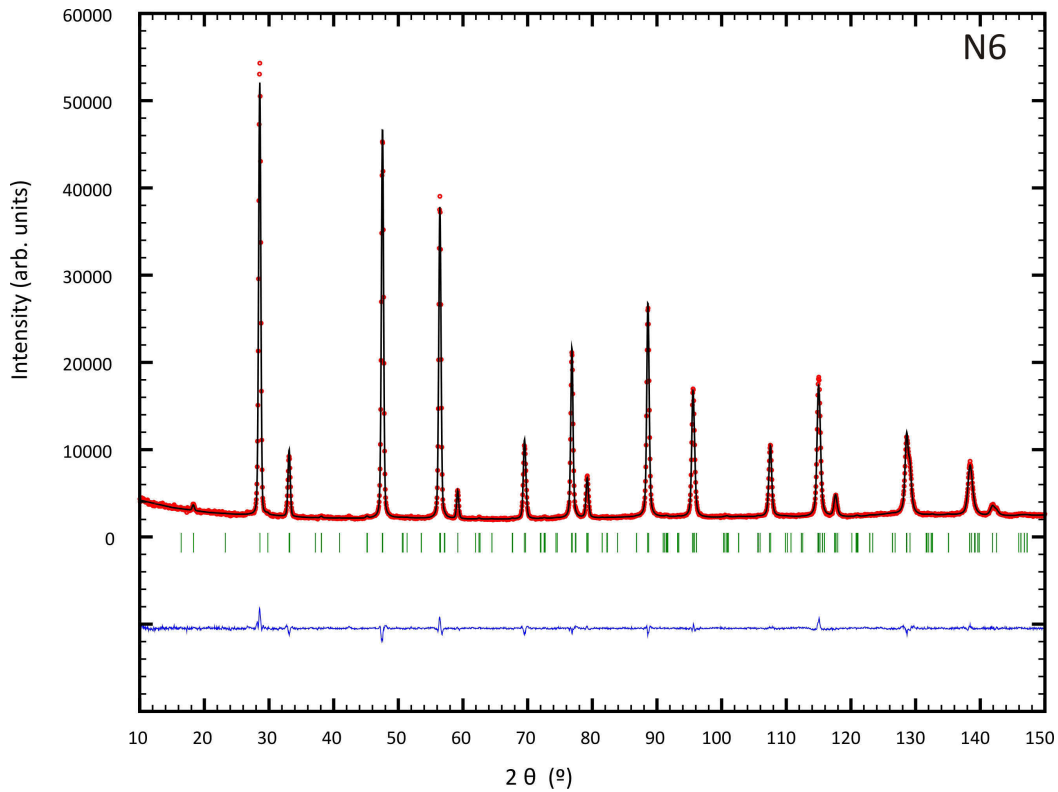
Figure 5.16.: Neutron powder diffraction patterns of samples N6 (533 K) with the results of the Rietveld refinements.

N7 – 543 K

Table 5.9.: Refined structural parameters of sample N7.

Neutron diffraction		Strategy 2				
Space group		$I\bar{4}$				
a / pm		543.270(8)				
c / pm		1084.47(2)				
R_{Bragg} / %		1.83				
R_{wp} / %		2.71				
R_{exp} / %		1.82				
S		1.49				
Atom	Wyckoff	x	y	z	B_{iso}	occ
Cu	$2a$	0	0	0	1.39(12)	1
Cu	$2c$	0	1/2	1/4	2.03(10)	0.70(4)
Zn	$2c$	0	1/2	1/4	2.03(10)	0.31(4)
Cu	$2d$	0	1/2	3/4	0.75(8)	0.31(4)
Zn	$2d$	0	1/2	3/4	0.75(8)	0.70(4)
Sn	$2b$	0	0	1/2	0.21(10)	1
S	$8g$	0.747(3)	0.7557(16)	0.8741(8)	0.811(12)	1
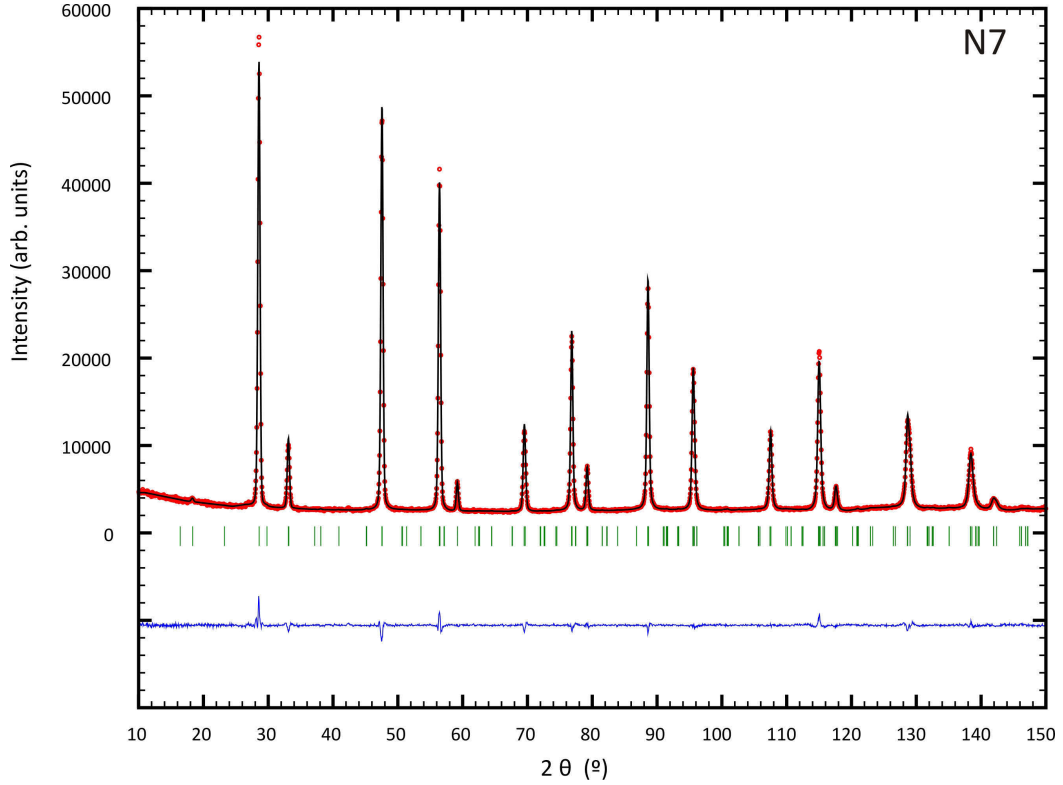
Figure 5.17.: Neutron powder diffraction patterns of samples N7 (543 K) with the results of the Rietveld refinements.

N8 − 553 K

Table 5.10.: Refined structural parameters of sample N8 (space group $I\bar{4}$).

Neutron diffraction		Strategy 2				
Space group		$I\bar{4}$				
a / pm		543.339(9)				
c / pm		1084.20(2)				
R_{Bragg} / %		2.36				
R_{wp} / %		2.80				
R_{exp} / %		1.86				
S		1.51				
Atom	Wyckoff	x	y	z	B_{iso}	occ
Cu	$2a$	0	0	0	1.49(10)	1
Cu	$2c$	0	1/2	1/4	1.5(2)	0.50(3)
Zn	$2c$	0	1/2	1/4	1.5(2)	0.50(3)
Cu	$2d$	0	1/2	3/4	1.10(18)	0.50(3)
Zn	$2d$	0	1/2	3/4	1.10(18)	0.50(3)
Sn	$2b$	0	0	1/2	0.15(8)	1
S	$8g$	0.752(4)	0.7586(14)	0.8740(9)	0.799(13)	1

Figure 5.18.: Neutron powder diffraction patterns of samples N8 (553 K) with the results of the Rietveld refinements.

Table 5.11.: Refined structural parameters of sample N8 (space group $I\bar{4}2m$)

Neutron diffraction		$I4\bar{2}m$				
Space group		$I4\bar{2}m$				
a / pm		543.344(9)				
c / pm		1084.21 (2)				
R_{Bragg} / %		2.33				
R_{wp} / %		2.79				
R_{exp} / %		1.86				
S		1.50				
Atom	Wyckoff	x	y	z	B_{iso}	occ
Cu	$2a$	0	0	0	2.17(8)	0.994(11)
Cu	$4d$	0	1/2	1/4	0.72(3)	0.502(4)
Zn	$4d$	0	1/2	1/4	0.72(3)	0.502(4)
Sn	$2b$	0	0	1/2	0.71(7)	1.003(13)
S	$8i$	0.7566(6)	0.7566(6)	0.8760(10)	0.79(2)	1

Figure 5.19.: Neutron powder diffraction patterns of samples N8 (553 K) with the results of the Rietveld refinements.

N9 – 643 K

Table 5.12.: Refined structural parameters of sample N9 (space group $I\bar{4}$)

Neutron diffraction		Strategy 2				
Space group		$I\bar{4}$				
a / pm		543.256(9)				
c / pm		1084.46 (2)				
R_{Bragg} / %		2.14				
R_{wp} / %		2.85				
R_{exp} / %		1.88				
S		1.52				
Atom	Wyckoff	x	y	z	B_{iso}	occ
Cu	*2a*	0	0	0	1.49(9)	1
Cu	*2c*	0	1/2	1/4	1.5(2)	0.51(3)
Zn	*2c*	0	1/2	1/4	1.5(2)	0.50(3)
Cu	*2d*	0	1/2	3/4	1.2(2)	0.50(3)
Zn	*2d*	0	1/2	3/4	1.2(2)	0.51(3)
Sn	*2b*	0	0	1/2	0.16(7)	1
S	*8g*	0.752(4)	0.7583(12)	0.8741(8)	0.779(12)	1

Figure 5.20.: Neutron powder diffraction patterns of samples N9 (643 K) with the results of the Rietveld refinements.

Table 5.13.: Refined structural parameters of sample N9 (space group $I\bar{4}2m$)

Neutron diffraction		$I4\bar{2}m$				
Space group		$I4\bar{2}m$				
a / pm		543.259(9)				
c / pm		1084.45(2)				
R_{Bragg} / %		2.16				
R_{wp} / %		2.84				
R_{exp} / %		1.88				
S		1.51				
Atom	Wyckoff	x	y	z	B_{iso}	occ
Cu	$2a$	0	0	0	1.39(6)	0.979(10)
Cu	$4d$	0	1/2	1/4	1.42(3)	0.505(4)
Zn	$4d$	0	1/2	1/4	1.42(3)	0.505(4)
Sn	$2b$	0	0	1/2	0.25(4)	1.009(9)
S	$8i$	0.7560(5)	0.7560(5)	0.8737(9)	0.770(12)	1

Figure 5.21.: Neutron powder diffraction patterns of samples N9 (643 K) with the results of the Rietveld refinements.

N10 − 473 K

Table 5.14.: Refined structural parameters of sample N10

Neutron diffraction		Strategy 2				
Space group		$I\bar{4}$				
a / pm		543.341(10)				
c / pm		1083.76(2)				
R_{Bragg} / %		2.35				
R_{wp} / %		2.877				
R_{exp} / %		1.68				
S		1.65				
Atom	Wyckoff	x	y	z	B_{iso}	occ
Cu	2a	0	0	0	1.3(4)	1
Cu	2c	0	1/2	1/4	2.0(4)	1.01(2)
Zn	2c	0	1/2	1/4	2.0(4)	0.00(2)
Cu	2d	0	1/2	3/4	0.5(3)	0.00(2)
Zn	2d	0	1/2	3/4	0.5(3)	1.01(2)
Sn	2b	0	0	1/2	0.3(4)	1
S	8g	0.750(8)	0.7588(7)	0.8738(9)	0.771(14)	1
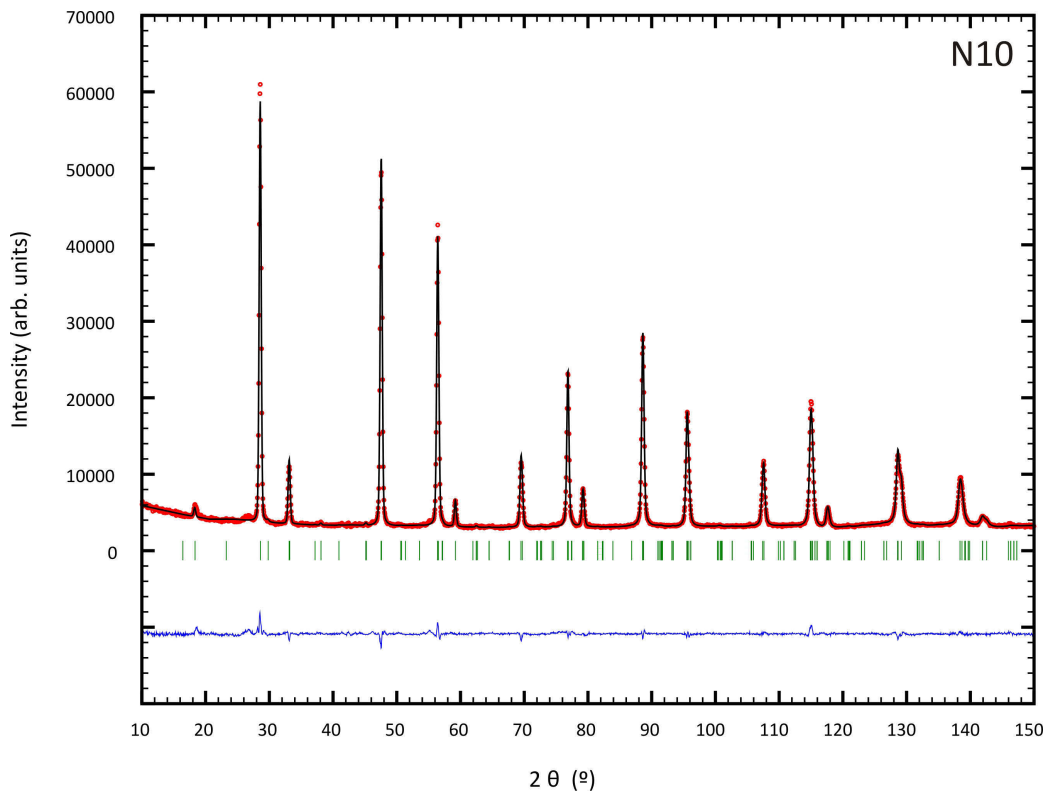
Figure 5.22.: Neutron powder diffraction patterns of samples N9 (643 K) with the results of the Rietveld refinements.

6. Publication 3

Study of the mechanochemical process to crystalline Cu$_2$ZnSnS$_4$ powder

Anna Ritscher, Marc Schlosser, Arno Pfitzner, Martin Lerch

Contribution to publication:

A. Ritscher: Sample preparation, analysis and evaluation, writing.

M. Schlosser: Measurements (high temperature diffraction).

A. Pfitzner   Proofreading.

M. Lerch: General advice and helpful comments, proofreading.

Overall contribution of A. Ritscher to the publication: 75 %

Authors   A. Ritscher [1,2], M. Schlosser [3], A. Pfitzner [3], M. Lerch *[1]

[1] Institut für Chemie, Technische Universität Berlin, Straße des 17.Juni 115, 10623 Berlin, Germany

[2] Helmholtz-Zentrum Berlin für Materialien und Energie, Hahn-Meitner-Platz 1, 14109 Berlin, Germany

[3] Institut für Anorganische Chemie, Universität Regensburg, Universitätsstr. 31, 93040 Regensburg, Germany

   * corresponding author

6.1. Abstract

Kesterite-type Cu_2ZnSnS_4 was synthesized from the corresponding binary sulfides by a mechanochemical route in a planetary ball mill. The reaction progress during this milling step was followed within a time range of $10-180$ minutes by powder X-ray diffraction. In addition, the crystallization of the milled material was studied *in situ* by high-temperature X-ray powder methods in a temperature range of $300-500$ °C. Significant disorder (cation distribution) was observed at 500 °C, strongly decreasing during cooling down to ambient temperature with a rate of 60 K/h.

6.2. Introduction

Systematic analysis of the semiconductor compound Cu_2ZnSnS_4 (CZTS) and its structural, chemical, and physical properties have been in the focus of interest in the last few years [1-6]. This quaternary chalcogenide shows a great potential as absorber material for applications in thin film photovoltaics. Owing to its suitable properties (optical band gap energy $=1.5$ eV, absorption coefficient in the order of 10^{-4} cm^{-1} [7-9]) this material could be a promising low-cost alternative to In-containing $CuIn_xGa_{(1-x)}Se_2$ (CIGS). The current record efficiency of 12.6 % was reached for CZTS-based devices containing additional selenium [10].

After some controversies about the correct crystal structure of Cu_2ZnSnS_4 it was demonstrated in different studies that this quaternary sulfide adopts the kesterite type (space group $I\bar{4}$) [11, 12]. This tetragonal crystal structure derives from the sphalerite type (known for ZnS etc.) by doubling the c-axis and it consists of alternating cation layers stacked along this axis (see Figure 6.1).

The lattice planes at $z=0$ and $z=1/2$ are occupied by Cu/Sn while Cu is found on Wyckoff position $2a$ $(0,0,0)$ and Sn on position $2b$ $(0,0,1/2)$. Remaining Cu/Zn is located on lattice planes at $z=1/4$ and $z=3/4$, position $2c$ $(0,1/2,1/4)$ and $2d$ $(0,1/2,3/4)$, respectively. *Ab initio* calculations [13, 14] showed that, due to its very low formation energy, the point defect complex $(Cu_{Zn} + Zn_{Cu})$ is easily formed and thus Cu/Zn disorder has to be expected. This was also confirmed by diffraction studies on CZTS powder samples, where partial [15, 16] or complete disorder [1] of Cu and Zn on the $2c$ and $2d$ positions was reported.

High temperature X-ray diffraction measurements of kesterite powder using synchrotron radiation show that Cu_2ZnSnS_4 undergoes a structural phase transitions from the tetragonal kesterite- to the cubic sphalerite-type structure at temperatures above of 866 °C [2]. The transition leads to a random distribution of the cations Cu, Zn, and Sn (space group $F\bar{4}3m$). Due to the formation of secondary phases it is challenging to prepare phase-pure
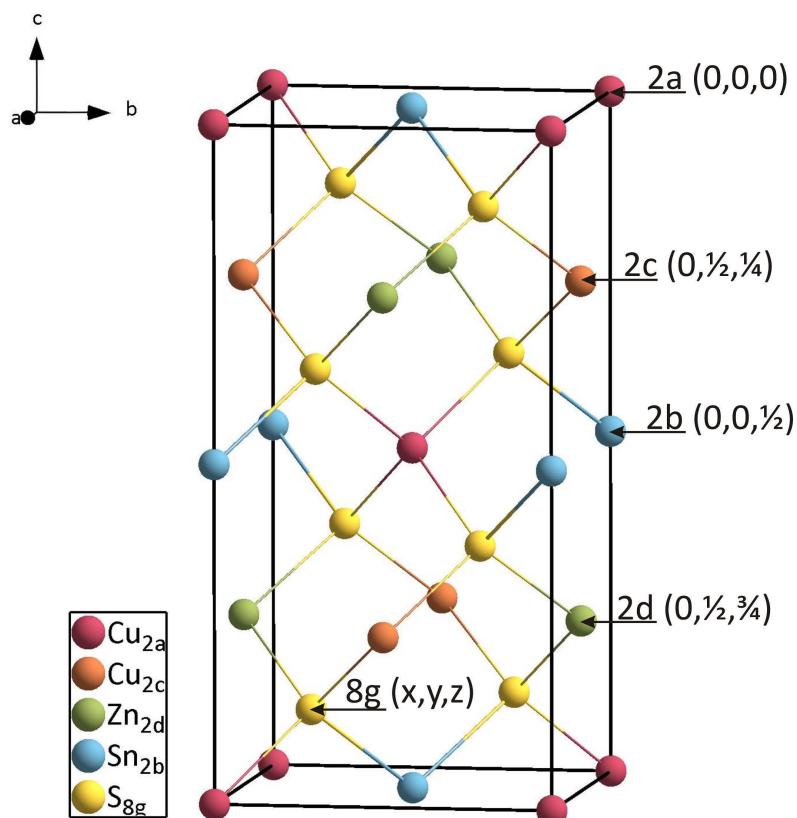
Figure 6.1.: Unit cells of fully ordered kesterite, all Wyckoff positions of the structure are labeled.

CZTS powder, which is important for detailed studies concerning the correlations between structural and electronic properties. Bulk material of CZTS has been usually produced by solid state reaction of the elements in evacuated silica ampoules [1, 17]. Due to the high sulfur vapor pressure it is necessary to apply a defined temperature program and homogenization is obtained by a second annealing step at 750 °C. All these factors result in long reaction times and an enhanced possibility for the formation of secondary phases.

Recently, we presented an easy and fast process for the preparation of single phase CZTS powders [16]. The main idea was the development of a synthesis route at temperatures lower than 750 °C. This was realized by a mechanochemical approach and the synthesis of a precursor by reaction of the corresponding binary sulfides CuS, ZnS, and SnS in a planetary ball mill. Mechanochemical processes in planetary ball mills find a widespread use in science and industry due to the feasibility of rapid, highly efficient, and usually solvent-free chemical synthesis. Additionally, it is possible to develop compounds that cannot be obtained via a conventional solid-state route [18]. After annealing at 500 °C

in H_2S atmosphere a highly crystalline product is achieved. A similar mechanochemical process was reported in Ref. [19], where Cu_2ZnSnX_4 (X = S, Se) bulk material was prepared in a ball mill starting from the metals and the chalcogens.

In this contribution we present a more detailed study of our new developed two step synthesis process. The reaction process in the ball mill as function of time as well as the crystallization behavior of the poorly crystalline CZTS precursor to the crystalline powder with temperature are investigated.

6.3. Experimental

Sulfide powders with the chemical formula Cu_2ZnSnS_4 were prepared by our mechanical process [16]. CuS, ZnS, and SnS were mixed in a molar ratio of 2:1:1 without any additional fluid medium and filled into an 80 ml agate jar (including 5 grinding balls with a diameter of 20 mm). Milling was performed in a Fritsch Planetary Mono Mill PULVERISETTE 6 using a rotational speed of 400 rpm and milling times of up to 180 min. Small amounts of the sample were withdrawn at time intervals of 10 – 30 min for diffraction analyses.

In order to get a highly crystalline product as reference, one half of the as-milled powder (milling time 180 min) was annealed in a conventional tube furnace equipped with a SiO_2-tube in H_2S-atmosphere for 3 h at 500 °C. After this treatment the sample was cooled down with a rate of 60 K/h. X-ray powder diffraction was used for the structural characterization of all samples. Diffraction data were collected using a Panalytical X'Per PRO diffractometer (Bragg-Brentano geometry, Cu-K_α radiation). Structural refinements were performed by the Rietveld method [20] with the program package FULLPROF Suite Version 2015 [21] by applying a pseudo-Voigt function. The kesterite-type structure (space group $I\bar{4}$) was used as starting model for the refinement.

The second half of the sample was used for the investigation of the crystallization behavior of the quaternary sulfide precursor by *in situ* high-temperature X-ray diffraction with the help of a STOE STADI P diffractometer (Transmission/Debye Scherrer geometry, Mo-K_α radiation). The instrument was equipped with a STOE furnace using a Ni/CrNi thermocouple. The sample was encapsulated in an evacuated silica capillary and initially measured at room temperature (RT, measurement number 001). Then the sample was heated to 300 °C with a rate of 50 K/min and subsequently measured at 300 °C every 10 minutes in order to follow the isothermal phase formation and growth of the crystallites (20 measurements, 1 min., measurement numbers N = 002 – 021). Afterwards, the temperature was raised to 400 °C and the powder was again measured every 10 min (measurement numbers N = 022 – 042). A further heating step up to a temperature of 500 °C was applied (measurement numbers N = 043 – 062). Again, diffraction pattern were recorded every 10 min. As a reference measurement a diffraction pattern of the empty furnace without

any sample was recorded in order to detect the signals from the furnace (measurement number N = 000).

6.4. Results and discussion

As described in the experimental section, the first synthesis step to phase pure Cu_2ZnSnS_4 powder is the reaction of the corresponding binary sulfides (CuS, ZnS, SnS) in a ball mill. In order to follow this reaction process, small amounts of powder were withdrawn from the grinding bowl by interrupting the milling procedure several times.Figure 6.2 depicts the XRD patterns of the prepared CZTS powders milled for 10 – 180 min.
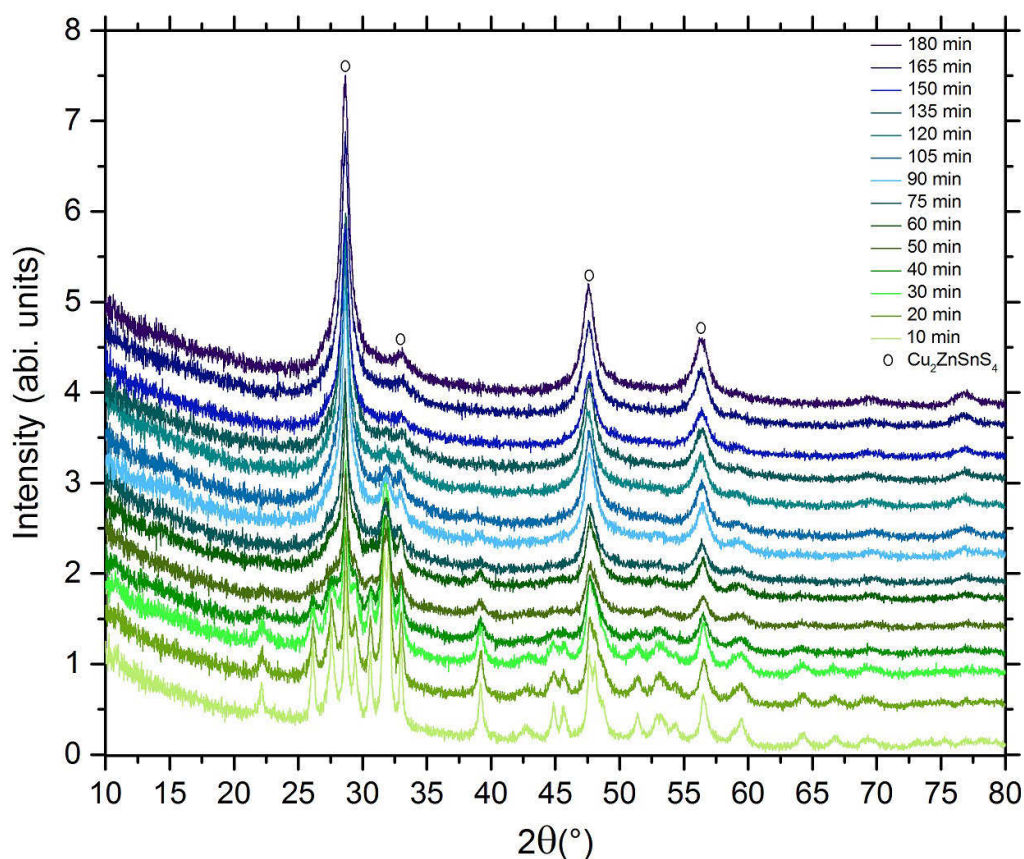
Figure 6.2.: Diffraction patterns (Cu-Kα radiation) of as-prepared samples after the milling process at different times (t = 10 – 180 min.) .

Up to a milling time of 30 minutes the reflections originating from the binary sulfides are the main signals in the diffraction patterns. During this early stage of milling, the powders of CuS, ZnS, and SnS are mixed together and no reaction takes place. After 40 minutes of milling the intensities of the reflections that can be assigned to the binary compounds begin to decrease, which indicates that the solid-state reaction is activated and the product starts
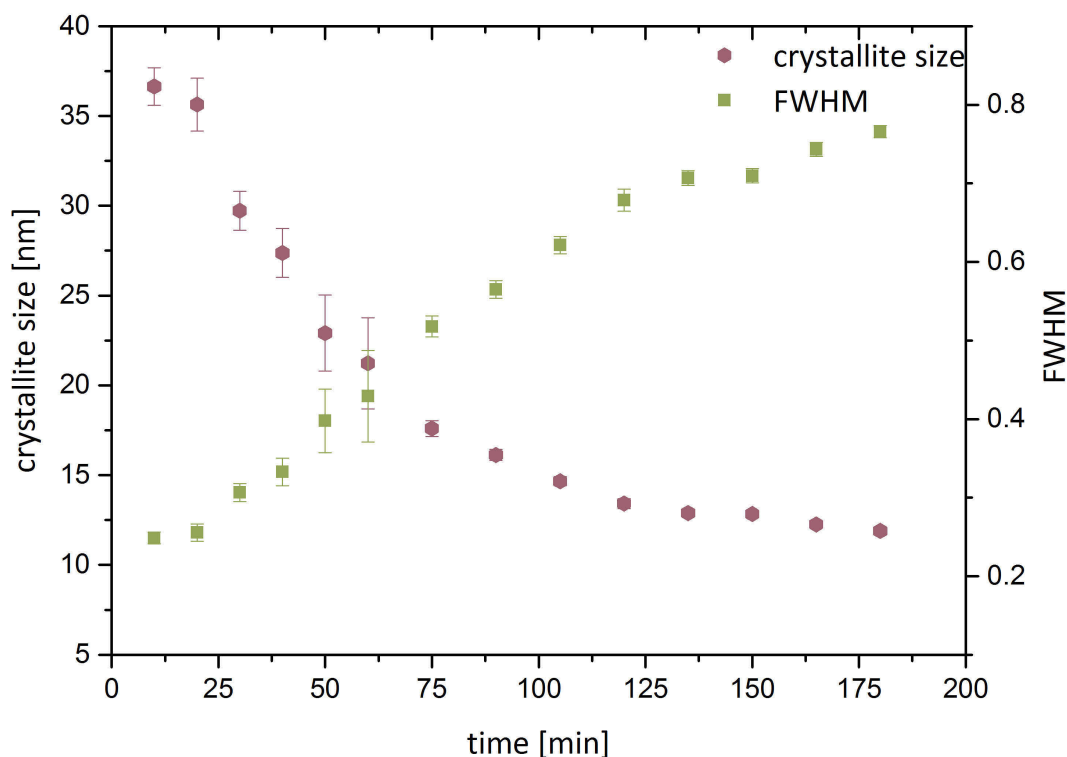
Figure 6.3.: FWHM parameters and corresponding crystalline sizes during reaction in the ball mill

to form, and after 150 minutes it is clearly seen that the signals have disappeared. The sample was further treated up to a total milling time of 180 min. However, the diffraction pattern did not change significantly, thus at this stage the reaction is considered to be terminated. Taking a look at the change of the reflection position of the major reflection a clear trend to lower 2theta values is visible ($2\vartheta = 28.68 \rightarrow 28.62$), which is an indication that the quaternary compound is formed during the reaction in the ball mill. The observed reflection positions of the final as-milled powder correspond to the strongest ones expected for the quaternary compound. However, from the obtained X-ray diffraction patterns it is not possible to extract unequivocal information concerning the distribution of the cations as the main reflections of the kesterite phase (partially or fully ordered) practically have the same positions as the expected ones for a sphalerite-type structure (fully disordered) with the same chemical composition. The superlattice reflections for the kesterite-type phase are rather small (see Figure 6.4), but their total absence points to severe disorder in the milled material. For more unambiguous results additional investigations, for example by EXAFS, would be necessary.

In addition, as it can be clearly seen in Figure 6.2 the milling process results in very broad reflections. Increasing the milling time the FWHM values increase as shown in

Figure 6.4. Profile analyses revealed a dominant Lorentzian shape which can be attributed to crystallite size broadening. The crystallite sizes of the precursor powders are calculated using the Scherrer equation (Equation 1.1) from the strong 112-reflection at $2\vartheta \tilde{} 28.6°$ [22]

$$\triangle(2\theta) = \frac{K\lambda}{Lcos\theta_0} \tag{6.1}$$

where $\Delta(2\vartheta)$ is the line broadening at half the maximum intensity (FWHM), K is the Scherrer-form factor, in this study a factor of 1 was used, λ is the wavelength, L the mean size of the crystallite, and ϑ_0 the diffraction angle. $\Delta(2\vartheta)$ has to be corrected for reflex broadening coming from the instrument according to $\triangle(2\theta) = (\beta_M^2 - \beta_I^2)^{\frac{1}{2}}$ (β_M is measured FWHM and β_I is the correction factor for instrument broadening).

As depicted in Figure 6.3, the particle size after 10 minutes of milling is calculated to 37 nm. In the first 90 minutes the crystallite size decreases rapidly, approaching a value of about 15 nm. On further milling the crystallite size slightly changes reaching a size of $\tilde{} 11$ nm after 180 min. In order to confirm the calculated value, TEM measurements were carried out with this sample. The observed crystallite sizes were found to be in a range of $8 - 13$ nm which is in good agreement with the result of the Scherrer method (~ 11 nm).

In order to prepare a highly crystalline reference sample, one half of the precursor powder was annealed in a tube furnace (H_2S atmosphere) according to the second step of our mechanochemical process [16]. The structural parameters of the annealed sample were refined with the Rietveld method (see Tables 6.1 and 6.2).

Table 6.1.: Lattice parameters of CZTS and residual values of the Rietveld refinement

	Neutron diffraction
Structure type	kesterite
Crystal system	tetragonal
Space group	$I\bar{4}$ (No.82)
Diffractometer	Panalytical X'Pert PRO
Wavelength	154.06 pm, 154.44 pm
2ϑ range	$10 - 120°$
a / pm	543.347(13)
c / pm	1083.72(3)
R_{Bragg} / %	3.84
R_{wp} / %	2.44
R_{exp} / %	2.02
S	1.20

As it was shown in our recent studies, it is nicely possible to control the composition of the synthesized powder with the mechanochemical method [16, 22]. Therefore, for the structural refinement the ideal composition Cu_2ZnSnS_4 was used. The X-ray powder diagram with the results of the Rietveld refinement is depicted in Figure 6.4.

It should be mentioned that it is not possible to differentiate between Zn and Cu using conventional X-ray powder diffraction methods. Consequently, we can only distinguish between Cu/Zn and Sn. Unfortunately, the amount of prepared material was not sufficient for neutron diffraction experiments. For the refinements, the following side conditions were set: the sum of Cu/Zn on all positions must be 3, the sum of Sn on all positions must be 1, and all four cation positions have to be fully occupied.

Table 6.2 lists the final atomic and additional structural parameters. As expected, Sn was found on Wyckoff position $2b$ $(0, 0, 1/2)$, whereas Cu/Zn is located on $2a$ $(0, 0, 0)$, $2c$ $(0, 1/2, 1/4)$, and $2d$ $(0, 1/2, 3/4)$ sites. No Sn is found on position $2c$. On $2a$ and $2d$ sites very small amounts of Sn (around 1%) are found. Missing Sn on the $2b$ site is replaced by Cu/Zn. These results are in agreement with our recent refinements [16].
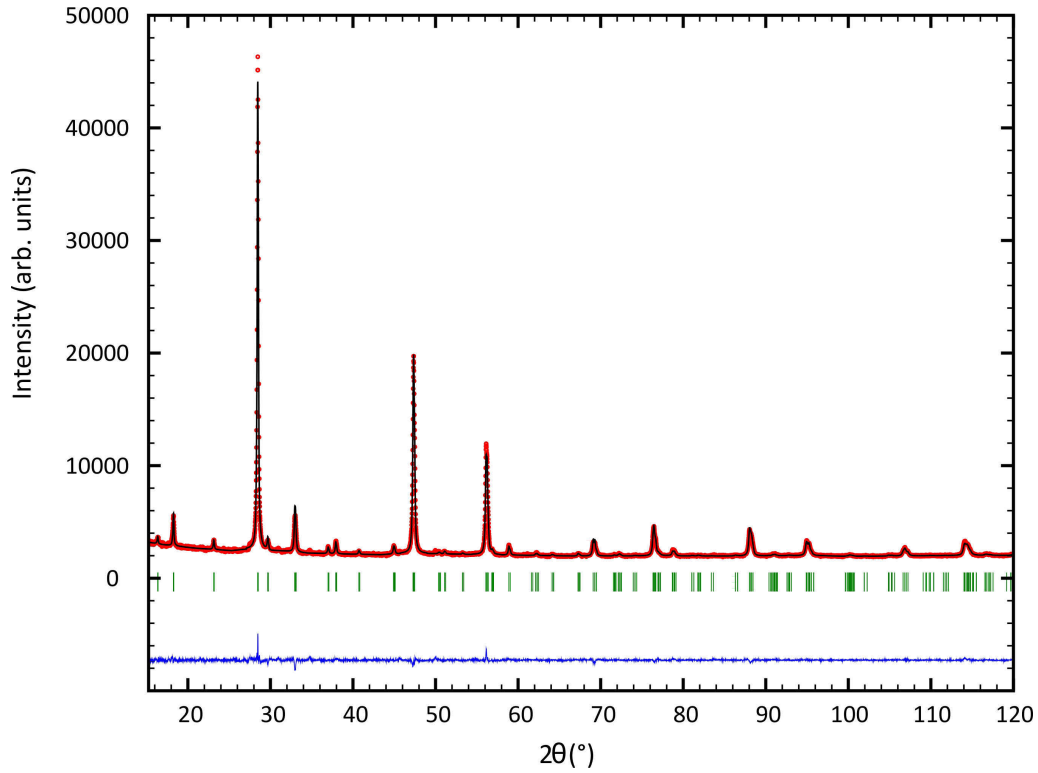
Figure 6.4.: X-ray powder diffraction pattern with the results of the Rietveld refinement using the kesterite-type structure as starting model.

Table 6.2.: Refined structural parameters for CZTS from X-ray diffraction

Atom	Wyckoff	x	y	z	Biso	occ
Cu/Zn	$2a$	0	0	0	1.88(7)	0.995(2)
Sn	$2a$	0	0	0	1.88(7)	0.005(2)
Cu/Zn	$2c$	0	1/2	1/4	0.83(5)	1.000(2)
Sn	$2c$	0	1/2	1/4	0.83(5)	0.000(2)
Cu/Zn	$2d$	0	1/2	3/4	0.83(5)	0.989(3)
Sn	$2d$	0	1/2	3/4	0.83(5)	0.011(3)
Cu/Zn	$2b$	0	0	1/2	1.15(3)	0.016(2)
Sn	$2b$	0	0	1/2	1.15(3)	0.984(2
S	$8g$	0.7472(12)	0.7612(12)	0.8695(3)	0.48(3)	1

The second half of the as-milled precursor was used to examine the effect of heat treatment on the crystallization of mechanochemically synthesized CZTS powder by *in situ* high-temperature X-ray diffraction. As pointed out in the experimental section, some series of isothermal measurements at 300, 400, and 500 °C were performed. The evolution of the XRD patterns collected during heating is depicted in Figure 6.5 and 6.6. For a first overview, Figure 6.5 presents a 3D plot and a rainbow contour plot of all high temperature X-ray patterns.

In order to avoid informational overflow, Figure 6.6 (left) presents only one half of measured patterns (including the pattern with signals from the empty furnace), whereas in Figure 6.6 (right) the last *in situ* measurement of each annealing temperature (300, 400, 500 °C) as well as the diffraction pattern at 25 °C is shown. Is it clearly seen that the reflections of as-milled CZTS became sharper with heating time, reflecting increased crystallinity.

As expected, increasing temperature led to a decrease of the full width at half maximum (FWHM) values (see Figure 6.7a). The measurement of the starting material (25 °C) gives a calculated crystallite size of 12 nm which is in good agreement with the result from the diffractometer working with Cu-Ka radiation (see Figure 6.4). Having a closer look at the results coming from different annealing temperatures significant differences are found (see Figure 6.7b). At 300 °C the crystallization is rather slow, the crystallite sizes barely increase. After 3.5 h sizes of ~15 nm are reached (see Figure 6.7b). As expected, a significantly faster increase is observed for 400 °C, where a final size of 37 nm is calculated. In the last annealing step at 500 °C the crystallite size is still increasing and reaches a value of 50 nm after 3.5 hours. As shown in Figure 6.7b, the crystallite size increases almost linearly at 400 °C and above.
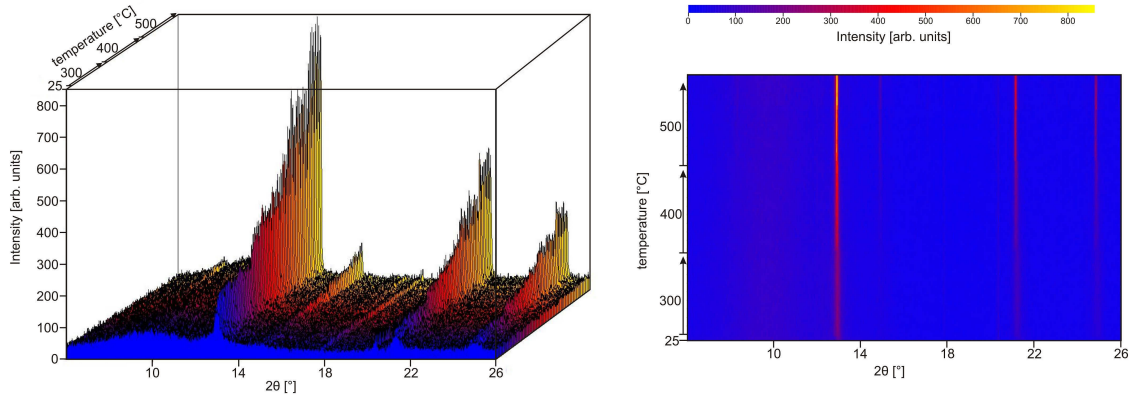
Figure 6.5.: 3D plot (left) and rainbow contour plot (right) for in-situ heat treatment of CZTS precursor powder up to 500 °C (Mo-Ka radiation). In the rainbow color contour plot intensities are shown as color scale where low counts are blue, while higher intensities are shown as red and yellow. Temperature increases from the bottom to the top.

Using the final data set measured at 500 °C (N = 062), the crystal structure was also refined. The X-ray powder pattern with the results of the Rietveld refinement is depicted in Figure 6.8. Lattice parameters and residual values are summarized in Table 6.3. As already described above, space group $I\bar{4}$ was used together with additional side conditions as copper and zinc cannot be distinguished by conventional X-ray diffraction methods. Table 6.4 lists the final atomic and other structural parameters.

Sn is mainly located on Wyckoff position $2b$, whereas Cu/Zn is found on the other three cation sites. No significant amount of Sn was found on positions $2a$ and $2c$. In contrast, a significant amount of tin (~8 %) was found on the $2d$ site, whereas missing Sn is replaced by Cu/Zn on $2b$. For CZTS it is known that intrinsic defects can be easily formed while the kesterite–type structure (space group $I\bar{4}$) is maintained, e.g. [17, 24-26]. Theoretical work [14, 27] has shown that the defect cluster $[Zn_{Sn}^{2-} + Sn_{Zn}^{2+}]$ has relatively low formation energy (around 0.9 eV/pair). Therefore, $Sn_{Cu/Zn}$ and Cu/Zn_{Sn} defects should be present when increasing the temperature. Keep in mind that Zn and Cu cannot be distinguished with conventional X-ray diffraction techniques. Consequently, the actual defect clusters in the present sample cannot be determined unequivocally.

The refined values can be compared with the values for the above-presented sample annealed at 500 °C and cooled down with a rate of 60 K/h. At 500 °C, $Sn_{Cu/Zn}$ and Cu/Zn_{Sn} anti-site defects are clearly present; in the sample slowly cooled down to 25 °C hardly any Sn disorder is found. Consequently, it can be presumed that these defects heal out rapidly during cooling down to ambient temperature. This is also in agreement with our recent
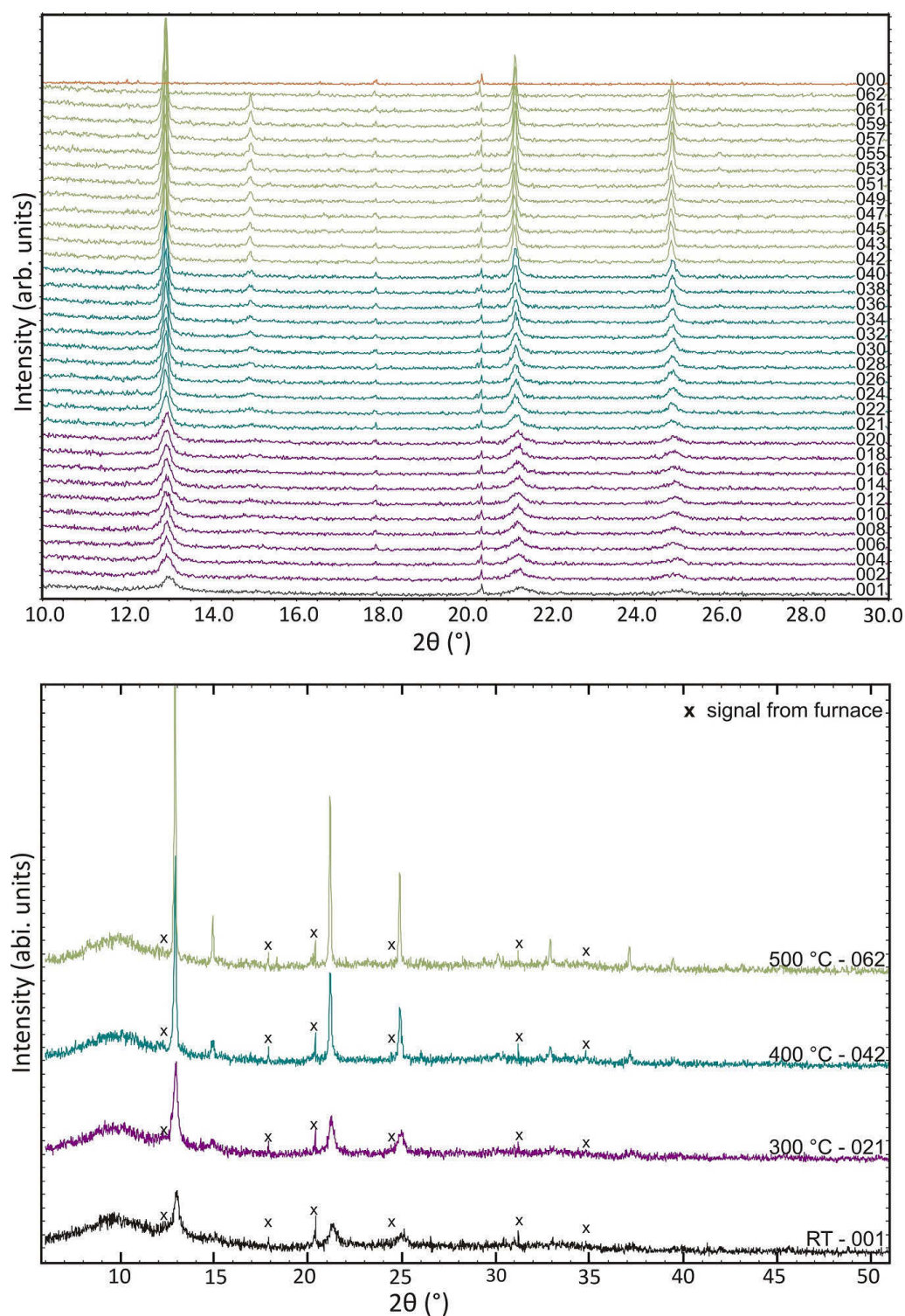
Figure 6.6.: Evolution of the powder patterns probed by *in situ* high temperature X-ray diffraction (Mo-Ka radiation). The number of each pattern corresponds to the measurement number N (see experimental section). Pink: 300 °C, blue: 400 °C, green: 500 °C. The starting pattern at 25 °C is shown in black, the pattern of the empty furnace is depicted in orange.
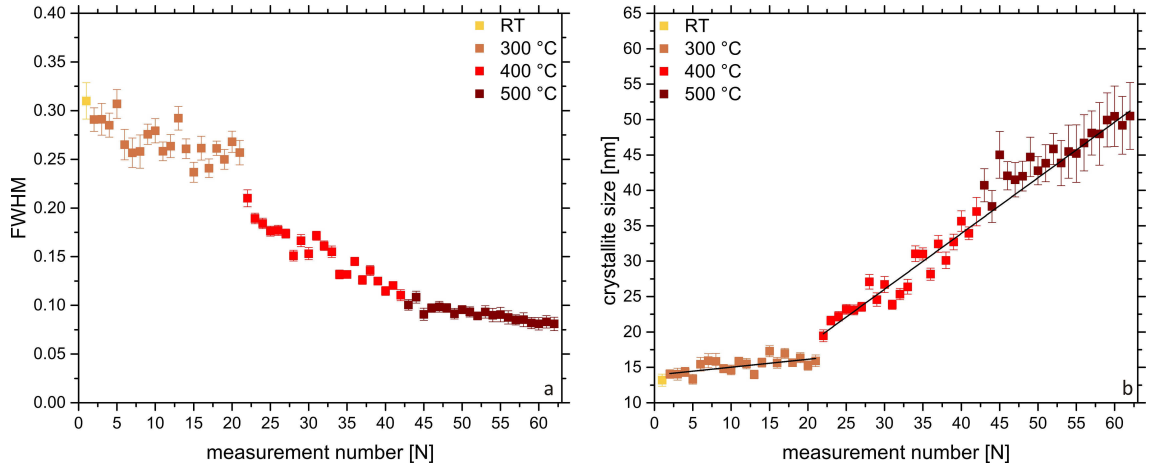
Figure 6.7.: FWHM paramters analysis (a) and calculated crystal sizes (b) for the CZTS precursor.

neutron powder diffraction study on samples annealed for weeks [23]: up to 350 °C no significant disorder of Sn on the remaining three cation positions ($2a$, $2c$, $2d$) is occurring.

It can be expected that the amount of point defects is increasing with increasing temperature, finally resulting in a statistical distribution of copper, zinc, and tin. As mentioned in the introduction, such a high-temperature order-disorder transition was observed by Schorr and Gonzales-Aviles [2], resulting in a cubic sphalerite-type crystal structure.

Table 6.3.: Lattice parameters and residual values of the Rietveld refinement of CZTS at 500 °C

Neutron diffraction	
Structure type	kesterite
Crystal system	tetragonal
Space group	$I\bar{4}$ (No.82)
Diffractometer	STOE STADI P
Wavelength	70.931 pm
2θ range	$10-50°$
T (Measurement)	500 °C
a / pm	546.28(3)
c / pm	1090.10(8)
R_{Bragg} / %	4.77
R_{wp} / %	3.84
R_{exp} / %	3.49
S	1.10
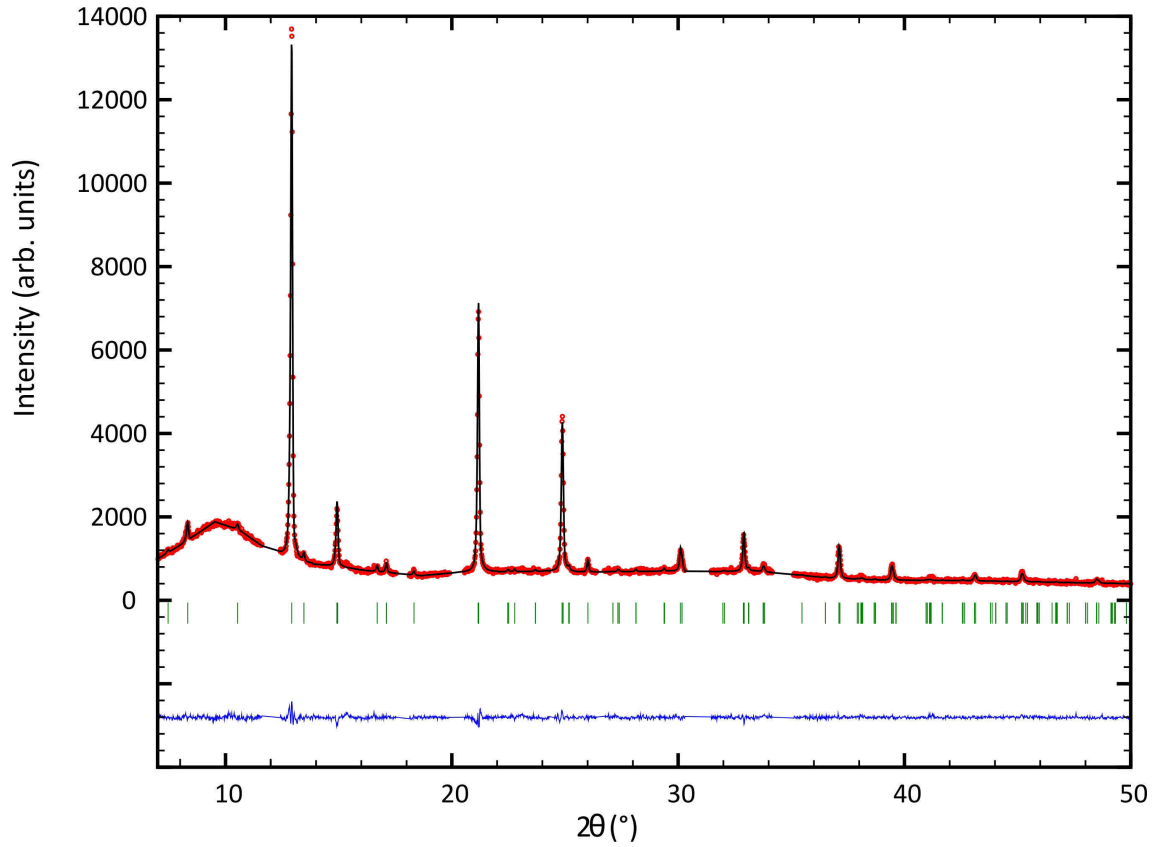
Figure 6.8.: High temperature (500 °C) X-ray powder diffraction pattern with the results of the Rietveld refinement (excluded regions = signals coming from the furnace).

Table 6.4.: Refined structural parameters for CZTS at 500 °C from high temperature X-ray diffraction data

Atom	Wyckoff	x	y	z	Biso	occ
Cu/Zn	2a	0	0	0	4.00(18)	0.997(11)
Sn	2a	0	0	0	4.00(18)	0.004(11)
Cu/Zn	2c	0	1/2	1/4	4.32(13)	1.000(2)
Sn	2c	0	1/2	1/4	4.32(13)	0.000(2)
Cu/Zn	2d	0	1/2	3/4	4.32(13)	0.922(16)
Sn	2d	0	1/2	3/4	4.32(13)	0.080(16)
Cu/Zn	2b	0	0	1/2	2.36(8)	0.084(11)
Sn	2b	0	0	1/2	2.36(8)	0.918(11)
S	8g	0.748(6)	0.757(5)	0.8699(10)	1.94(9)	1

6.5. Conclusions

In this work our recently developed mechanochemical synthesis process to phase pure CZTS powder was investigated in more detail. The reaction of the binary sulfides in the ball mill was followed by X-ray diffraction measurements. The crystallite size of the as-milled CZTS powder approaches a value of 10 nm after 3 h of milling. In addition, the crystallization behavior with temperature was investigated by *in situ* high-temperature X-ray diffraction. At 500 °C, $Sn_{Cu/Zn}$ and Cu/Zn_{Sn} anti-site defects are clearly observed. Their concentration strongly decreases when cooling down the sample. The cooling rate of 60 K/h seems to be the limit for the production of samples with low Sn-involved disorder, which is important for the performance of CZTS in solar cells. For a more detailed analysis of ordering processes up to the disordered cubic phase, *in situ* high-temperature neutron powder diffraction investigations are planned.

Acknowledgement

References

[1] S. Schorr, H.-J. Hoebler, M. Tovar, *Eur. J. Mineral.* **2007**, *19*, 65 – 73.

[2] S. Schorr, G. Gonzalez-Aviles, *Phys. Status Solidi A* **2009**, *206*, 1054 – 1058.

[3] J. Just, D. Luetzenkirchen-Hecht, R. Frahm, S. Schorr, T. Unold, *Appl. Phys. Lett.* **2011**, *99*, 262105/1 – 262105/3.

[4] S. Chen, X.G. Gong, A. Walsh, S.-H. Wei, *Appl. Phys. Lett.* **2010**, *96*, 021902/1 – 021902/3.

[5] S. Chen, L.-W. Wang, A. Walsh, X.G. Gong, S.-H. Wei, *Appl. Phys. Lett.* **2012**, *101*, 223901/1 – 223901/4.

[6] A.J. Jackson, A. Walsh, *J. Mater. Chem. A*, **2014**, 7829 – 7836.

[7] S. Chen, X.G. Gong, A. Walsh, S.-H. Wei, *Appl. Phys. Lett.* **2009**, *94*, 041903/1 – 041903/3.

[8] J.J. Scragg, P.J. Dale, L.M. Peter, G. Zoppi, I. Forbes, *Phys. Status Solidi B* **2008**, *245*, 1772 – 1778.

[9] S. Siebentritt, S. Schorr, *Prog. Photovoltaics* **2012**, *20*, 512 – 519.

[10] W. Wang, M.T. Winkler, O. Gunawan, T. Gokmen, T.K. Todorov, Y. Zhu, D.B. Mitzi, *Adv. Energy Mater.* **2014**, *4*, 1301465/1 – 1301465/5.

[11] S. Schorr, *Sol. Energy Mater. Sol. Cells* **2011**, *95*, 1482 – 1488.

[12] L. Choubrac, M. Paris, A. Lafond, C. Guillot-Deudon, X. Rocquefelte, S. Jobic, *Phys. Chem. Chem. Phys.* **2013**, *15*, 10722 – 10725.

[13] A. Nagoya, R. Asahi, R. Wahl, G. Kresse, *Phys. Rev. B Condens. Matter Mater. Phys.* **2010**, *81,* 113202/1 – 113202/4.

[14] S. Chen, J.-H. Yang, X.G. Gong, A. Walsh, S.-H. Wei, *Phys. Rev. B: Condens. Matter Mater. Phys.* **2010**, *81*, 245204/1 – 245204/10.

[15] S. Schorr, M. Tovar, B*ENSC Experimental Report* **2006**.

[16] A. Ritscher, J. Just, O. Dolotko, S. Schorr, M. Lerch, *J. Alloys Compd.* **2016**, *670*, 289 – 296.

[17] L.E. Valle Rios, K. Neldner, G. Gurieva, S. Schorr, *J. Alloys Compd.* **2016**, *657*, 408 – 413.

[18] C.F. Burmeister, A. Kwade, *Chem. Soc. Rev.* **2013**,*42*, 7660 – 7667.

[19] D. Pareek, K.R. Balasubramaniam, P. Sharma, *Mater. Charact.* **2015**, *103*, 42 – 49.

[20] H.M. Rietveld, *J. Appl. Crystallogr.* **1969**, *2*, 65 – 71.

[21] J. Rodriguez-Carvajal, *Abstracts of the Satellite Meeting on Powder Diffraction of the XV.Congress of the IUCr* **1990**, 127.

[22] P. Scherrer, *Nachrichten von der Gesellschaft der Wissenschaften zu Göttingen, Mathematisch-Physikalische Klasse 1918* **1918**.

[23] A. Ritscher, M. Hoelzel, M. Lerch, *J. Solid State Chem.* **2016**, *238*, 68 – 73.

[24] G. Gurieva, M. Dimitrievska, S. Zander, A. Perez-Rodriguez, V. Izquierdo-Roca, S. Schorr, *Phys. Status Solidi C* **2015**, *12*, 588 – 591.

[25] A. Lafond, L. Choubrac, C. Guillot-Deudon, P. Deniard, S. Jobic, *Z. Anorg. Allg. Chem.* **2012**,*638*, 2571 – 2577.

[26] L. Choubrac, A. Lafond, C. Guillot-Deudon, Y. Moelo, S. Jobic, *Inorg. Chem.* **2012**, *51*, 3346 – 3348.

[27] S. Chen, A. Walsh, X.-G. Gong, S.-H. Wei, *Adv. Mater.* **2013**, *25*,1522 – 1539.

7. Publication 4

Off-stoichiometric CZTS: Neutron scattering investigations on mechanochemically synthesized powders

Anna Ritscher, Alexandra Franz, Susan Schorr, Martin Lerch

Contribution to publication:

A. Ritscher: Sample preparation, analysis and evaluation, writing.

F. Franz: Measurements (neutron diffraction).

S. Schorr   General discussion, proofreading.

M. Lerch: General advice and helpful comments, proofreading.

Overall contribution of A. Ritscher to the publication: 75 %

Authors   A. Ritscher [1,2], A. Franz [2], S. Schorr [2,3], M. Lerch [*][1]

[1] Institut für Chemie, Technische Universität Berlin, Straße des 17.Juni 115, 10623 Berlin, Germany

[2] Helmholtz-Zentrum Berlin für Materialien und Energie, Hahn-Meitner-Platz 1, 14109 Berlin, Germany

[3] Institut für Geologische Wissenschaften, Freie Universität Berlin, Malteserstr. 74, 12249 Berlin, Germany

[*] corresponding author

7.1. Abstract

In this work a series of B- and C-type off-stoichiometric CZTS samples was prepared by a mechanochemical synthesis route. For structural characterization X-ray diffraction measurements were performed. Furthermore, compositional analyses of the powder samples were carried out by means of wavelength-dispersive X-ray spectroscopy (WDS). For detailed cation distribution analyses of two off-stoichiometric single-phase samples neutron diffraction methods were used. The method of the average neutron scattering length was applied revealing the occurrence of Zn_{Cu}, Cu_{Zn}, and Zn_{Sn} point defects in the Cu-poor/Zn-rich sample (B-type, $Cu_{1.95}Zn_{1.09}Sn_{0.96}S_{4.00}$), whereas for the Cu-rich/Zn-poor sample (C-type, $Cu_{2.04}Zn_{0.95}Sn_{1.01}S_{4.00}$) Zn_{Cu}, Cu_{Zn}, and Sn_{Zn} defects are suggested.

7.2. Introduction

The quaternary p-type semiconductor compound Cu_2ZnSnS_4 has been examined intensively as an alternative absorber material for thin film solar cells in recent years. It is considered as a suitable candidate for photovoltaic applications due to its high absorption coefficient ($> 10^{-4}\,cm^{-1}$), a desirable direct optical bandgap ($1.5\,eV$) as well as the sufficient abundance and the non-toxicity of the raw materials [1-3].

The crystal structure of Cu_2ZnSnS_4 has long been a controversial topic. Different studies proved that the quaternary sulfide adopts the kesterite structure type (space group $I\bar{4}$) [4, 5]. In this sphalerite-derived crystal structure four cation positons are available. Sn is located on Wyckoff position $2b$ $(0, 0, 1/2)$ and Cu on position $2a$ $(0, 0, 0)$, occupying the lattice planes at $z = 0$ and $1/2$, respectively. The lattice planes at $z = 1/4$ and $3/4$ are filled with Zn (site $2d$ $(0, 1/2, 3/4)$) and the remaining Cu (site $2c$ $(0, 1/2, 1/4)$). Additionally, partial or complete disorder of Cu and Zn on Wyckoff positions $2c$ and $2d$ are reported [6-8]. As shown by theoretical calculations [9, 10], the defect cluster $[Zn_{Cu} + Cu_{Zn}]$ has the lowest formation energy compared to other defect complexes in the CZTS system, which underlines the possibility of copper/zinc disorder in the sample.

Until now, record efficiencies of thin film solar cells based on CZTS have reached $8.4\,\%$ [11] and for devices with additional selenium even $12.6\,\%$ were achieved [12]. In both cases, these photovoltaic performances were not obtained using stoichiometric compounds, the applied materials rather exhibit Cu-poor/Zn-rich compositions. Consequently, it is of strong interest to study and elucidate the relation between composition, crystal structural, and electronic properties of the material.

In recent studies it was shown that also compositions beside the ideal Cu_2ZnSnS_4 stoichiometry can exhibit the Kesterite-type structure. This structural flexibility was first investigated by Lafond et al. [13, 14], who introduced 4 off-stoichiometry types of kesterite,

which can be characterized by different cation substitution reactions and the formation of related point defect clusters in order to maintain the charge balance in the structure. In CZTS literature the substitution types are mainly related to the cation ratios $Cu/(Zn+Sn)$ and Zn/Sn resulting in a cation ratio plot as depicted in Figure 7.1 (right). It can be seen that the plot is divided into four regions: Cu-poor/Zn-rich, Cu-poor/Zn-poor, Cu-rich/Zn-rich, Cu-rich/Zn-poor. These regions can be associated with the different off-stoichiometric types.

In the so-called A-type (Cu-poor, Zn-rich region) defect complexes with zinc on copper antisites and copper vacancies ($[Zn_{Cu} + V_{Cu}]$) are present. Another Cu-poor/Zn-rich type can be attained by the substitution of copper and tin forming copper (Zn_{Cu}) and tin (Zn_{Sn}) point defects (B-type). The C-type point defects can be seen as the opposite of the B-type ones, forming copper on zinc antisites by substitution with copper (Cu_{Zn}) and tin (Sn_{Zn}).The reverse of the A-type is the D-type (Cu-rich/Zn-poor region) where zinc is replaced by copper forming copper on zinc antisites (Cu_{Zn}) and copper interstitials (Cu_i). While A-, B-, and C-type off-stoichiometric CZTS samples were also observed experimentally by Lafond et al. [13], D-type was introduced only according to charge balance considerations. To our knowledge, no single phase D-type sample could be prepared yet. Valle-Rios et al. [15] prepared C-D- and D-F-type mixtures with kesterite as major phase but with additional secondary phases.

Recently, investigations on the ability of CZTS(Se) to deviate from the stoichiometry were performed on kesterite powder samples by Valle-Rios et al. [15] introducing a new off-stoichiometry type, the so-called F-type. To form this special type of off-stoichiometric kesterite, tin is replaced in the structure forming a Cu-rich/Zn-rich composition. Two defect complexes are possible, the formation of zinc on tin positions with additional copper interstitials ($[Zn_{Sn} + 2\,Cu_i]$) or copper on tin sites and two interstitials ($[Cu_{Sn} + Cu_i + Zn_i]$). The opposite of this type of cation substitution would be the E-type which first appeared in Ref. [16]. In this Cu-poor/Zn-poor type copper and zinc are substituted forming either tin on zinc antisites (Sn_{Zn}) and copper vacancies (V_{Cu}) or tin on copper antisites (Sn_{Cu}) as well as copper and zinc vacancies ($V_{Cu} + V_{Zn}$). According to our research, no information about single phase E- or F-type CZTS can be found in literature, except B-F-type mixture samples [15] up to 76 % F-type fraction. Due to the high formation energies of interstitial Zn and Cu compared to other point defects in the CZTS system [9, 10], it seems to be rather unlikely that single phase F-type samples are formed. The formation energies of the defect complexes $[2\,Cu_{Zn} + Sn_{Zn}]$ and $[Zn_{Cu} + V_{Cu}]$ have rather low values, with $0.2-0.6$ and $0.4\,eV$, respectively [9, 10]. This may be an indication that single-phase A- and C-type samples are generally more easily formed. In Table 7.1 all these off-stoichiometry types are summarized.

Table 7.1.: Off-stoichiometric kesterite types and its cation substitution reactions. *[first reported]

type	formula	composition	cation substitution reaction	synthesis temp./ °C,*
A	$Cu_{2-2x}Zn_{1+x}SnS_4$	Cu-poor/Zn-rich/ Sn-constant	$2\,Cu^+ \rightarrow Zn_{Cu}^{2+} + V_{Cu}$	750, [13]
B	$Cu_{2-2x}Zn_{1+3x}Sn_{1-x}S_4$	Cu-poor/Zn-rich/Sn-poor	$2\,Cu^+ + Sn^{4+} \rightarrow 2\,Zn_{Cu}^{2+} + Zn_{Sn}^{2+}$	750, [13]
C	$Cu_{2+2x}Zn_{1-3x}Sn_{1+x}S_4$	Cu-rich/Zn-poor/Sn-rich	$3\,Zn^{2+} \rightarrow 2\,Cu_{Zn}^+ + Sn_{Zn}^{4+}$	750, [13]
D	$Cu_{2+2x}Zn_{1-x}SnS_4$	Cu-rich/Zn-poor/Sn-constant	$Zn^{2+} \rightarrow Cu_{Zn}^+ + Cu_i^+$	not reported as single phase
E	$Cu_{2-2x}Zn_{1-x}Sn_{1+x}S_4$	Cu-poor/Zn-poor/Sn-rich	$2\,Cu^+ + Zn^{2+} \rightarrow 2\,V_{Cu} + Sn_{Zn}^{4+}$ $\rightarrow Sn_{Cu}^{4+} + V_{Cu} + V_{Zn}$	not reported as single phase
F	$Cu_{2+2x}Zn_{1+x}Sn_{1-x}S_4$	Cu-rich/Zn-rich/Sn-poor	$Sn^{4+} \rightarrow Zn_{Sn}^{2+} + 2\,Cu_i^+$ $\rightarrow Cu_{Sn}^+ + Cu_i^+ + Zn_i^{2+}$	750 (B-F-type mixture), [15]

CZTS powder has been usually synthesized via a solid state reaction process at 750 °C in evacuated silica ampoules [8, 15]. Using this procedure it is not so easy to control the final composition of the sample. For example: in Ref. [15] only a few sample compositions can be correlated to solely one off-stoichiometry type, most of the synthesized samples show a mixture of two different types. However, for a comprehensive clarification of the cation order in each off-stoichiometry type the synthesis of single-type powders is important. As it is seen in our recent studies, it is nicely possible to control the composition of the synthesized CZTS powder with the developed mechanochemical process [7, 17]. In this contribution the new process was used to synthesize off-stoichiometric CZTS samples (B- and C-type). The limits of single-phase samples for the B- and C-type were investigated. Furthermore, a detailed study on the cation ordering in selected off-stoichiometric samples was performed. As Cu and Zn are not distinguishable with X-rays, neutron powder diffraction measurements were performed.

7.3. Experimental

14 CZTS powder samples of the B- and C-type were prepared according to our recently developed two-step mechanochemical process [17]. The synthesis starts from the corresponding binary sulfides (CuS, ZnS, SnS) which were filled in an 80 ml agate jar (including

5 grinding balls, $\varnothing$ 20 mm) and milled in a Fritsch Planetary Mono Mill PULVERISETTE 6 for 5 h with a rotational speed of 350 pm. In a second step each sample was annealed in a conventional tube furnace (SiO$_2$-tube, $\varnothing$ 70 mm) under flowing H2S-gas for 3 h at 500 °C. After this heat treatment the samples were cooled down with a cooling rate of 60 K/h. At this annealing step powder samples with good crystallinity are achieved. For the determination of the exact chemical composition and phase contents (possible secondary phases) of the synthesized CZTS samples, the powders were analyzed by wavelength dispersive X-ray spectroscopy (WDS) using an electron microprobe analyzer (JEOL-JXA 8200 System). For calibration of the system elemental standards of Cu, Zn, and Sn as well as the mineral chalcopyrite for S was used. In order to obtain accurate and reliable values for the chemical composition of each sample 20 grains averaging over 15 point measurements within each grain were measured.

Structural characterization and quantitative phase analysis were done by X-ray powder diffraction using a Panalytical X'Pert PRO diffractometer (Bragg-Brentano geometry, Cu-Ka radiation). Additionally, neutron powder diffraction measurements of one sample of each off-stoichiometry type were performed. Data were collected at the Berlin Research Reactor BER II at the Helmholtz-Zentrum Berlin für Materialien und Energie using the fine resolution powder diffractometer FIREPOD (E9) at ambient temperature and $\lambda = 179.8$ pm (Ge(511)). For the measurement the samples were encapsulated in vanadium tubes of 6 mm diameter.

Structural refinements were performed by the Rietveld method [19] using the program FULLPROF Suite Version 2015 [20] by applying a pseudo-Voigt (X-ray data) and a Thompson-Cox-Hasting pseudo-Voigt function (neutron data), respectively. The kesterite-type structure (space group $I\bar{4}$) was used as starting model for the refinements, with the following cation distribution: Cu on positions $2a$ $(0, 0, 0)$ and $2c$ $(0, 1/2, 1/4)$, Zn on position $2d$ $(0, 1/2, 3/4)$, and Sn on Wyckoff position $2b$ $(0, 0, 1/2)$.

7.4. Results and discussion

Fourteen off-stoichiometric CZTS samples have been synthesized successfully according to our recently developed mechanochemical process [17]. The chemical compositions of the kesterite powders, according to the WDS results, are plotted in the ternary phase diagram in Figure 7.1 (left). For a better overview the cation ratios Cu/(Zn+Sn) and Zn/Sn are usually used for defining the composition of kesterite-type samples [15, 16]. This cation ratio plot is depicted in Figure 7.1 (right) showing the 8 B-type and 6 C-type off-stoichiometric samples. It can be seen that all compositions lie on the line of the specific off-stoichiometry type. In comparison to the work of Valle-Rios et al. [15] it is

evident that the preparation of single-type off-stoichiometric CZTS powders is easier with our mechanochemical route.
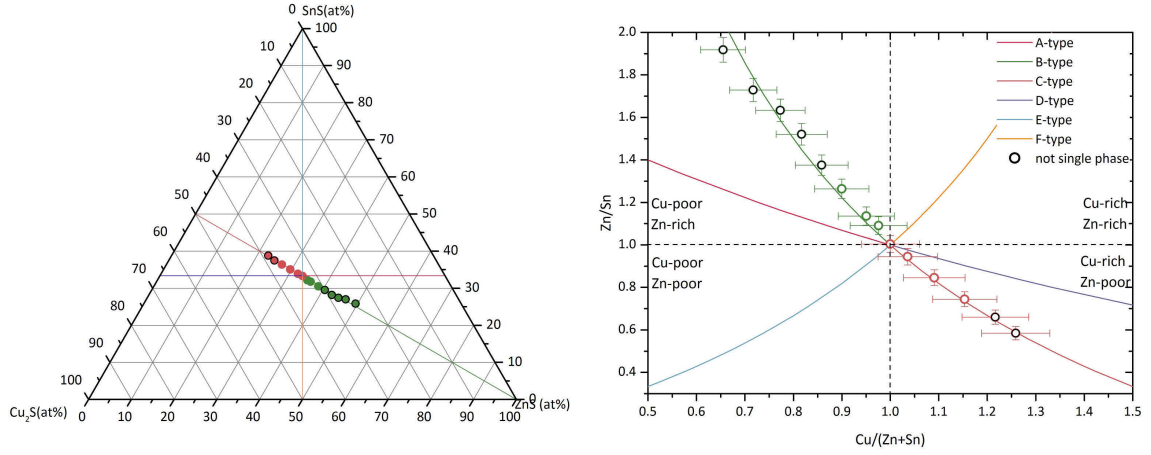
Figure 7.1.: Prepared B-type (green) and C-type (red) CZTS powder samples. Left: Ternary phase diagram. Right: Cation ratio plot of the synthesized off-stoichiometric sampels. Each line corresponds to one off-stoichiometric CZTS type (calculated according the formulas described in Table 7.1).

According to the results of the electron microprobe analyses, seven single-phase off sto-ichiometric kesterite samples, in both B- and C-type region, were successfully synthe-sized. It was possible to prepare single-phase materials up to cation ratios of $0.90-1.15$ for Cu/(Zn+Sn) and $0.74-1.09$ for Zn/Sn. In comparison, Valle-Rios et al. [15] realized cation ratios up to $0.96-1.01$ for Cu/(Zn+Sn) and $1.03-1.12$ for Zn/Sn for single-phase powders. Furthermore, in other works the limit of single phase off-stoichiometric CZTS is significantly lower. Olekseyuk et al. [21], who studied the phase diagram of the Cu2S-ZnS-SnS2 system up to 1150 °C, proposed a homogeneity region 3 at% at 400 °C. Lafond et al. [13] prepared off-stoichiometric CZTS samples at 750 °C and reached the limit in the B-type region with a sample $Cu_{1.945(13)}Zn_{1.06(2)}Sn_{0.979(4)}S_{4.00(2)}$, which is also lower than in the current work. The wider expansion of the single phase region can probably be attributed to the mechanochemical synthesis method and the relatively low synthesis temperature of 500 °C which suppresses the formation of secondary phases [17].

Secondary phases have been detected in samples far off the stoichiometric composition. In samples belonging to the C-type, copper sulfide ($Cu_{1.8}S$) was found, which is ratified by the Cu-rich composition. In B-type samples, the full range of secondary phases was found, including ZnS, SnS_2, and copper sulfides such as CuS and $Cu_{1.8}S$. These findings are comparable to the results of Valle-Rios et al. [15] who found similar secondary phases in their off-stoichiometric sulfide samples. All detected secondary phases are listed in Table 7.2.

Table 7.2.: Prepared off-stoichiometric samples including cation ratios obtained from WDS measurements, occuring secondary phases, and refined lattice parameters from the XRD data.

sample		formula	Cu/(Zn+Sn)	Zn/Sn	lattice parameter a (pm)	c (pm)	secondary phases
B-type	B1	$Cu_{1.98}Zn_{1.06}Sn_{0.97}S_{4.00}$	0.98	1.09	543.160(15)	1083.94(4)	-
	B2	$Cu_{1.95}Zn_{1.09}Sn_{0.96}S_{4.00}$	0.95	1.14	543.17(14)	1084.14(4)	-
	B3	$Cu_{1.89}Zn_{1.18}Sn_{0.93}S_{4.00}$	0.90	1.26	543.108(19)	1083.85(6)	-
	B4	$Cu_{1.85}Zn_{1.25}Sn_{0.91}S_{4.00}$	0.86	1.38	543.294(15)	1083.88(5)	ZnS, $Cu_{1.8}S$
	B5	$Cu_{1.80}Zn_{1.33}Sn_{0.87}S_{4.00}$	0.82	1.52	542.975(19)	1083.47(6)	CuS, ZnS
	B6	$Cu_{1.74}Zn_{1.40}Sn_{0.86}S_{4.00}$	0.77	1.63	543.090(11)	1084.11(4)	ZnS
	B7	$Cu_{1.67}Zn_{1.48}Sn_{0.85}S_{4.00}$	0.72	1.73	543.18(4)	1083.05(15)	SnS_2, ZnS
	B8	$Cu_{1.58}Zn_{1.59}Sn_{0.83}S_{4.00}$	0.65	1.92	543.203(11)	1083.48(4)	SnS_2, ZnS
C-type	C1	$Cu_{2.00}Zn_{1.00}Sn_{1.00}S_{4.00}$	1.00	1.00	543.27(3)	1084.37(7)	-
	C2	$Cu_{2.04}Zn_{0.95}Sn_{1.01}S_{4.00}$	1.04	0.94	543.26(3)	1084.45(6)	-
	C3	$Cu_{2.09}Zn_{0.88}Sn_{1.04}S_{4.00}$	1.09	0.85	543.31(3)	1084.42(8)	-
	C4	$Cu_{2.14}Zn_{0.79}Sn_{1.06}S_{4.00}$	1.15	0.74	543.19(3)	1084.75(7)	-
	C5	$Cu_{2.20}Zn_{0.72}Sn_{1.09}S_{4.00}$	1.22	0.66	543.45(5)	1085.11(14)	$Cu_{1.8}S$
	C6	$Cu_{2.23}Zn_{0.65}Sn_{1.12}S_{4.00}$	1.26	0.58	543.26(3)	1085.03(8)	$Cu_{1.8}S$

First structural characterizations of the off-stoichiometric samples have been performed by means of X-ray powder diffraction. The refined lattice parameters off all off-stoichiometric samples are summarized in Table 2. Additionally, in Figure 7.2, the lattice parameters a and $c/2$ of the kesterite-type phase in dependence of the cation ratios (Cu/(Zn+Sn), Zn/Sn) are depicted. It can be easily seen that only a small variation of the lattice parameters is observed for off-stoichiometric CZTS samples. Looking at the behavior of the lattice parameter a as function of the cation ratio Cu/(Zn+Sn), only a slight alternation of 0.4 pm is observed, whereas the change of $c/2$ is more significant (variation of 2.1 pm) for Cu-poor/Zn-rich to Cu-rich/Zn-poor compositions. In comparison, when going from Zn-poor/Sn-rich to Zn-rich/Sn-poor compositions (cation ratio Zn/Sn) both lattice parameters are decreasing.
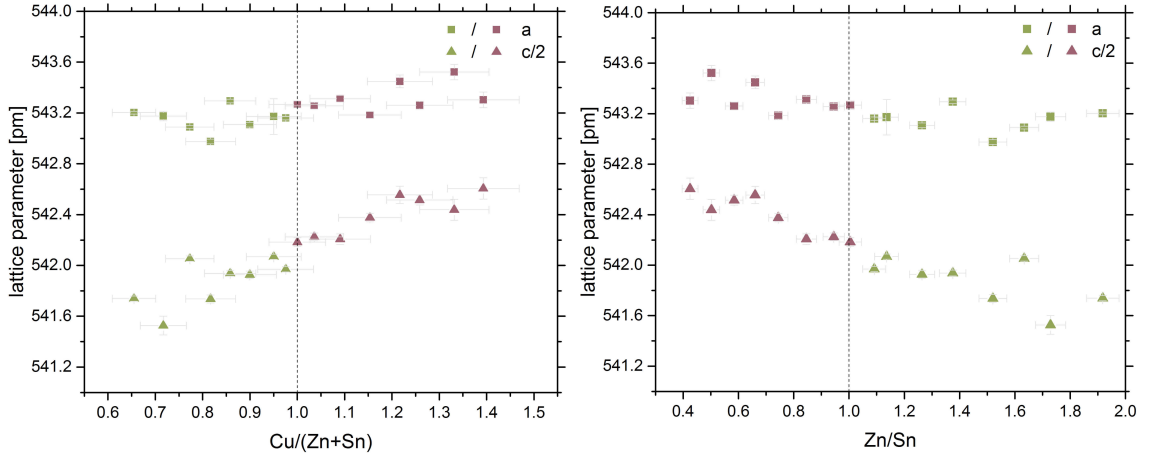
Figure 7.2.: X-ray powder diffraction pattern with the results of the Rietveld refinement using the kesterite-type structure as starting model.

With conventional X-ray powder diffraction, it is not possible to perform a full cation distribution analysis. In order to reveal the distribution of Cu, Zn, and Sn on the four crystallographic sites, neutron diffraction measurements of two single-phase samples, one of each off-stoichiometric type (samples B2 and C2), were performed. The cation distribution was determined using the method of average neutron scattering length. This method was described in detail by Schorr et al. [22] and was already used in several other works [4, 7, 16, 17]. Starting from the refined site occupation values (occ) it is possible to calculate the experimental average neutron scattering length according to Equation 1.1.

$$\bar{b}_i^{exp} = occ_i \cdot b_j \tag{7.1}$$

using the scattering lengths of the particular cation j on position i ($b_{\text{Cu}} = 7.718\,\text{fm}$, $b_{\text{Zn}} = 5.680\,\text{fm}$, $b_{\text{Sn}} = 6.225\,\text{fm}$). The values of $\bar{b}_i^{exp}$ are compared with the neutron scat-

tering length of the presumed cation on the particular site ($2a$, $2c$: Cu; $2d$: Zn; $2b$: Sn). If a deviation from the initial value is observed, one can predict that this cation site is not exclusively occupied by the supposed cation species. In order to calculate the cation distribution on each cation site Equation 1.2 is used.

$$\bar{b}_i = x_i \cdot b_{Cu} + y_i \cdot b_{Zn} \tag{7.2}$$

where X_i, Y_i, and Z_i are the fraction of Cu, Zn, and Sn on the respective site and $\bar{b}_i$ is the calculated average neutron scattering length of site i ($2a$, $2c$, $2d$, $2b$). For the evaluation of the cation distribution a global optimization procedure was applied where all values are optimised simultaneously. Following conditions have to be fulfilled: minimization of the difference between $\bar{b}_i^{exp}$ and $\bar{b}_i$, each position is fully occupied (keep in mind that there are no vacancies in B and C-type, see Table 7.1) and the given stoichiometry is respected.

Table 7.3.: Lattice parameters of sample B2 with composition $Cu_{1.95}Zn_{1.09}Sn_{0.96}S_{4.00}$ and residual values of the Rietveld refinement

B2	Neutron diffraction
Structure type	kesterite
Crystal system	tetragonal
Space group	$I\bar{4}$ (No.82)
Diffractometer	E9
Wavelength	179.8 pm
2θ range	$10-140°$
a / pm	543.264(12)
c / pm	1084.62(5)
R_{Bragg} / %	2.98
R_{wp} / %	2.53
R_{exp} / %	1.97
S	1.30

The refined parameters of the sample B2 with composition $Cu_{1.95}Zn_{1.09}Sn_{0.96}S_{4.00}$ are depicted in Table 7.3 and 7.4. The following cation distribution can be proposed: copper fully occupies the 2a position. The average neutron scattering length of the copper 2c position is reduced significantly which would suggest Zn_{Cu} antisites defects. An indication for Cu_{Zn} defects is found on position 2d due to the increased average neutron scattering length compared to the value of Zn. On the other hand, the average neutron scattering length of 2b is decreased, indicating that this site is also occupied by Zn.
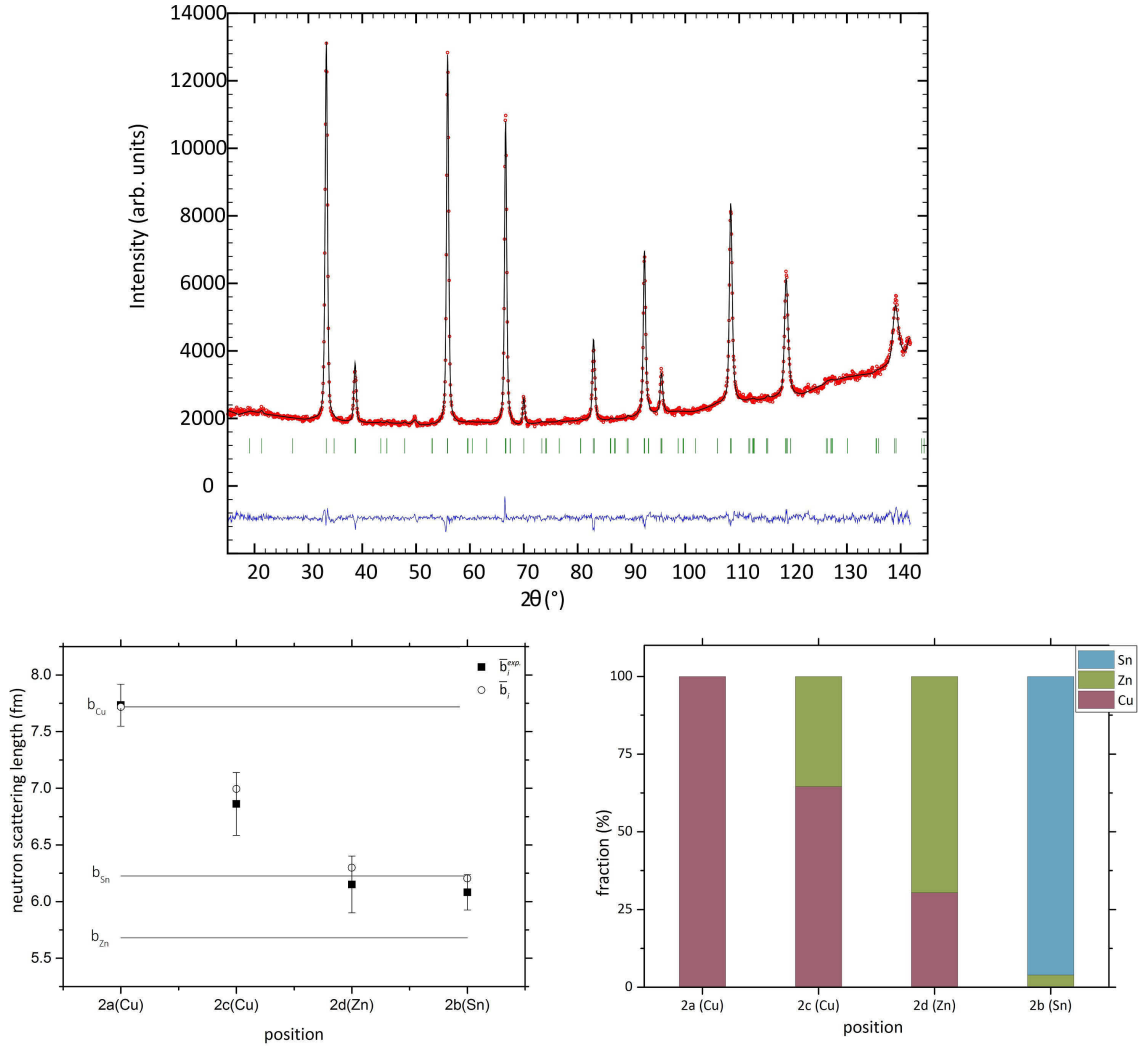
Figure 7.3.: Sample B2 Top: Neutron powder diffraction pattern with the results of the Rietveld refinement. Left: Experimental average neutron scattering length of the four cation sites - $\bar{b}_i^{exp}$ (rectangle) and $\bar{b}_i$ (circle). Right: Resulting cation distribution.

Table 7.4.: Refined structural parameters for sample B2 from neutron diffraction data

Atom	Wyckoff	x	y	z	Biso	occ
Cu	$2a$	0	0	0	2.4(3)	1.00(2)
Cu	$2c$	0	1/2	1/4	1.1(3)	0.89(4)
Zn	$2d$	0	1/2	3/4	1.4(3)	1.08(4)
Sn	$2b$	0	0	1/2	0.2(3)	0.98(3)
S	$8g$	0.7661(17)	0.752(5)	0.8687(10)	0.88(5)	1

These predictions are supported by the theoretical point defects of B-type CZTS. In this off-stoichiometric type Zn_{Cu} and Zn_{Sn} anti-site defects are expected [13]. Figure 7.3 shows the neutron powder diffraction pattern with results of the Rietveld refinement as well as the resulting cation distribution on the four cation positions.

The refined parameters of the sample C2 with composition $Cu_{2.04}Zn_{0.95}Sn_{1.01}S_{4.00}$ are depicted in Table 7.5 and 7.6. Comparing the experimental average neutron scattering lengths with the values of Cu, Zn, and Sn it can be seen that, like in the sample B2, copper fully occupies the 2a position. Also the 2b position is occupied by the presumed cation Sn. As the sample is Sn-rich, remaining tin is suggested to be on site 2d according to the expected defect complex of this off-stoichiometry type (C-type: Cu_{Zn} and Sn_{Zn}) [13]. This prediction is also supported by the significantly increased average neutron scattering length of the zinc $2d$ position. Also Cu_{Zn} antisites are predicted on this position. Additionally, the presence of Zn_{Cu} anti-sites is suggested on position $2c$, due to the reduced average neutron scattering length. Figure 7.4 shows the neutron powder diffraction pattern of sample C2 with results of the Rietveld refinement as well as the resulting cation distribution on the four positions.

Table 7.5.: Lattice parameters of sample C2 with composition $Cu_{2.04}Zn_{0.95}Sn_{1.01}S_{4.00}$ and residual values of the Rietveld refinement

C2	Neutron diffraction
Structure type	kesterite
Crystal system	tetragonal
Space group	$I\bar{4}$ (No.82)
Diffractometer	E9
Wavelength	179.8 pm
2ϑ range	$10-140°$
a / pm	543.476(8)
c / pm	1084.77(3)
R_{Bragg} / %	2.34
R_{wp} / %	2.36
R_{exp} / %	2.09
S	1.13

Table 7.6.: Refined structural parameters for sample C2 from neutron diffraction data

Atom	Wyckoff	x	y	z	Biso	occ
Cu	$2a$	0	0	0	2.3(3)	0.98(3)
Cu	$2c$	0	1/2	1/4	1.2(4)	0.90(4)
Zn	$2d$	0	1/2	3/4	1.1(4)	1.14(5)
Sn	$2b$	0	0	1/2	0.3(3)	1.02(3)
S	$8g$	0.764(4)	0.757(9)	0.8705(11)	0.79(5)	1
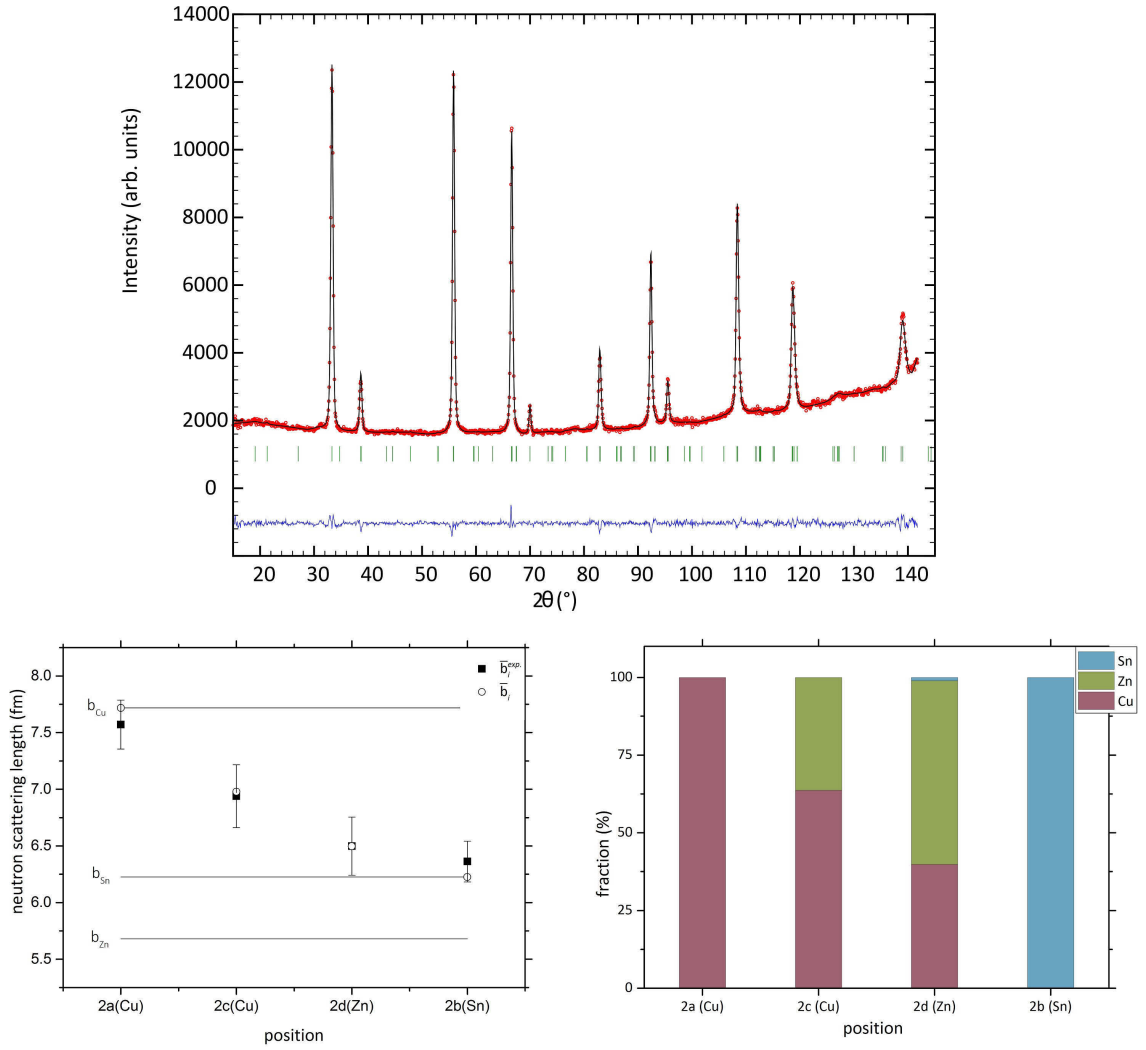
Figure 7.4.: Sample C2 Top: Neutron powder diffraction pattern with the results of the Rietveld refinement. Left: Experimental average neutron scattering length of the four cation sites - $\bar{b}_i^{exp}$ (rectangle) and $\bar{b}_i$ (circle). Right: Resulting cation distribution.

Table 7.7 summarizes all observed point defect types in the CZTS samples investigated in detail. In both samples the expected point defects attributed to the specific off-stoichiometric CZTS type are present [13]: Zn_{Cu} and Zn_{Sn} in the B-type sample, Cu_{Zn} and Sn_{Zn} in the C-type sample. Additionally, and not surprising, Zn_{Cu} and Cu_{Zn} defect pairs related to the order-disorder behavior on positions 2c and 2d are found. In stoichiometric single-phase CZTS powder a partial Cu/Zn-disorder of ~30 % on these positions is reported [17]. This disorder disappears when annealing the powder at low temperatures (200 °C) for a long time period (3 weeks) [7]. It should be mentioned that the rate of cation ordering seems to be strongly dependent on the composition of the sample [23]. For example, as shown by Rudisch et al. [24], even after 27 years full order seems to be not reached in B-type kesterite.

Table 7.7.: Summary of all occurring point defects in samples B2 and C2

| Atom | Defect types | |
	Sample B2	Sample C2
2a	-	-
2c	Zn_{Cu} 35 %	Zn_{Cu} 36 %
2d	Cu_{Zn} 30 %	Cu_{Zn} 40 % Sn_{Zn} 1 %
2b	Zn_{Sn} 4 %	-

7.5. Conclusions

Off-stoichiometric CZTS powder samples of the B- and C-type were successfully prepared with a mechanochemical synthesis process. WDS measurements showed that this method is suitable for controlling the composition of the synthesized sample. Furthermore, it is possible to prepare single-phase samples far off the stoichiometric composition. Analyses of the cation distribution revealed the occurrence of Zn_{Cu} and Zn_{Sn} point defects in B-type CZTS and Cu_{Zn} and Sn_{Zn} point defects in C-type CZTS samples, respectively. Additionally, $30-35$ % Cu_{Zn}-Zn_{Cu} anti-site defect pairs on Wyckoff positons $2c$ and $2d$ are present. These results show the limits of phase-pure off-stoichiometric CZTS materials when prepared by a mechanochemical synthesis route and should also be of relevance for the detailed understanding of the correlations between defect structure and physical properties.

Acknowledgement

References

[1] S. Chen, X.G. Gong, A. Walsh, S.-H. Wei, *Appl. Phys. Lett.* **2009**, *94*, 041903/1 – 041903/3.

[2] J.J. Scragg, P.J. Dale, L.M. Peter, G. Zoppi, I. Forbes, *Phys. Status Solidi B* **2008**, *245*, 1772 – 1778.

[3] S. Siebentritt, S. Schorr, *Prog. Photovoltaics* **2012**, *20*, 512 – 519.

[4] S. Schorr, *Sol. Energy Mater. Sol. Cells* **2011**, *95*, 1482 – 1488.

[5] L. Choubrac, M. Paris, A. Lafond, C. Guillot-Deudon, X. Rocquefelte, S. Jobic, *Phys. Chem. Chem. Phys.* **2013**, *15*, 10722 – 10725.

[6] S. Schorr, M. Tovar, B*ENSC Experimental Report* **2006**, 101.

[7] A. Ritscher, M. Hoelzel, M. Lerch, *J. Solid State Chem.* **2016**, 238, 68 – 73.

[8] S. Schorr, H.-J. Hoebler, M. Tovar, *Eur. J. Mineral.* **2007**, *19*, 65 – 73.

[9] S. Chen, A. Walsh, X.G. Gong, S.-H. Wei, *Adv. Mater.* **2013**, *25*, 1522 – 1539.

[10] S. Chen, J.-H. Yang, X.G. Gong, A. Walsh, S.-H. Wei, *Phys. Rev. B Condens. Matter Mater. Phys.* **2010**, *81*, 245204/1 – 245204/10.

[11] B. Shin, O. Gunawan, Y. Zhu, N.A. Bojarczuk, S.J. Chey, S. Guha, *Prog. Photovoltaics* **2013**, *21*, 72 – 76.

[12] W. Wang, M.T. Winkler, O. Gunawan, T. Gokmen, T.K. Todorov, Y. Zhu, D.B. Mitzi, *Adv. Energy Mater.* **2014**, *4*, 1301465/1 – 1301465/5.

[13] A. Lafond, L. Choubrac, C. Guillot-Deudon, P. Deniard, S. Jobic, Z. Anorg. Allg. Chem. **2012**, *638*, 2571 – 2577.

[14] Choubrac, A. Lafond, C. Guillot-Deudon, Y. Moelo, S. Jobic, Inorg. Chem. **2012**, *51*, 3346 – 3348.

[15] L.E. Valle Rios, K. Neldner, G. Gurieva, S. Schorr, *J. Alloys Compd.* **2016**, *657*, 408 – 413.

[16] G. Gurieva, M. Dimitrievska, S. Zander, A. Perez-Rodriguez, V. Izquierdo-Roca, S. Schorr, *Phys. Status Solidi C* **2015,** 1 – 4.

[17] A. Ritscher, J. Just, O. Dolotko, S. Schorr, M. Lerch, *J. Alloys Compd.* **2016**, *670*, 289 – 296.

[18] D.M. Toebbens, N. Stusser, K. Knorr, H.M. Mayer, G. Lampert, *Mater. Sci. Forum* **2001**, *378*, 288 – 293.

[19] H.M. Rietveld, *J. Appl. Crystallogr.* **1969**, *2*, 65 – 71.

[20] J. Rodriguez-Carvajal, *Abstracts of the Satellite Meeting on Powder Diffraction of the XV.Congress of the IUCr* **1990**, 127.

[21] I.D. Olekseyuk, I.V. Dudchak, L.V. Piskach, *J. Alloys Compd.* **2004**, *368*, 135 – 143.

[22] S. Schorr, C. Stephan, T. Toerndahl, R. Mainz in, Wiley-VCH Verlag GmbH & Co. KGaA, **2011**, 347 – 363.

[23] M. Paris, L. Choubrac, A. Lafond, C. Guillot-Deudon, S. Jobic, Inorg. Chem. **2014**, *53*, 8646 – 8653.

[24] K. Rudisch, Y. Ren, C. Platzer-Bjoerkman, J. Scragg, Appl. Phys. Lett. **201**6, *108*, 231902/1 – 231902/4.

8. Conclusion and Prospects

8.1. Conclusion

The main goal of this project was to disclose unexplored structural characteristics of the quaternary compound Cu_2ZnSnS_4. One focus was given to the full cation distribution analysis of stoichiometric CZTS powders and the order-disorder phenomenon in the structure (Paper 2). The second focus was set on the revelation of intrinsic-point defects and defect clusters in off-stoichiometric CZTS samples (Paper 4).

In order to investigate both aspects of the project precisely, first of all, the development of a novel route to CZTS was the key issue (Paper 1). A two-step process was introduced for the synthesis of phase-pure powder samples. The first step comprised the mechanochemical treatment of related binary sulfides in a planetary ball mill. Analysis of the as-milled powder at different milling times clearly showed a time-dependent formation of the quaternary compound, and it was possible to follow the reaction path in the ball mill (Paper 3).

The second process step was the annealing of the precursor powder in gaseous H_2S-atmosphere, in order to obtain crystalline samples. The influence of the annealing temperature on the precursor powder was studied using *in situ* high-temperature X-ray diffraction methods, revealing the isothermal phase formation and the crystallite growth at three different temperatures (Paper 3). Using microprobe and X-ray absorption spectroscopy analysis, phase purity and composition of the final powders were determined. Good reproducibility of the mechanochemical process, concerning the composition and crystallinity of the CZTS powders, could be shown.

As it was feasible to control the final composition of the CZTS powder easily by using the developed synthesis route, a number of CZTS samples with different compositions were successfully synthesized in this work. The samples were examined accurately, in order to gain a better understanding of the relationships between crystal structure, cation ordering, and intrinsic defects.

For exact determination of the crystal structure and the ordering of the cations on the four lattice sites, X-ray diffraction data of all samples were collected. As Cu and Zn are not distinguishable using X-ray radiation, only a partial cation distribution could be accomplished with this method. For full structural characterization and the unveiling of the

exact cation ordering in the structure, additional neutron diffraction data were collected. The crystal structures were then refined using the Rietveld method.

8.1.1. Stoichiometric samples, order-disorder transition

After the successful development of a fast synthesis route to phase-pure CZTS powder the full structural characterization of one stoichiometric CZTS sample was carried out. It could be demonstrated that Cu_2ZnSnS_4 crystallizes in the kesterite-type structure (space group $I\overline{4}$). Using X-ray diffraction, it could be shown that no significant Sn/(Cu/Zn) disorder is present in the sample, whereas for determination of the Cu/Zn ordering, neutron diffraction measurements were carried out. For the neutron scattering investigations two different refinement approaches were used to reveal the distribution of the atoms over the crystal lattice. Both methods provided the same results, showing that partial Cu/Zn disorder (~ 30 %) is present in the cation layers at $z = 1/4$ and $3/4$.

In a further study, the temperature-dependent order-disorder behavior of CZTS was investigated. Therefore, nine stoichiometric CZTS powder samples were synthesized according to the mechanochemical process. Then the powders where sealed in evacuated silica ampoules, annealed at different temperatures in a range of $473 - 623$ K (1 week) and quenched in water. Again, neutron diffraction measurements were performed. Using the Rietveld method it could be determined, that all powders crystallize in the kesterite-type structure, however varying in the order parameter.

When looking at the variation of the cation distribution as a function of the temperature, no significant differences were found on positions $2a$ and $2b$. Both lattice sites are occupied by the presumed atom over the whole temperature range, with Cu on position $2a$ and Sn on position $2b$. It can be assumed that those two cation positions are not involved in the order-disorder process. The order-disorder transformation is limited to the Wyckoff positions $2c$ and $2d$. For Zn and remaining Cu on these two sites, an obvious variation of the cation ordering was detected and a change from ordered to the disordered kesterite-type structure could be demonstrated. This order-disorder transition occured at a critical temperature of 552 ± 2 K and the refined critical exponent β was determined as 0.57 ± 0.06, indicating a Landau-type second order transition.

Finally, one stoichiometric CZTS sample was further annealed at 473 K for additional two weeks (3 weeks in total). With this second heat treatment it was possible to further increase the order paramter. Structural refinements revealed the existence of the first known sample with full order (within the standard deviation) according to the kesterite-type structure model . It can be concluded that very long annealing times are required to reach complete order of the three cation species on the four lattice sites at low temperatures.

8.1.2. Off-stoichiometric samples, intrinsic defects

With the aim to investigate the influence of the composition on the crystal structure several off-stoichiometric powder samples of the B- and C-type were successfully synthesized. It could be demonstrated that, when using the mechanochemical process, it is possible to prepare phase-pure CZTS samples far off the stoichiometric point while preserving the kesterite-type structure. When deviating from stoichiometry no real structural change is observed, expect the distribution of the three cation species on the four lattice sites. Neutron diffraction data of two samples were collected in order to perform a full cation distribution analysis. It could be concluded that B-type CZTS shows Zn_{Cu} and Zn_{Sn} intrinsic defects, whereas in the C-type material Cu_{Zn} and Sn_{Zn} point defects were found. Both results are comparable with the proposed intrinsic point defect complexes for the respective off-stoichiometric type. Additionally, Cu_{Zn}/Zn_{Cu} antisites in the lattice planes at $z = 1/4$ and $3/4$ were revealed, which is in good agreement with similar synthesized stoichiometric samples.

8.2. Outlook

The crystal structure plays a key role for the performance of a CZTS-based photovoltaic device. It can be expected that the physical properties, and thus the efficiency, are strongly dependent on the degree of order in the crystal lattice. Furthermore, the occurence of intrinsic defects seem to be an important issue. The knowledge acquired from this research work can be of strong interest for future thin film preparation processes, as it provides information about fundamental characteristics of the compound semiconductor material. In the light of the presented observations, the direct synthesis of samples with a defined and optimized order parameter, as well as the design of CZTS-based solar cells with minimized cation disorder should be possible. Additionally, the findings could be of importance not only in CZTS material but also in structure/function studies of other multinary chalcogenide compounds, which are in focus of interest for electronic applications.

Despite the new findings, which were systematically obtained in the present study, still some structural features of the CZTS material, regarding defect clustering and defect concentration limits, should be examined in more detail. This circumstance will strengthen future efforts for the preparation and investigation of CZTS material and should lead to a steady development of synthesis methods and solar cell properties.

The newly developed synthesis route provides a suitable basis for prospective attempts to prepare CZTS compounds. In order to investigate intrinsic defects and defect complexes in more detail, off-stoichiometric powders of the remaining off-stoichiometric types could be produced. Besides, the method could also be used to synthesize other quaternary sulfide compounds, which are difficult to prepare using a conventional solid-state route.

A. Appendices

A.1. Additional information, Supplementary material

A.1.1. Abbreviations

BSE   Back scattered electrons
CIGS   Cu(In,Ga)Se$_2$
CTS   Cu$_2$SnS$_3$
CZTS   Cu$_2$ZnSnS$_4$
CZTSe   Cu$_2$ZnSnSe$_4$
CZTSSe   Cu$_2$ZnSn(S,Se)$_4$
EDS   Energy dispersive spectroscopy
EMPA   Electron microprobe analysis
FWHM   Full width of half maximum
PV   Photovoltaic
RPM   Rounds per minute
WDS   Wavelength dispersive spectroscopy
XAS   X-ray absorption spectroscopy
XANES   X-ray absorption near edge spectroscopy
XRD   X-ray diffraction

A.1.2. Chemicals

Table A.1.: List of utilized chemicals

Name	Purity	Producer
H$_2$S	99.5 %	Air Liquide
Cu(NO$_3$)$_2$	99.5 %	Merck
ZnO	99.5 %	Merck
Sn	99.9 %	Merck
S	99.99 %	Fluka

A.1.3. XRD pattern of binary starting materials
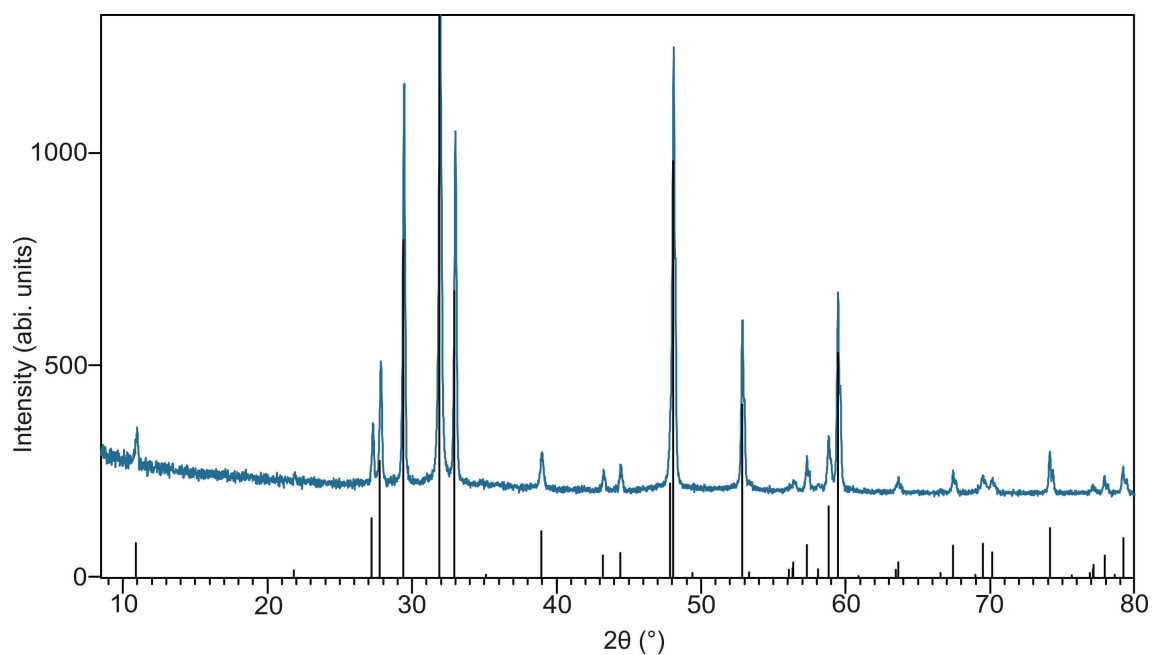
Figure A.1.: Diffraction pattern of synthesized CuS, covellite (space group $P6_3/mmc$)
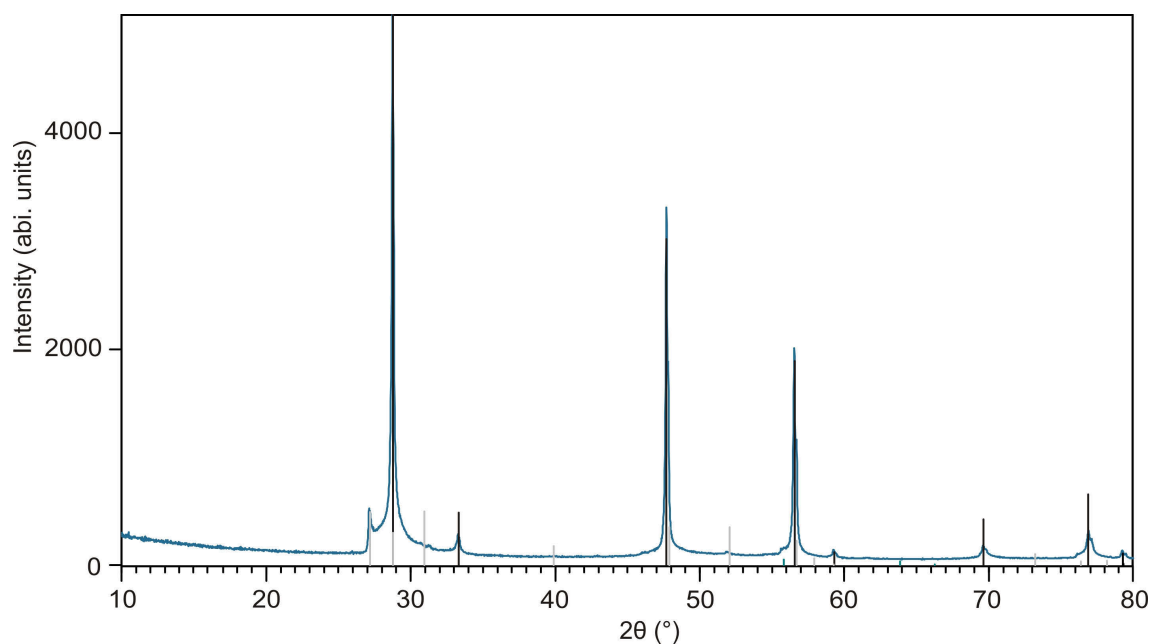
Figure A.2.: Diffraction pattern of synthesized ZnS, sphalerite (dark grey, space group $F\overline{4}3m$) with additional wurtzite (light grey, space group $P6_3mc$)
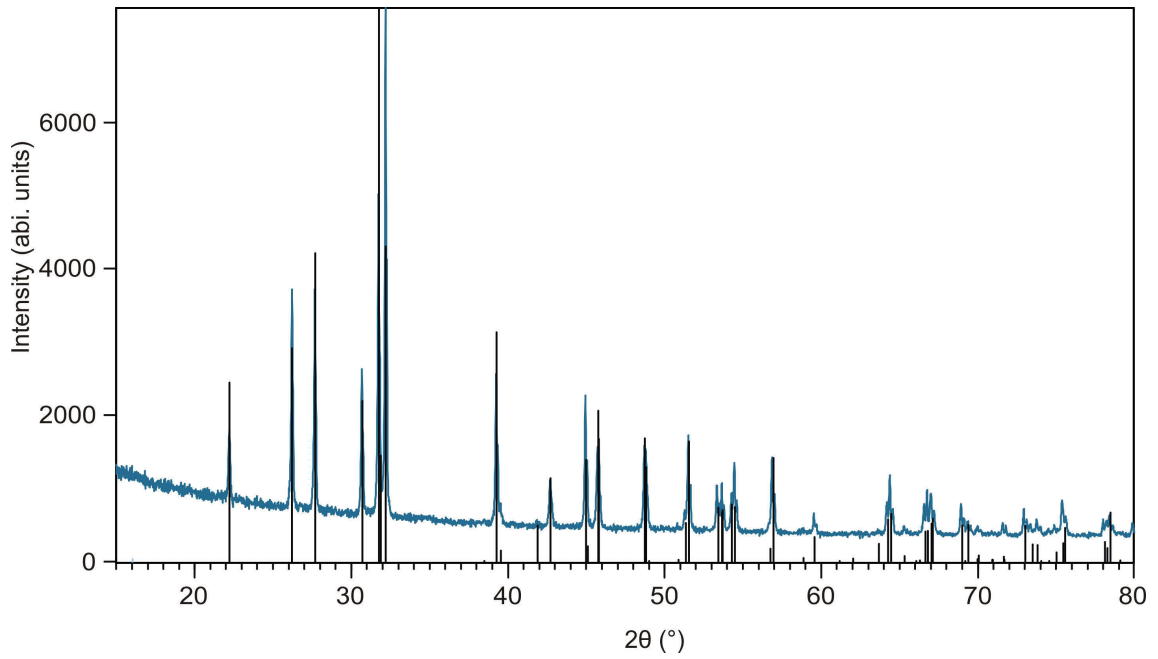
Figure A.3.: Diffraction pattern of synthesized SnS, herzenbergite (space group *Pnma*)

A.1.4. Phase diagrams of binary systems
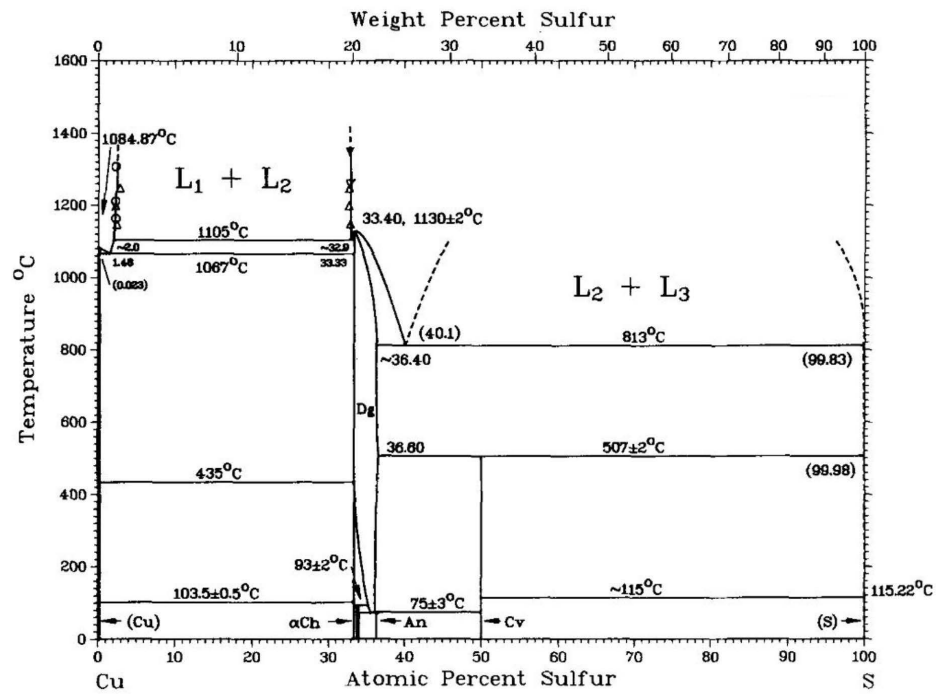
Figure A.4.: Phase diagram of the Cu-S system according to Chakrabarti and Laughlin
[63]
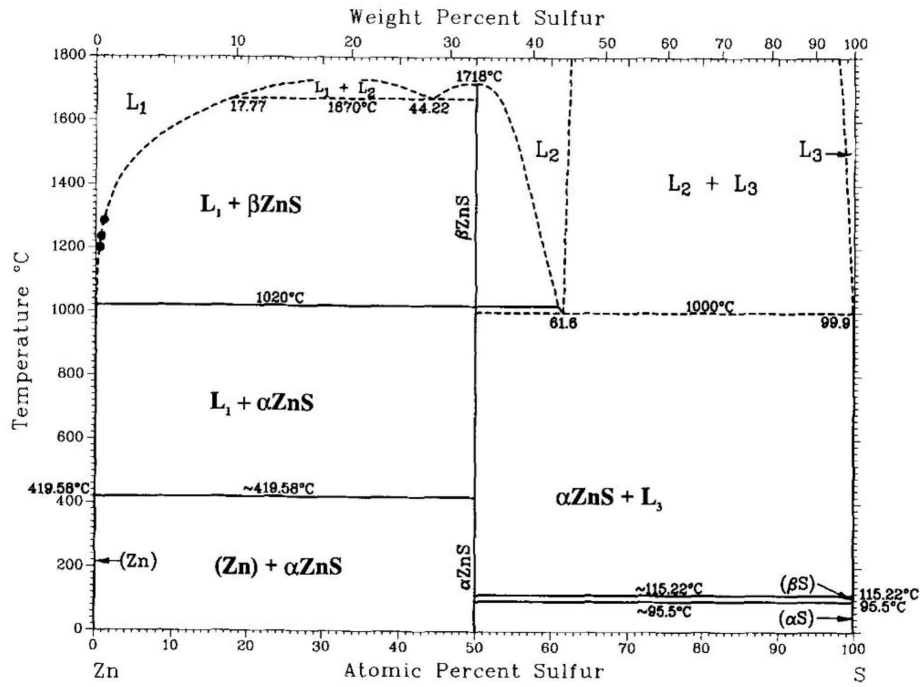
Figure A.5.: Phase diagram of the Zn-S system according to Sharma and Chang [64]
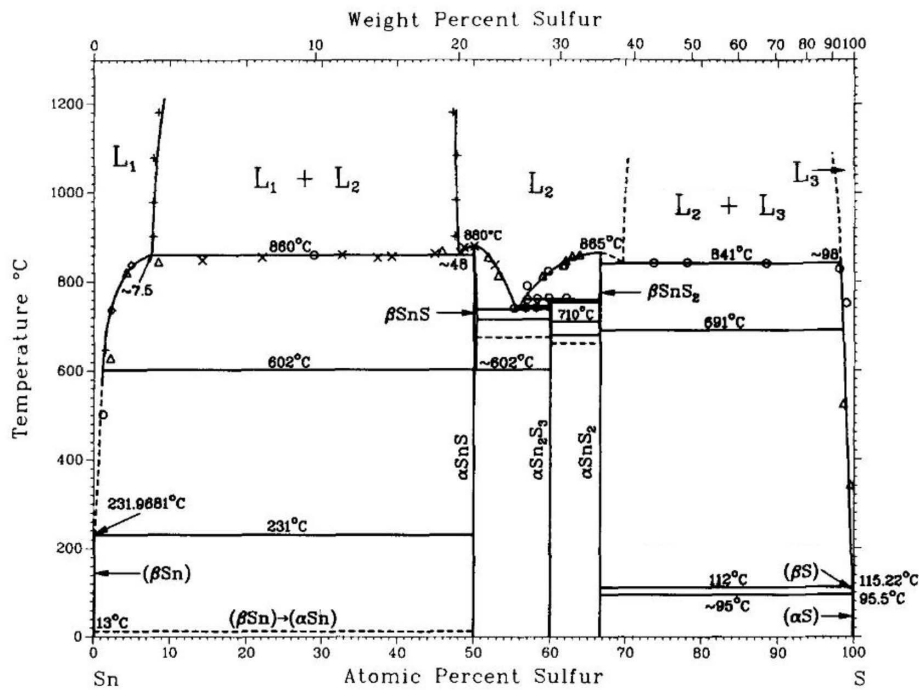
Figure A.6.: Phase diagram of the Sn-S system according to Sharma and Chang [69]

A.2. List of publications

1. A. Ritscher, M. Lerch; "Mechanochemische Synthese von kristallinem Cu_2ZnSnS_4" *Z. Anorg. Allg. Chem.* 2014, *640*, 2387. doi: 10.1002/zaac.201404102

2. A. Ritscher, M. Lerch; "Low-temperature route to crystalline Cu_2ZnSnS_4" *Z. Kristallog./ Supplemente* 2014, *34*, 143. doi: 10.1524/9783110376388.110

3. A. Ritscher, O. Dolotko, M. Lerch; "Neutron scattering of mechanochemical prepared CZTS" *Z. Kristallog./Supplemente* 2015, *35*, 78. doi: 10.1515/9783110415377-023

4. A. Ritscher, J. Just, O. Dolotko, S. Schorr, M. Lerch; "A mechanochemical route to single phase Cu_2ZnSnS_4 powder" *J. Alloys Compd.* 2016, *670*, 289 – 296. doi: 10.1016/j.jallcom.2016.02.058

5. A. Ritscher, M. Hoelzel, M. Lerch; "The order-disorder transition in Cu_2ZnSnS_4" *Z. Kristallog./Supplemente* 2016, *36*, 67 doi: 10.1515/9783110476620-023.

6. A. Ritscher, M. Hoelzel, M. Lerch; "The order-disorder transition in Cu_2ZnSnS_4 – a neutron scattering investigation", *J. Solid State Chem.* 2016, *238*, 68 – 73. doi: 10.1016/j.jssc.2016.03.013

7. A. Ritscher, M. Schlosser, A. Pfitzner, M. Lerch; "Study of the mechano-chemical process to crystalline Cu_2ZnSnS_4 powder", *Mater. Res. Bull.* 2016, *84*, 162 - 167. doi: 10.1016/j.materresbull.2016.08.006

8. A. Ritscher, A. Franz, S. Schorr, M. Lerch; "Off-stoichiometric CZTS – Neutron scattering investigations on mechanochemical synthesized powders", *J. Alloys Compd.* 2016, *689*, 271 - 277. doi: 10.1016/j.jallcom.2016.07.298

9. A. Ritscher, M. Schlosser, A. Pfitzner, M. Lerch; "Detaillierte Untersuchung des mechanochemischen Prozesses zur Synthese von CZTS (Kesterit)" *Z. Anorg. Allg. Chem.* 2016, accepted.

A.3. List of conference contributions

09/2016   19. Vortragstagung Fachgruppe Festkörperchemie und Materialforschung, Innsbruck, Austria – *Poster*

03/2016   24$^\text{th}$ Annual Meeting of the German Crystallographic Society (DGK) 2016, Stuttgart, Germany – *Poster*

08/2015   15$^\text{th}$ European Conference on Solid State Chemistry (ECSSC15) 2015, Vienna, Austria – *Poster*

05/2015   E-MRS Spring Meeting 2015, Lille, France – *Poster*

03/2015   23$^\text{th}$ Annual Meeting of the German Crystallographic Society (DGK) 2015, Göttingen, Germany – *Poster*

11/2014   5$^\text{th}$ European Kesterite Workshop 2013, Tallin, Estonia – *Poster*

09/2014   18. Vortragstagung Fachgruppe Festkörperchemie und Materialforschung, Dresden, Gemany – *Poster*

03/2014   22$^\text{th}$ Annual Meeting of the German Crystallographic Society (DGK) 2014, Berlin, Germany – *Poster*

11/2013   4$^\text{th}$ European Kesterite Workshop 2013, Berlin, Germany – *Poster*

List of Figures

List of Tables

Eidesstattliche Versicherung

Hiermit versichere ich an Eides statt, die vorliegende Dissertation mit dem Titel "Synthesis and Structural Characterization of Semiconductors based on Kesterites" selbstständig und eigenhändig und nur unter Verwendung der in meiner Dissertation angegebenen Hilfsmittel und Literatur verfasst zu haben. Die Angaben über den Eigenanteil meiner Veröffentlichungen in meiner Erklärung sind zutreffend.

Untertschrift,Datum

....